Crystal-phase defined nanowire quantum dots as a platform for qubits

Inauguraldissertation

zur
Erlangung der Würde eines Doktors der Philosophie
vorgelegt der
Philosophisch-Naturwissenschaftlichen Fakultät
der Universität Basel

von

Alessia Prisca Pally

Basel, 2024

Originaldokument gespeichert auf dem Dokumentenserver der Universität Basel
`edoc.unibas.ch`

Genehmigt von der Philosophisch-Naturwissenschaftlichen Fakultät
auf Antrag von
Erstbetreuer: Prof. Dr. Christian Schönenberger
Zweitbetreuer: Prof. Dr. Dominik Zumbühl
Externe Experten: Prof. Dr. Georgios Katsaros, Dr. Heike Riel

Basel, den 13.12.2022

Prof. Dr. Marcel Mayor
Dekan

Contents

1. Introduction **1**

2. Theoretical background **5**

2.1. Quantum dots . . . 5

2.1.1. Coulomb blockade and single electron tunneling . . . 6

2.1.2. Resonance line shapes . . . 9

2.1.3. Coulomb blockade diamonds . . . 10

2.1.4. Quantum dot states in a magnetic field . . . 12

2.1.5. Double quantum dots . . . 12

2.1.6. Two-level systems . . . 17

2.2. Cavity quantum electrodynamics with quantum dots . . . 22

2.2.1. Coupling a resonator to a charge qubit . . . 22

2.2.2. Input-Output theory . . . 24

2.2.3. Coupling a resonator to a spin qubit . . . 25

2.3. Superconductivity . . . 26

2.3.1. Cooper pairs and superconducting gap . . . 26

2.3.2. Transport in superconductor - normal metal structures . 29

2.3.3. Crossed Andreev reflection and Andreev bound states . 31

2.3.4. Superconducting Islands . . . 33

3. Experimental Methods **37**

3.1. Fabrication . . . 37

3.2. Low-frequency measurement setup . . . 43

3.3. Radio-frequency measurement setup . . . 45

4. Material Platform **49**

4.1. Nanowire Growth . . . 49

4.2. Electronic Properties . . . 52

4.3. Characterization of InAs nanowires . . . 53

4.3.1. Single tunnel barrier . . . 54

4.3.2. Single quantum dot . . . 56

4.3.3. Double quantum dot . . . 58

4.4. Summary and Outlook . . . 60

5. Spectroscopy of the superconducting proximity region **63**

5.1. Three-terminal measurements . . . 64

5.1.1. The conductance of adjacent contacts . . . 64

        5.1.2. The conductance across the whole device 69
    5.2. Superconducting proximity gap 73
    5.3. Summary and Outlook 76

6. Charge sensing of a superconducting charge box **79**
    6.1. Cooper pair island device 79
    6.2. QD as charge sensor for the superconducting charge boxes . . . 81
        6.2.1. Magnetic field dependence 82
        6.2.2. Time-resolved tunnel events 86
    6.3. Proximitized nanowire quantum dot 91
    6.4. Summary and outlook 95

7. Dispersive sensing of a double qunatum dot **99**
    7.1. The resonator-nanowire hybrid device 99
    7.2. Dispersive read-out 101
    7.3. Charge qubit 103
    7.4. The strongly dispersive regime and the Bloch-Siegert shift . . . 106
    7.5. Crossing of the charge qubit 107
    7.6. Summary and Outlook 107

8. Strong coupling between a microwave photon and a singlet-triplet qubit **109**
    8.1. Introduction 110
    8.2. Device characterization 112
    8.3. Strong spin-photon coupling 115
    8.4. Magnetospectroscopy 117
    8.5. Conclusion and Outlook 120

9. Summary and Outlook **123**

Bibliography **127**

A. Fabrication Recipes **143**
    A.1. Fabrication of InAs NW Devices 143
        A.1.1. Wafer Characteristics 143
        A.1.2. Wafer Cleaning 143
    A.2. E-beam Lithography, Development and Lift-off 143
    A.3. Reactive ion etching - O_2 Plasma Etching 144
    A.4. Etching of the GaSb-shell before metallization 144
    A.5. Contacts 144
        A.5.1. Ti/Au contacts 144
        A.5.2. Ti/Al contacts 145
        A.5.3. Thin Al contacts 145

B. Additional data on the material platform 147
B.1. Gate dependence with and without built-in tunnel barrier . . . 147
B.2. Addition energy of a single quantum dot 147

C. Additional data on Cooper pair charge sensing of a superconducting charge box 149
C.1. Full dataset on magnetic field maps 149
C.2. Wrongly detected tunnel events 149

D. Additional data strong coupling between a microwave photon and a singlet-triplet qubit 155
D.1. Resonator characterization and analysis 155
D.2. InAs crystal-phase nanowires 156
D.3. Hamiltonian in the odd charge parity 157
D.4. Extraction of parameters using input-output theory 157
D.5. Charge parity determination 158
D.6. Analysis of device B 161
  D.6.1. Charge-stability diagram 162
  D.6.2. Avoided crossing 163
D.7. Magnetospectroscopy 165

Curriculum Vitae 169

Publications 171

Acknowledgments 173

1 Introduction

In the last decades hardly any achievement has shaped humanity as much as the invention of the first transistor more than 70 years ago by Bardeen, Brattain, and Shockley. Since then technology has improved by leaps and bounds: today's average smartphone has more computational power than a supercomputor of the late nineties, barely more than 20 years ago. This has been best described in the famous "Moore's law", [1, 2], that states that the number of transistors in an integrated circuit doubles about all two years. This exponential increase, achieved by shrinking the transistor size, has governed every progress in computer based technologies for decades.

However in recent years Moore's law has started to breakdown [3]. The increased heat load of the increasingly small and dense circuitry is starting to slow down progress in microprocessor design. Furthermore, even if this issues can be solved, classical computation has an intrinsic lower bound in size. As transistor size shrinks, quantum effects are becoming increasingly important. Eventually, their random nature will destroy classical computation. In order to truly advance technology and satisfy the ever increasing consumer demands, quantum effects need not be seen as a problem but an advantage to make use of. Doing so entails the evolution of a classical bit to a quantum bit (qubit), where information is encoded in the superposition of a quantum states [4].

Quantum computation is in early stages and the most promising platform has not been determined yet. So far, superconducting qubits [5–7] and trapped ions [8, 9] have been at the forefront in numbers of qubits and computational power. However, despite immense progress in error correction [10], quantum computation is still on the noisy intermediate-scale quantum technology level [11]. Hence, a major focus of the physics community lies with the exploration of further platforms for quantum computing. This search focuses on two major points: less error prone qubits and more scalable architectures.

To mitigate error [12] an interesting approach is given by exploiting topological protection [13] of topological particles, such as Majorana bound states (MBS) [14–17] or parafermions [18–20]. They can be engineered [13, 16, 21] by the combination of a strong spin-orbit material proximitized by a superconductor and an external magnetic field. At the same time recent advances in the growth of semiconducting nanowires and metallic-interface engineering has opened up a realm of new nanowire based semiconducting devices. Examples include nanowire crosses [22–24] and networks [25–28], in-situ grown epitaxial metal-nanowire interfaces [29–33], and nanowire heterostructures in radial [34, 35] and axial [36–40] direction. Furthermore, advances in template-assisted nanowire growth [27, 41, 42] and selective-area growth [23, 25, 26, 28] have come closer to a scalable growth approach to nanowire structures.

The advances of epitaxial superconducting interfaces to nanowires have lead to numerous experimental reports of signatures of MBS [43–47]. However their unambiguous identification has been challenging, as they can be mimicked by other non-topological phenomena [48, 49], most prominently Andreev bound states (ABS) [50–54]. Quantum dots (QDs) are a useful spectroscopy tool to probe MBS or ABS. They are predicted to allow the study of the MBS lifetime [55], parity [56], and spin texture [57]. In spectroscopy experiments, QDs are often defined by electrostatic gating [43–45, 58] or the source-drain contacts [59], which can make control and understanding of these QDs difficult.

Combining the spectroscopy of possible MBS with the nanowire heterostructures could make the identification of MBS more reliable. Radial heterostructures grown by crystal-phase control in InAs nanowire have shown to host well-defined tunnel barriers and QDs [39, 60–62]. The number, length and distance between crystal-phase defined barriers can be tuned during growth [40] and thus allows for an individually tailored system to study potential MBS.

Furthermore, the same crystal-phase defined tunnel barriers can be used to create double QDs (DQDs) in InAs nanowires. Nanowires with built-in DQDs can be readily combined with the knowledge of circuit quantum electrodynamics gained from superconducting qubits [63–65]. Coupling a superconducting resonator to a qubit enables rapid, high-fidelity qubit-readout [66] and long-range coupling between qubits [67]. The combination of these two systems has lead to strong charge-photon [68, 69] and strong spin-photon coupling [70–72], as well as coherent coupling of distant qubits [73–75]. Many of these structures are reliant on complicated device architecture, such as micromagnets [74], to couple the resonator to the spin-degree of freedom. However, the same effect can be achieved using the strong intrinsic spin-orbit interaction in InAs nanowires [76] and the device architecture is further simplified by needing no additional gates to define the DQD.

Aim of the thesis

This thesis aims to study InAs nanowires with built-in crystal-phase defined QDs as a platform for quantum computing. We investigate them as a platform for topological qubits, as well as charge and spin qubits. In a first step towards MBS we investigate the induced superconductivity in nanowire hybrid device where the superconductor is deposited by standard e-beam evaporation without an epitaxial interface to the nanowire. Using the integrated tunnel barriers as spectrometer, we draw conclusions about the origin of quasiparticle poisoning in our system.

In a second approach we couple a nanowire DQD to a high-impedance resonator. In the first step we will investigate the resonator-nanowire hybrid device as a charge qubit. We observe a very large qubit linewidth. To improve our system we turn to spin qubits. We take advantage of the strong spin-orbit coupling in our nanowires to couple the resonator to a singlet-triplet qubit, with which we demonstrate strong spin-photon coupling.

Outline of the thesis

In **chapter** 2 we will introduce the most important theoretical concepts relevant for this work. We start with a brief introduction to single QDs, followed by DQD and the charge and spin qubits in them. We will turn to a short introduction to resonators and circuit quantum electrodynamics. To finish we will give a concise introduction to the basic superconductivity phenomena discussed here.

Chapter 3 will introduce the most important experimental methods, including a summary of the standard fabrication process of our devices as well as a brief summary of the measurement setups. In **chapter** 4 we will give a brief explanation of the growth and electronic properties of the InAs nanowires used in this work. We will follow up with some basic characterization measurements of our integrated tunnel barriers and QDs.

In **chapter** 5 we study the superconducting properties of superconductor-nanowire hybrid devices. We will use three-terminal measurements to show that we perform tunneling spectroscopy on an induced proximity region and not the superconducting contact. Furthermore, we will investigate our "soft" gap and give some explanations to its origin.

Following this we study a Cooper pair island in **chapter** 6. We accidentally create superconducting charge boxes (SCB) in aluminium side gates. We use the integrated nanowire QD as a charge sensor for these SCB and observe the 2e-parity of a Cooper pair island. Furthermore, we measure time-resolved Cooper pair tunneling.

Chapter 7 turns to the resonator-nanowire hybrid device. We couple a NbTiN high-impedance resonator to a nanowire DQD. We perform dispersive sensing on the DQD and characterize the dispersive shift of the resonator in response to the two-level system of the DQD. We extract the DQD tunnel rates, qubit linewidth, and the charge-photon coupling strength for different inter-dot resonances.

In **chapter** 8 we add a magnetic field to the resonator-nanowire hybrid system and show the creation of a singlet-triplet qubit. We model the general behavior of the qubit with a simplified two-electron Hamiltonian and extract tunnel rates, spin-photon coupling strength and linewidth of the qubit. With this we demonstrate strong spin-photon coupling.

Finally, we conclude with **chapter** 9 summarizing the most important finding and giving an outlook on further steps and experiments in the future.

2 Theoretical background

This chapter will serve to introduce the most important theoretical concepts that are the foundation of this work. The first part will be an introduction to electron transport in single and double quantum dots. Further, the usage of double quantum dots to create charge and spin qubits will be discussed. We will follow up with a brief introduction to the coupling of spin and charge qubits to superconducting resonators. The second part will give a brief introduction to superconductivity and electron transport at a normal-superconductor interface, as well as superconducting islands. The theory of the quantum dots and superconductivity parts will partially follow Refs. [77–80], while the qubit part will follow Refs. [77, 81–83]

2.1. Quantum dots

Tunnel barriers and quantum dots (QDs) are the building blocks of which all experiments in this thesis are build upon. Either as a spectroscopy tool (chapters 4, 5, and 6) or as a platform for qubits (chapters 7 and 8). In a quantum dot the motion of electrons is confined in all three spatial dimensions resulting in a quantized energy spectrum. Due to this spectrum, they are sometimes referred to as "artificial atoms" [84]. However unlike actual atoms, QDs can be coupled to source-drain electrodes and their electrostatic potential tuned by gate electrodes. This allows us to study both their electronic properties at low temperatures. Quantum dots have been realized in various solid state systems. Examples include semiconducting nanowires [35, 39, 44, 85], carbon nanotubes [86–88], graphene nanoribbons [89], two-dimensional electron gases (2DEGs) [90–92], and van-der-Waals materials [93].

A QD is typically a very small structure on the order of a few hundreds nanometer, as the name "dot" implies. QDs have a characteristic energy scale, the so called charging energy E_C. This energy is analogues to the ionization energy of an atom and describes the energy necessary to add or remove a single electron to the QD. The charging energy has to exceed the thermal energy $k_B T$ of the electrons to be a relevant energy scale [77, 94]. An electronic one-dimensional channel, such as a semiconducting nanowire (NW), confines an electron in two dimensions. To create a QD an additional confinement in the lateral direction is necessary. This can be achieved by either Shottky-contacts

[95] or in a more controlled way by gate-defined barriers [68, 93, 96–99] or in-built tunnel barriers [35, 60, 85]. This barrier has to be sufficiently opaque, so that fluctuations of the occupation number N on the QD are much less than one over the timescale of the measurement. This gives us a lower bound for the tunnel resistance R_t, as the energy uncertainty should be much lower than the charging energy. Therefore, R_t should be much larger than the resistance quantum, $R_t \gg h/e^2 = 25.813\ \mathrm{k}\Omega$ [77, 94].

2.1.1. Coulomb blockade and single electron tunneling

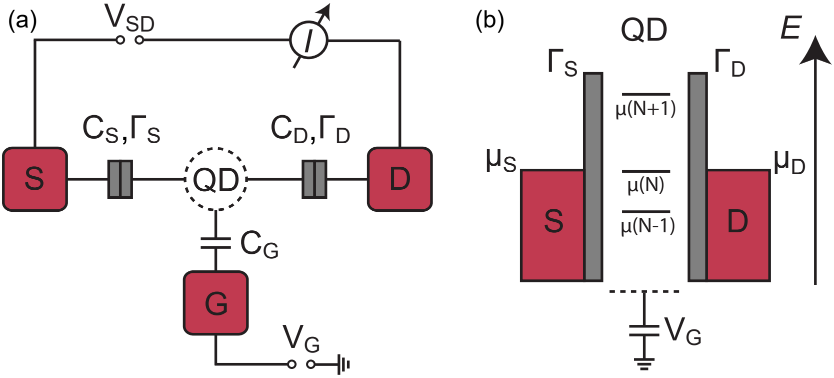

Figure 2.1. Quantum dot model. (a) Capacitance model and typical circuit measurement diagram. A quantum dot (QD) is tunnel coupled to a source-drain leads with capacitances $C_{S/D}$ and tunnel coupling $\Gamma_{S/D}$. A purely capacitive coupling C_G to the gate G allows to tune the electrochemical potential of the QD. (b) Schematic of the energy level diagram of a QD with N electrons and electrochemical potential μ_N. Adapted from [60, 78, 100, 101].

Given the criteria mentioned above, that the temperature is sufficiently large and the tunnel barriers sufficiently opaque, Coulomb interactions between electrons on the QD become a relevant or even dominating energy scale [94]. Coulomb interactions can be well described within the framework of the *constant interaction model* (CIM) [84, 94]. This models makes two assumptions. First, the Coulomb interactions of the QD can be described by a constant capacitance C. Second, the energy spectrum of the QD is unaffected by both electron-electron interaction and the occupation number N of the QD.

Let us assume a QD as illustrated in Fig. 2.1. A QD is tunnel coupled to a source (drain) lead with tunnel coupling Γ_S (Γ_D) and a capacitive coupling C_S (C_D). A finite current can be induced from source to drain contact by applying a finite bias voltage $V_{SD} = V_S - V_D$. Furthermore, the QD is purely capacitively coupled to a gate electrode G, where a gate voltage V_G can be applied to tune the electrostatic potential on the QD. The sum of these gives us the QD capacitance $C = C_S + C_D + C_G$. For N electrons the total energy E_{tot} on the QD is given by [91, 102].

$$E_{tot}(N) = \frac{Q_{tot}^2}{2C} + \sum_{j=1}^{N} E_j = \frac{1}{2C}[e(N - N_0) - \sum_i C_i V_i]^2 + \sum_{j=1}^{N} E_j, \tag{2.1}$$

where N_0 is the QD occupancy for all $V_i = 0$ and Q_{tot} describes the total charge on the QD [94, 102]. The first term accounts for the electrostatic energy on the QD. Hereby, $\sum_i C_i V_i$ describes the gate-induced charges. The second term accounts for the sum of occupied quantum states of the QD. As we usually measure energy difference in transport, it is convenient to use the electrochemical potential μ of the QD.

$$\mu(N) = E_{tot}(N) - E_{tot}(N-1) = E_N + \frac{e^2}{C}(N - N_0 - \frac{1}{2}) - \frac{|e|}{C}(\sum_i C_i V_i) \tag{2.2}$$

This expression describes the energy needed to add the N$^{\text{th}}$ electron to the QD assuming the QD is already populated by N-1 electrons. Figure 2.1(b) illustrates this "ladder" of energy levels of the QD [91, 102]. The energy difference between this levels is called the *addition energy*

$$E_{add} = \mu(N+1) - \mu(N) = \frac{e^2}{C} + \delta E \tag{2.3}$$

where $E_C = \frac{e^2}{C}$ is the charging energy and $\delta E = E_{N+1} - E_N$ is the quantum mechanical level spacing of the QD [91, 102]. The ladder of electrochemical potentials can be shifted linearly by applying a gate voltage V_G. The gate can shift the ladder by $\alpha_G e \Delta V_G$, where $\alpha_G = C_G/C$ is called the gate lever arm or efficiency factor.

Let us now assume a linear response $V_{SD} \approx 0$ and small thermal broadening $k_B T \ll \delta E \ll E_C$. In this case we can assume that the Fermi distribution in the leads $f_{S/D} = \frac{1}{\exp((E - \mu_{SD})/k_B T) + 1}$ can be approximated by a step function with a small thermal broadening $k_B T$. As is illustrated in Fig. 2.2(a) electron transport through the QD is only possible if the potential of the source-drain leads aligns with the electrochemical potential of the QD, $\mu_{S/D} = \mu(N)$. If this condition is fulfilled the QD is on resonance and a single electron can tunnel from one lead into the QD and into the second lead. This process where sequentially tunneling discrete charges is called *single electron resonant tunneling*. In a transport measurement this will lead to a peak in the differential conductance

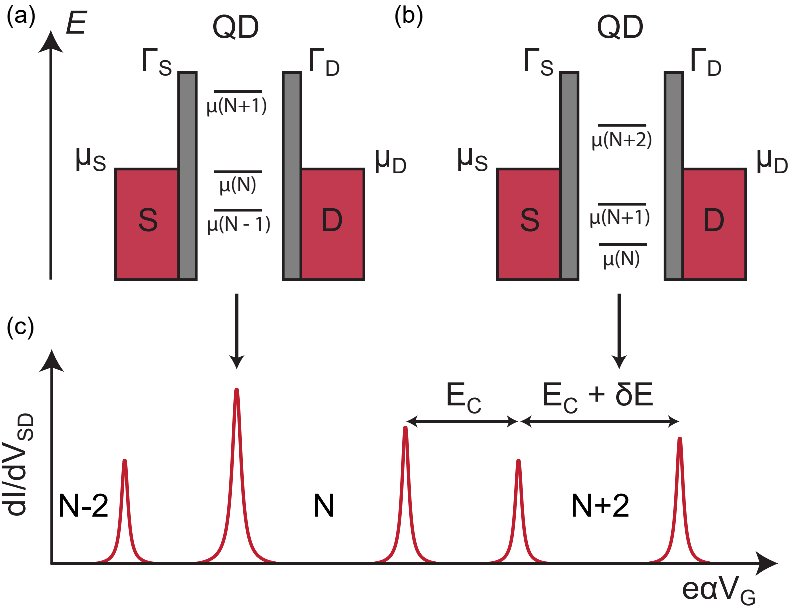
(a)
E
QD
Γ_S
Γ_D
μ(N+1)
μ_S
μ(N)
μ(N - 1)
μ_D
S
D
(b)
QD
Γ_S
Γ_D
μ(N+2)
μ_S
μ_D
μ(N+1)
μ(N)
S
D
(c)
dI/dV_SD
E_C
E_C + δE
N-2
N
N+2
eαV_G

Figure 2.2. Coulomb blockade and single electron tunneling. Alignment of the electrochemical potential $\mu(N)$ with the potential of the source-drain contacts $\mu_{S/D}$ for (a) single electron resonant tunneling and (b) Coulomb blockade. (c) schematic of a typical transport measurement of the differential conductance dI/dV_{SD} in dependence of the gate voltage V_G. Adapted from [60, 78, 100, 101].

dI/dV_{SD} at the resonance position of the QD. By varying the gate voltage different electrochemical potential can be tuned on resonance. However, if the electrochemical potential of the QD is not aligned with the potential in the leads, i.e $\mu(N) < \mu_S = \mu_D < \mu(N+1)$, electron transport is blocked, as the neither the electrons in the leads have enough energy to tunnel into the QD nor do the electrons in the lower energy QD levels have enough energy to tunnel out of the QD. This state is referred to as Coulomb blockade (CB). Assuming simple two-fold spin degeneracy (as is usual for InAs nanowires), we see a spacing between the Coulomb peaks as illustrated in Fig. 2.2(c). Adding an electron to a new orbital requires the addition energy $E_{add} = E_C + \delta E$, while adding a second electron to an already single occupied orbital cost $E_{add} = E_C$ [91, 94].

2.1.2. Resonance line shapes

In the above description we did not account for finite temperature broadening nor tunnel coupled broadening $\Gamma_{S/D}$ of the lineshape of the Coulomb resonances. While the $\Gamma_{S/D}$ have to be sufficiently small to create a QD, even a small coupling $\Gamma = \Gamma_S + \Gamma_D$ will lead to a finite lifetime τ of the electrons on the QD. According to Heisenberg's uncertainty principle this small lifetime creates an energy window $\sim h/\tau$. Due to this energy window electrons are able to tunnel through the barriers even at slightly off resonance energies, which broadens the Coulomb resonance. We will differentiate between two limiting cases of broadening. For $k_BT \ll \Gamma \ll \delta E, E_C$ we speak of the *life-time broadened* or *strong coupling* regime, where the broadening is given by the tunnel coupling to the leads and can be well described in conductance $G = dI/dV_{SD}$ by a Lorentzian lineshape [77]

$$G(\Delta E) = \frac{e^2}{h}\frac{4\Gamma_S\Gamma_D}{\Gamma^2}\frac{(\Gamma/2)^2}{\Delta E^2 + (\Gamma/2)^2}, \tag{2.4}$$

where $\Delta E = -e\alpha_G(V_G - V_G^{(0)})$ is the energy detuning with respect to the resonance at $V_G^{(0)}$. The tunnel coupling Γ is given by the full width at half maximum (FWHM) of the resonance and the conduction is maximal for symmetric barriers. In the *thermally broadened limit* or *weak coupling regime*, where $\Gamma \ll k_BT \ll E_C, \delta E$, the Coulomb peak lineshape is given by [103].

$$G(\Delta E) = \frac{e^2}{h}\frac{\pi}{2k_BT}\frac{\Gamma_S\Gamma_D}{\Gamma}\cosh^{-2}\left(\frac{\Delta E}{2k_BT}\right). \tag{2.5}$$

The maximum of the conductance is reached for symmetric barriers and scales with $\sim 1/k_BT$

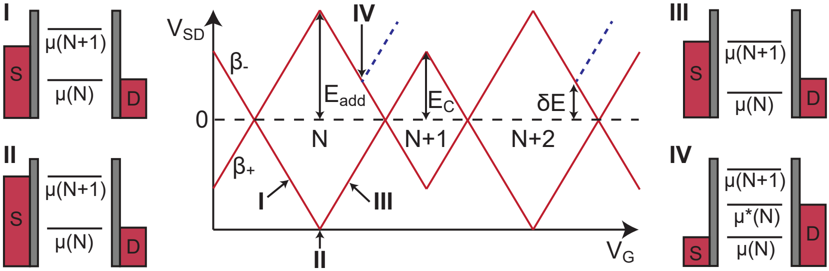

Figure 2.3. Schematic of Coulomb diamonds An illustration of a typical differential conductance G measurement of a QD as a function of gate voltage V_G and source-drain bias V_{SD}. The QD has a two-fold degeneracy. The lines with slopes β_+ and β_- show the onset of transport, where the source-drain potential align with the QD level μ_N, as shown in the schematics **I-III**. **IV** marks the onset of the first excited state. Adapted from [60, 78, 100, 101].

2.1.3. Coulomb blockade diamonds

So far we have only considered QDs without any source-drain bias. Just as Coulomb blockade can be overcome by applying a gate voltage V_G, it can also be overcome by applying a source-drain bias V_{SD}. Coulomb blockade can be lifted if an electrochemical potential level μ_{QD} enters the bias window $-|e|V_{SD} = \mu_S - \mu_D$. In a measurement this will be signified by a step in current or a peak in conductance. Measuring conductance G in dependence of V_G and V_{SD} results in the so-called Coulomb diamonds as illustrated in Fig. 2.3. Within the diamonds there are no μ_{QD} within the bias window, therefore no electron transport can happen. No conductance will be measured and the number of charges on the QD is fixed. Outside the diamonds there is at least one QD level within the bias window and transport can happen. Hence, the electron number on the QD is constantly fluctuating. The boundary of the diamonds are given by the condition $\mu_{QD} = \mu_{S/D}$. In Fig. 2.3 **I** (**III**) the drain (source) potential aligns with the QD level resulting in the line with negative (positve) slope $\beta_- = \frac{\Delta V_{SD}}{\Delta V_G}$ (β_+). At the top of the diamond (**IV**) the two lines cross, thus the source-drain bias at that point is directly equal to the difference in adjacent electrochemical potentials on the QD. This allows to directly measure the addition energy $E_{add} = E_C + \delta E$. The schematic shown in Fig. 2.3 is two-fold degenerate, as such the addition energy E_{add} is given by the larger diamond and the charging energy E_C is given by the subsequent, smaller diamond. The orbital energy δE can be extracted from the difference between the two [102].

Let us assume an asymmetric bias for our QD, where the drain contact is grounded $\mu_D = 0$ and all the potential is applied on the source contact $\mu_S = -|e|V_{SD}$. As seen above we can extract the addition energy, charging energy and orbital energy from height of the Coulomb diamonds. From the slopes $\beta_{+/-}$ we can also extract the capacitances of the QD and the lever arm of the gates. From the negative slope with $0 = \mu_D = \mu_{QD}$ and Eq. 2.2 we get $0 = -|e|\frac{C_G}{C}\Delta V_G - |e|\frac{C_S}{C}\Delta V_{SD}$, i.e to keep the electrochemical potential constant the gate has to compensate the capacitive shift of the source contact. We can do the same calculation for the positive slope, giving us $|e|V_{SD} = -|e|\frac{C_G}{C}\Delta V_G - |e|\frac{C_S}{C}\Delta V_{SD}$. Using this equations and the definition of the slopes $\beta_{-/+} = \frac{\Delta V_{SD}}{\Delta V_G}$, we get $\beta_- = -\frac{C_G}{C_S}$ and $\beta_+ = -\frac{C_G}{C-C_S}$. We can also combine these to a get the lever arm of the gate $\alpha_G = \frac{C_G}{C} = \frac{\beta_+|\beta_-|}{\beta_+ + |\beta_-|}$. With the gate lever arm gate axes can be converted to energies. This is useful to extract energy scales like the addition energy from CB peaks or extract the photon-charge coupling strength from the dispersive shift of a resonator [77, 78].

Excited states and cotunneling

So far we have only discussed ground state transition $E_{tot}(N) \leftrightarrow E_{tot}(N)$, however other excited processes are possible. If a bias voltage $|eV_{SD}| > \delta E$ is applied, the Nth electron can be excited into the orbital level E_{N+1} and relax back into the ground state. In Fig. 2.3 **IV** such an *excited orbital state* μ^*_{QD} is shown. They appear as additional line parallel to the diamond boundary lines when $|eV_{SD}| > \delta E$ [91].

Besides excited state transition there are also higher order tunneling processes that can occur. With increased tunnel coupling $\Gamma_{S/D}$ *co-tunneling* becomes possible. Hereby, two tunneling processes happen in a very short time interval via a virtual intermediate non-resonant state. We differentiate between *elastic co-tunneling*, where the QD is left in its ground state and *in-elastic co-tunneling*, where the QD is left in an excited state (or relaxed from an excited state into the ground state). In elastic co-tunneling at low bias an electron can tunnel from one lead into an energetically forbidden forbidden state $\delta = \mu^*_{QD} - \mu_{QD}$ above the potential in the leads and then tunnel into the other lead. Given strong enough tunnel coupling to the leads $\Gamma_{S/D}$, the energy of the total system is uncertain enough to allow for this process. In an in-elastic co-tunneling process the bias voltage is large enough to populate the excited state, i.e $|eV_{SD}| \geq \delta$.

In a two electron tunneling process one electron can tunnel from the source into the excited state, while another electron can tunnel from the QD ground state into the drain. This will leave the QD in the excited state. To relax the QD back into its ground state another electron lacking energy δ can tunnel through the QD or an electron tunneling from either source of drain can be excited above the potential and relax the QD without charge transfer [77, 104–106]. The onset of inelastic co-tunneling $|eV_{SD}| > \delta$ is visible in a Coulomb diamond measurement as step in conductance. It can be used for precise measurement of the QDs excitation and level spectrum [106].

2.1.4. Quantum dot states in a magnetic field

The influence of a magnetic field B on a QD can be fairly complex. In general it can be assumed that the charging energy E_C and the lever arms α_i are independent of an external applied magnetic field. The magnetic field dependence of the electrochemical potentials of the QD then solely stems from the orbital levels $E_N(B)$ of the QD. A quantitative understand of the energy levels are only possible for few electron QD (usually less than 10 electrons), as the confinement potential of QDs are usually not very symmetrical [77]. In chapter 8 we will discuss the behavior of a many electron double QD in magnetic field with a very simplified model.

At zero magnetic field a QD exhibits a two-fold spin degeneracy. Applying an external finite magnetic field will lift the spin degeneracy. The spins of the electrons on the QD will be aligned either parallel or anti-parallel with the external field. The change in energy of the orbital levels is then given by

$$E_{N,s}(B) = \gamma B^2 \pm s g^*_N \mu_B B, \tag{2.6}$$

where the first term is the diamagnetic shift [77] which affects all levels equally. The parameter γ can be experimentally determined. The second term is the Zeeman-shift [107] with the Bohr magneton μ_B, the normalized g-factor of the Nth energy level g^*_N, and $s = \pm\frac{1}{2}$ is the spin quantum number along the axis of the magnetic field.

2.1.5. Double quantum dots

In the above discussion we have only looked at single QDs. We will now introduce the concept of double quantum dots (DQD). A serial DQD can be formed by adding a third tunnel barrier. This allows for electron and spin interaction between the two QD creating a system of major interest for both charge and spin qubits. We will discuss our results with a serial DQD coupled to a high-impedance resonator in chapters 7 and 8. A DQD can also be formed by adding a purely capacitive coupling between two QDs, a so-called parallel DQD. For this work we will focus on serial QDs, but some results with parallel QDs will be briefly discussed in chapter 6.

In Fig. 2.4(a) a schematic of a typical DQD and the capacitance model is shown. The QDs are capacitively and tunnel coupled to their respective source-drain contacts with $C_{S/D}$ and $\Gamma_{S/D}$. They are also coupled to each other with the mutual capacitance C_M and tunnel coupling Γ_M. Each QD has

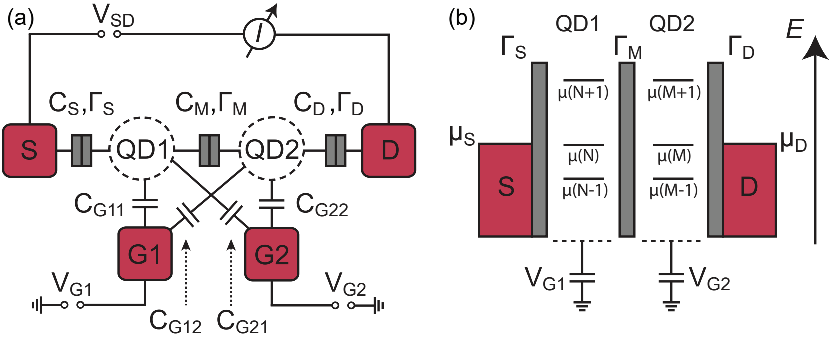

Figure 2.4. Schematic of circuit diagram and electrostatic model of a double quantum dot (DQD) (a) Capacitance model and a typical circuit diagram of a DQD. QD1 (QD2) is coupled to the source S (drain D) with capacitance C_S (C_D) and tunnel coupling Γ_S (Γ_D). The two QDs are coupled to each other with the mutual capacitance C_M and tunnel coupling Γ_M. The plunger gate G1 (G2) tunes QD1 (QD2) with capacitance C_{G11} (C_{G22}) and has a cross-capacitance to QD2 (QD1) of C_{G12} (C_{G21}). (b) Schematic of the energy diagram of the DQD. The electron population in QD1 (QD2) is given by N (M). The electrochemical potential of the QDs μ_N and μ_M and the source μ_S and drain μ_D are shown. With the plunger gate voltage $V_{G1/2}$ the electrochemical potential in the QDs can be tuned. Adapted from [81, 100, 101].

its own plunger gate G1 or G2 to tune the respective energy levels. The gates are purely capacitively coupled with C_{G11} for QD1 and C_{G22} for QD2. Due to limitation in the fabrication process and device design, some crosstalk between the gates and the QDs cannot be avoided. Therefore the model also includes cross-capacitances C_{G12} from G1 to QD2 and C_{G21} from G2 to QD1. We will refer to the electron population of QD1 (QD2) with N (M). In Fig. 2.4 (b) an example of an electrochemical potential configuration $\mu_{1,2}(N, M)$ is shown.

Charge stability diagram

A thorough derivation of the capacitance model and the charge stability diagram can be found in refs. [77, 81]. We will focus on the main results and leave it to the interested reader to consult the references for the full derivation. We will assume linear response, such that $V_{SD} \sim 0$ and $\mu_S = \mu_D \sim 0$. Then neglecting cross capacitances and stray capacitances, the charging energies of the individual dots $E_{C1(2)}$ are as follows

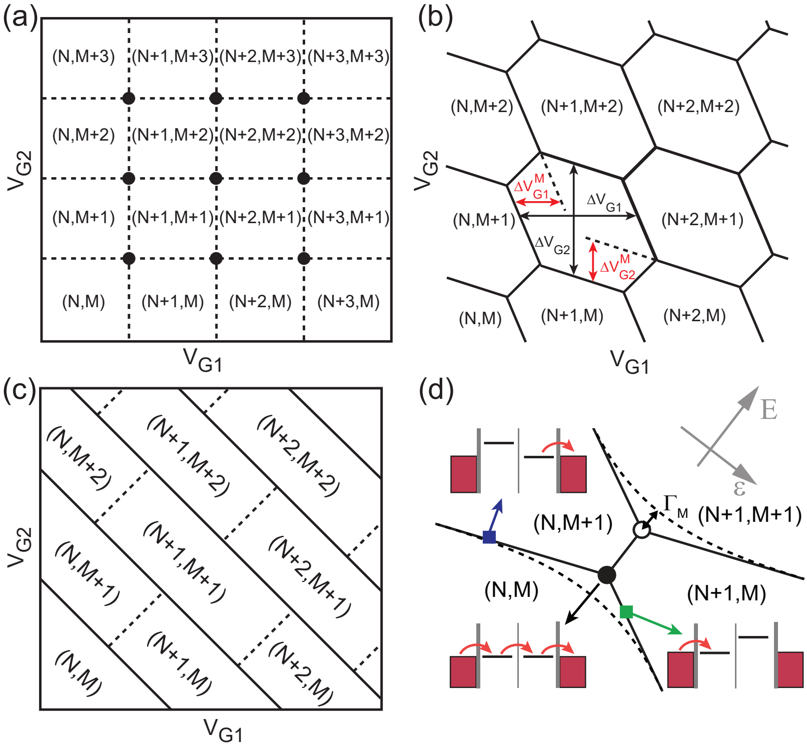
(a)
(N,M+3)
(N+1,M+3)
(N+2,M+3)
(N+3,M+3)
(N,M+2)
(N+1,M+2)
(N+2,M+2)
(N+3,M+2)
(N,M+1)
(N+1,M+1)
(N+2,M+1)
(N+3,M+1)
(N,M)
(N+1,M)
(N+2,M)
(N+3,M)
V_G2
V_G1
(b)
(N,M+2)
(N+1,M+2)
(N+2,M+2)
(N,M+1)
(N+2,M+1)
ΔV^M_G1
ΔV_G1
ΔV_G2
ΔV^M_G2
(N,M)
(N+1,M)
(N+2,M)
V_G2
V_G1
(c)
(N,M+2)
(N+1,M+2)
(N+2,M+2)
(N,M+1)
(N+1,M+1)
(N+2,M+1)
(N,M)
(N+1,M)
(N+2,M)
V_G2
V_G1
(d)
E
ε
Γ_M
(N,M+1)
(N+1,M+1)
(N,M)
(N+1,M)

Figure 2.5. Charge stability diagram of a DQD. The charge stability diagram is shown for (a) weak interdot coupling $C_M \to 0$, (b) intermediate coupling, and (c) strong coupling $C_M/C_{1/2} \to 1$. The intermediate regime (b) shows the typical honeycomb pattern of a DQD. From its dimension the gate capacitance and mutual capacitance can be extracted. (c) shows a detailed schematic of a interdot transition between two triple points. At the triple points three charge states are degenerate in energy. At the interdot transition line two charge states (N, M+1) and (N+1, M) are degenerate. The energy and detuning axes of the DQD are illustrated at the top right. Adapted from refs. [81, 100, 101]

$$E_{C1} = \frac{e^2}{C_1}\left(\frac{1}{1-\frac{C_m^2}{C_1C_2}}\right) \tag{2.7}$$

$$E_{C2} = \frac{e^2}{C_2}\left(\frac{1}{1-\frac{C_m^2}{C_1C_2}}\right). \tag{2.8}$$

The electrostatic coupling energy E_{Cm}, which describes the energy needed to add one electron to one QD, while the occupation on the other QD is kept constant. We get

$$E_{Cm} = \frac{e^2}{C_m}\left(\frac{1}{\frac{C_1C_2}{C_m^2}-1}\right), \tag{2.9}$$

where $C_{1(2)}$ denotes the sum of all capacitances acting on QD1 (2). $C_{1(2)} = C_{L(R)} + C_{G1(2)} + C_m$ [81]. The behavior of the DQD depends strongly on the mutual capacitance C_m, as is illustrated in the charge stability diagram in Fig. 2.5 (a)-(c), each line represents the addition or removal of one electron from one of the QDs. The two limiting cases $C_m = 0$ (a), $C_m/C_{1(2)}$ (c), and the case of intermediate coupling (b) are shown. For $C_m = 0$ the two QDs are independent of each other. They are completely decoupled and the gates only affect their respective QD. This is results in perfectly horizontal and vertical single charging lines. To measure charge transport an electron has to tunnel from source do drain through both QDs. For small bias this is only possible at the intersection points of the single charging lines, when all the chemical potential align; $\mu_S = \mu_{QD1} = \mu_{QD2} = \mu_D$.

In reality there will always be some mutual capacitance C_m and cross-coupling. As is shown in (b) the single charging lines will have a finite slope and the intersection points split into two triple points. This creates a hexagonal pattern, often called *honeycomb pattern*. Compared to (a), where four charge case co-exist at the corner points of the squares, these split into the *triple points*, where three charge states (N,M), (N,M+1) and (N+1,M) are energetically degenerate. Electron transport through the DQD is only possible at these points. There are two possible processes: (N,M) → (N+1,M) → (N,M+1) → (N,M) or (N+1,M+1) → (N+1,M) → (N,M+1) → (N+1,M+1). The first process describes the sequential tunneling of an electron through the DQD, while the second can be seen as the sequential tunneling of a hole. The separation between the two triple points gives the energy difference between the two processes which is equal to E_{Cm}. A schematic of a pair of triple points is shown in (d). The dimension of the honeycomb cell can be used to extract the capacitances of the QDs and the mutual capacitance. From the height ΔV_{G1} and the width ΔV_{G2} we get

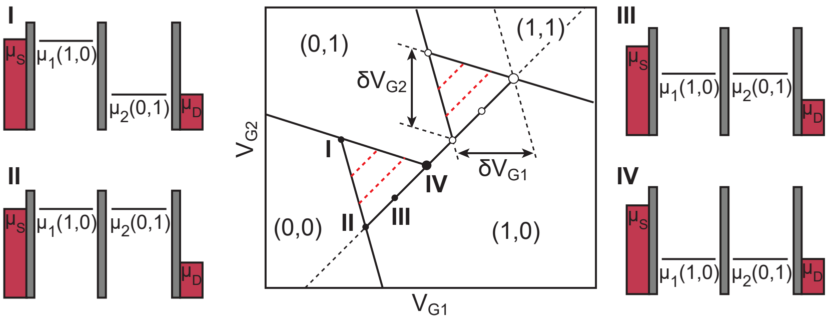

Figure 2.6. Transport at finite bias voltage through DQD. Applying a finite bias to a DQD evolves the triple points into bias triangles. Electron transport is only allowed within these triangles. The dimensions of the bias triangles $\delta V_{G1/G2}$ allow the extraction of the gate lever arms $\alpha_{1/2}$. The illustrations (**I-IV**) show the electrochemical potential at the indicated points on the bias triangles. For large enough V_{SD} excited states will be visible as lines at finite detuning in the bias triangles, as illustrated by the red dashed lines. Adapted from refs. [81, 100, 101].

$$C_{G1/G2} = \frac{|e|}{\Delta V_{G1/G2}}. \tag{2.10}$$

From the distance between the triple point the mutual capacitance can be extracted.

$$C_m = C_{1/2}\frac{\Delta V^m_{G1/G2}}{\Delta V_{G1/G2}} \tag{2.11}$$

In the presence of finite tunnel coupling Γ_M between the QDs. The degeneracy in the triple points is lifted and the states of the DQD hybridize to a symmectric and antisymmetric state. This leads to the sharp degeneracy points of the honeycomb becoming rounded into an avoided crossing, as illustrated from (d). The distance between the avoided crossing and the triple point is given by the strength of Γ_M. In the extreme case of large tunnel coupling and when $C_m/C1(2) \to 1$ becomes the dominant capacitance the DQD behaves as a single QD with charge N+M and capacitance $C_1 + C_2 - C_m$. As shown in (a) the charge stability diagram changes to diagonal parallel lines [77, 81].

Bias triangles

Let us now consider the case of an asymmetric finite bias $|V_{SD}| \geq 0$ applied on the source contact, such that $\mu_S = -|e|V_{SD}$ and the drain contact is grounded $\mu_D = 0$. With a bias applied the triple points evolve into triangular shaped region referred to as *bias triangles* as is shown in Fig. 2.6. Within this triangles electron transport through the DQD is possible. Their boundaries are determined by the conditions $-|e|V_{SD} = \mu_S \geq \mu_1$, $\mu_1 \geq \mu_2$, and $\mu_2 \geq \mu_D = 0$. Outside of these bias triangles transport is blocked. The dimensions of the bias triangles δV_{G1} and δV_{G2} are related to the applied bias voltage and the lever arms $\alpha_{1/2}$ of gates $V_{G1/G2}$ as follows

$$\alpha_{1/2}\delta V_{G1/G2} = \frac{C_{G1/G2}}{C_{1/2}}|e|\delta V_{G1/G2} = |eV_{SD}|. \tag{2.12}$$

Together with equations 2.10 and 2.11 the total capacitances $C_1/2$ and the mutual capacitance C_m can be extracted.

So far, we have only looked at the case where a single energy level lies in the bias window. Of course it is also possible for excited states to enter the bias window. These will be visible as lines parallel to the base line of the triangles at finite detuning. This is illustrated in Fig. 2.6 by the red dashed lines [81].

2.1.6. Two-level systems

The charge qubit

We have already discussed above that finite inter-dot tunnel coupling smooths out the sharp triple points and leads to an avoided crossing in the charge stability diagram. We will now look at these avoided crossings in more detail as a platform for qubits.

In general completely filled QD energy levels do not contribute to transport, as such we neglect these completely filled levels to simplify our picture. We are left with two cases. The odd case, when there is only one electron in the DQD and the even case, when there are two. It should be noted, that while this is a good approximation for few electron DQD, the orbital wavefunctions for many-electron DQD can become very complex leading to a much more complicated picture [81]. We will later discuss such a many-electron DQD in chapter 8 and show that we can explain a lot of its behavior with this very simplified picture.

Odd parity

We will look at the odd parity first, where one electron resides in the DQD. We can describe this system with a basis of $\{|L\downarrow\rangle, |L\uparrow\rangle, |R\downarrow\rangle, |R\uparrow\rangle\}$, where L,R denotes if the electron is in the left or right QD and $\uparrow,\downarrow$ denotes the

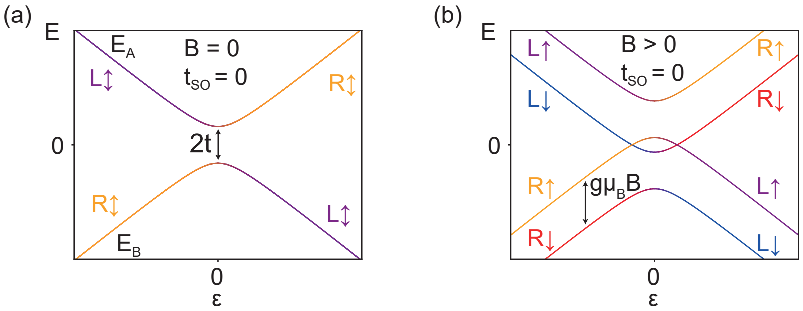

Figure 2.7. Charge qubit with odd parity. The energy levels in dependence of the detuning ϵ for the odd parity without spin-orbit interaction. (a) Energy levels without magnetic field. The uncoupled states $L\updownarrow$ and $R\updownarrow$ hybridize to the bonding and anti-bonding states E_B and E_A, which are split by the two times the tunnel coupling $2t$. States with different spin do not couple. (b) Energy levels with finite magnetic fields. The states are split into $R_\downarrow$, $R_\uparrow$, $L_\downarrow$, and $L_\uparrow$ with the energy difference given by the Zeeman-energy. As before states with different spin do not couple.

alignment of the electron spin with the external magnetic field. The system can be described by the Hamiltonian

$$\mathcal{H}_{\mathrm{odd}} = \mathcal{H}^0_{\mathrm{odd}} + \mathcal{H}^Z_{\mathrm{odd}} + \mathcal{H}^{\mathrm{SOI}}_{\mathrm{odd}}, \tag{2.13}$$

where the first term describes the detuning and spin independent tunneling between the QDs, the second term the Zeeman Hamiltonian, and the third term the spin-dependent tunneling due to spin-orbit interaction.

Assuming no magnetic field and no spin-orbit interaction for the moment, we obtain

$$\mathcal{H}^0_{\mathrm{odd}} = \frac{\epsilon}{2}\hat{\tau}_z + t\hat{\tau}_x, \tag{2.14}$$

with detuning $\epsilon = E_L - E_R$, inter-dot tunnel couplig t, and the charge Pauli matrices $\hat{\tau}_{x,y,z}$ [83, 108].

In a system without tunnel coupling $t = 0$ the electron is either localized on the left or right QD with energy E_L and E_R respectively. Note, that we have referred to t as Γ_M previously. We will refer to it as t for the parts of this thesis concerning qubits and resonators to stay consistent with literature. Adding finite tunnel coupling to this system delocalizes the electron over the entire DQD. This creates delocalized bonding (E_B) and anti-bonding (E_A) states with energies

$$E_B = E_M - \sqrt{\frac{1}{4}\epsilon^2 + |t|^2} \tag{2.15}$$

$$E_A = E_M + \sqrt{\frac{1}{4}\epsilon^2 + |t|^2}, \tag{2.16}$$

with mean energy $E_M = \frac{1}{2}(E_L + E_R)$ and detuning $\epsilon = E_L - E_R$. The energy difference between the two states is then

$$\Delta E = E_A - E_B = \sqrt{\epsilon^2 + (2|t|)^2}. \tag{2.17}$$

As we see from Fig. 2.7a) the effect of the tunnel coupling is strongest at zero detuning, where the splitting between the bonding and anti-bonding state is given by $2|t|$. At large detuning they approach the uncoupled energies E_1 and E_2 [81]. Note that the spin-down and spin-up states are degenerate at zero magnetic field. They will Zeeman-split at a finite magnetic field, described by the Hamiltonian term

$$\mathcal{H}^Z_{\text{odd}} = \frac{1}{2}\mu_B g_{L,R} B \hat{\sigma}_z, \tag{2.18}$$

where $g_{L,R}$ are the g-factors of the left and right QD, respectively, μ_B the Bohr magneton, and $\hat{\sigma}_{x,y,z}$ the Pauli spin matrices [83, 108]. The Zeeman-split energy levels are illustrated in Fig. 2.7(b).

Even parity

We will now move on to the even parity, where there are two electrons in the DQD. This case allows for three charge states (2,0), (0,2), and (1,1). We can describe this system with the basis $\{S_{1,1}, T^-_{1,1}, T^0_{1,1}, T^+_{1,1}, S_{2,0}, T^-_{2,0}, T^0_{2,0}, T^+_{2,0}\}$. Here, the charge state is given by the subscript tuple and the spin states by the singlet

$$S = \frac{1}{\sqrt{2}}(|\uparrow\downarrow\rangle - |\downarrow\uparrow\rangle), \tag{2.19}$$

and triplets

$$T^- = |\downarrow\downarrow\rangle\,, \quad T^0 = \frac{1}{\sqrt{2}}(|\uparrow\downarrow\rangle + |\downarrow\uparrow\rangle), \quad T^+ = |\uparrow\uparrow\rangle\,. \tag{2.20}$$

As for the even parity, we can describe the Hamiltonian in three parts [82]

$$\mathcal{H}_{\text{even}} = \mathcal{H}^0_{\text{even}} + \mathcal{H}^Z_{\text{even}} + \mathcal{H}^{\text{SOI}}_{\text{even}}, \tag{2.21}$$

again the first part describes the electrostatic potential and spin independent tunneling, the second the Zeeman Hamiltonian, and the third part the spin dependent tunneling due to spin-orbit interaction.

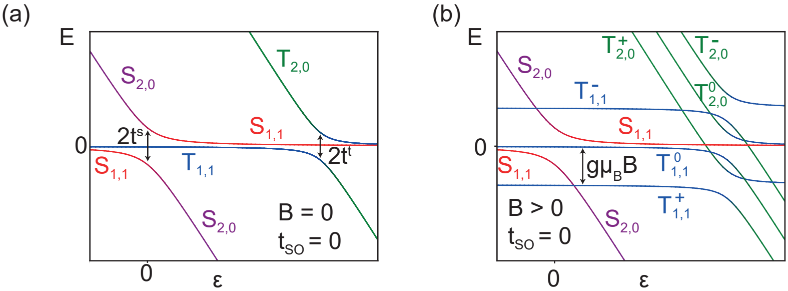

Figure 2.8. Charge qubit with even parity. The energy levels in dependence of the detuning ϵ for the odd parity without spin-orbit interaction. (a) Energy levels without magnetic field. The singlets (red, purple) and triplet (blue, green) state hybridize and anti-cross with a splitting given by twice their respective tunnel coupling. States of different spin texture do not hybridize. (b) Same as (a) but with finite magnetic field. The triplet states are Zeeman-split, while the singlets remain unaffected.

As for the odd parity, we will ignore the Zeeman and spin-orbit terms for the moment. This yields the Hamiltonians for the singlet and triplet tunneling states

$$\begin{aligned}\mathcal{H}^{0,S}_{\text{even}} &= -\epsilon \left|S_{2,0}\right\rangle \left\langle S_{2,0}\right| + t^S \left|S_{1,1}\right\rangle \left\langle S_{2,0}\right| + \text{h.c.},\\ \mathcal{H}^{0,T}_{\text{even}} &= (\Delta_{\text{ST}} - \epsilon) \sum_{\pm,0} \left|T^{\pm,0}_{2,0}\right\rangle \left\langle T^{\pm,0}_{2,0}\right| + t^T \sum_{\pm,0} \left|T^{\pm,0}_{1,1}\right\rangle \left\langle T^{\pm,0}_{2,0}\right| + \text{h.c.}\end{aligned}$$

Here, $t^{S,T}$ are the spin-conserving tunnel rates for singlet and triplet states, respectively, Δ_{ST} is the single QD singlet-triplet level splitting, and the detuning $\epsilon = E_L - E_R$ is given as before. The energy levels of this Hamiltonian are plotted as a function of ϵ in Fig. 2.8(a). At zero detuning the singlet states are the ground state and the triplets $T^{\pm,0}_{1,1}$ are degenerate at zero energy, while the triplets $T^{\pm,0}_{2,0}$ are at higher energy, given by Δ_{ST}. For increasing detuning the $T^{\pm,0}_{1,1}$ states stay at constant energy, while the $T^{\pm,0}_{2,0}$ states decrease in energy. The characteristics are similar to the odd case, where states with the same spin-texture hybridize with an anti-crossing given by twice their tunnel rate $2t^{S,T}$.

If a finite magnetic field is added to the system, the Zeeman Hamiltonian is described by

$$\mathcal{H}^Z_{\text{even}}/\mu_B = B \sum_{\pm} \left(\pm \frac{g_l + g_r}{2} \left|T^{\pm}_{1,1}\right\rangle \left\langle T^{\pm}_{1,1}\right| \pm g_l \left|T^{\pm}_{2,0}\right\rangle \left\langle T^{\pm}_{2,0}\right| \right), \tag{2.22}$$

where $g_{L,R}$ are the g-factors of the left and right QD, respectively. The energy levels for this system are plotted in Fig. 2.8(b) with $g_L = g_R$. The spin-polarized triplet states are Zeeman-split by $g\mu_B B$, while the spinless states remain unaffected. We observe, that for large enough B and negative g-factors the triplet state $T^+_{1,1}$ becomes the ground state at zero detuning. Since there is no coupling between states of different spin-texture the singlets and triplets cross without interaction.

The spin qubit

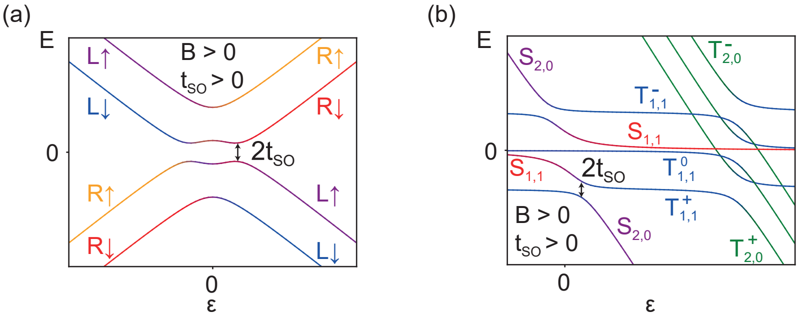

Figure 2.9. Spin qubit for odd and even parity. Energy levels as a function of detuning ϵ including finite magnetic field B and finite spin-flip tunnel amplitude t_{SO} for the odd (a) and even (b) parity.

In the previous we have investigated the charge qubit, where states of different spin-texture do not hybridize. In order to form a spin qubit another interaction is needed to couple different spin states. In our experiments this is done by intrinsic spin-orbit interaction of the material. We model this in the Hamiltonian with a spin-flipping tunneling amplitude t_{SO}. The spin-orbit term of the odd parity Hamiltonian introduced in eq. 2.13 is given by [83, 108]

$$\mathcal{H}^{\mathrm{SOI}}_{\mathrm{odd}} = t_{SO}\hat{\tau}_y\hat{\sigma}_y. \tag{2.23}$$

The resulting energy levels are plotted in Fig. 2.9(a). The $|L\downarrow\rangle$ (red) ($|L\uparrow\rangle$, yellow) and the $|R\uparrow\rangle$ (purple) ($|R\downarrow\rangle$, blue) hybridize and form a two-level system with the energy splitting given by $2t_{SO}$.

Assuming the same t_{SO} for all states in the even parity adds the following spin-orbit term of the even Hamiltonian in eq. 2.21 [82]

$$\mathcal{H}^{\mathrm{SOI}}_{\mathrm{even}} = t_{\mathrm{SO}}\left(|T^0_{1,1}\rangle\langle S_{2,0}| + \sum_{\pm} \pm|T^{\pm}_{1,1}\rangle\langle S_{2,0}|\right) + \mathrm{h.c.}$$

The energy levels are plotted as a function of ϵ in Fig. 2.9(b) with finite B and t_{SO}. We observe avoided crossing between $S_{2,0}$ and $T_{1,1}$ with a splitting of $2t_{SO}$.

2.2. Cavity quantum electrodynamics with quantum dots

We have previously introduced QDs and specifically DQDs as a two level system ("qubit"). However, to properly build up an architecture for quantum processing, qubits have to coupled in a coherent fashion. Photons can act as a mobile carrier for quantum information between quantum systems. This photon-qubit interaction can be further enhanced by confining the photons to a cavity. In the following we will give a very brief introduction to superconducting resonators and their coupling to a QD two-level system. For a more in depth review, please refer to Refs. [64, 65, 109–111]

2.2.1. Coupling a resonator to a charge qubit

On the most basic level, a cavity QED system has two components: a cavity with well-defined photon modes at a resonance frequency ω_r and a two-level quantum system (qubit) with a transition energy $\hbar\omega_q$, between the two levels, close to $\hbar\omega_r$. In optics, a cavity is constructed by two reflecting mirrors. In between the mirrors the light forms standing waves with discrete modes. Analogously, in circuit quantum electro dynamics (cQED) a superconducting resonator shows a similar discrete spectrum of modes in the microwave range [109, 110].

In our experiments the resonator is capacitively coupled to the DQD two-level system via a gate or a contact. We have already described the DQD two-level system above, now we will add the coupling of the cavity. Electric dipole interactions couple the resonator cavity photons to the electrons in the DQD with strength g_c, the so-called charge-photon coupling rate. The strength of g_c is given by the product of the dipole moment $\vec{d}$ of the DQD and the vacuum electric field E_0 of the cavity. For a charge qubit the charge states are most strongly hybridized at zero detuning $\epsilon = 0$ of the energy levels in the left and right QD. This results in a maximized $g_c = \vec{d} \cdot \vec{E_0}/\hbar$. If the DQD system is detuned from zero ($|\epsilon| > 0$) the charge states are weakly admixed and the effective dipole moment is reduced by $g_c(\epsilon) = \frac{2t}{\sqrt{\epsilon^2+4t^2}} g_c(\epsilon = 0)$ [110], where t is the inter-dot tunnel rate.

By coupling a DQD to a superconducting resonator, the energy landscape of the DQD is affected by the electric field of the resonator. Since the dimension of the DQD are much smaller than the wavelength of the electromagnetic field inside the resonator, we can assume that the electric field is constant for the

DQD [110]. The single-two level system coupled to a single cavity mode can be described by the Hamiltonian [64, 110, 112]

$$H = \hbar\omega_r \left(\hat{a}^\dagger\hat{a} + \frac{1}{2}\right) + \frac{1}{2}\hbar\omega_q\hat{\sigma}_z - \vec{d}\cdot\vec{E}_0\hat{\sigma}_x(\hat{a} + \hat{a}^\dagger), \tag{2.24}$$

with the quantized bosonic creation and annihilation operators $\hat{a}$ and $\hat{a}^\dagger$, ω_r the cavity resonance frequency, ω_q the qubit transition frequency, and the Pauli operators $\hat{\sigma}_{x,y,z}$. The first term describes the bosonic cavity modes, the second term the qubit mode, and the last term the dipolar interaction between the qubit and the resonator.

We can express the interaction dipolar Hamiltonian H_{int} with the fermionic ladder operators $\hat{\sigma}_x = (\hat{\sigma}_+ + \hat{\sigma}_-)/2$ and our definition above of the charge coupling strength $g_c = \vec{d}\cdot\vec{E}_0/\hbar$, yielding

$$H_{int} = \hbar g_c \left(\hat{\sigma}_-\hat{a}^\dagger + \hat{\sigma}_+\hat{a} + \hat{\sigma}_+\hat{a}^\dagger + \hat{\sigma}_-\hat{a}\right) \tag{2.25}$$

The first two terms $\hat{\sigma}_-\hat{a}^\dagger + \hat{\sigma}_+\hat{a}$ describe the resonant interaction between the resonator and qubit, i.e. the transition from the ground (excited) to the excited (ground) state together with the annihilation (creation) of a photon. The last two terms $\hat{\sigma}_+\hat{a}^\dagger + \hat{\sigma}_-\hat{a}$ describe the anti-resonant interaction, i.e the transition from the ground (excited) to the excited (ground) state combined with the creation (annihilation) of a photon. If the resonator frequency $\omega_r/2\pi$ and the qubit frequency $\omega_q/2\pi$ are close and the coupling strength is much smaller than the transition frequencies $g_c \ll \omega_r, \omega_q$, these transitions are highly unlikely. We therefore perform the rotating wave approximation and neglect these two terms. This gives the Jaynes-Cummings (JC) Hamiltonian [113]

$$H_{JC} = \hbar\omega_r \left(\hat{a}^\dagger\hat{a} + \frac{1}{2}\right) + \hbar\frac{\omega_q}{2}\hat{\sigma}_z + \hbar g_c(\hat{\sigma}_-\hat{a}^\dagger + \hat{\sigma}_+\hat{a}) \tag{2.26}$$

The diagonalization of this Hamiltonian gives the ground state $|\downarrow, 0\rangle$ and dressed states [64, 111]

$$|+, n\rangle = \cos(\theta_n)\,|\uparrow, n\rangle + \sin(\theta_n)\,|\downarrow, n+1\rangle \tag{2.27}$$

$$|-, n\rangle = -\sin(\theta_n)\,|\uparrow, n\rangle + \cos(\theta_n)\,|\downarrow, n+1\rangle \tag{2.28}$$

with the eigenergies

$$E_{\downarrow,0} = \hbar\frac{\omega_q - \omega_r}{2} \tag{2.29}$$

$$E_{\pm,n} = (n+1)\hbar\omega_r \pm \frac{\hbar}{2}\sqrt{4g_c^2(n+1) + (\omega_q - \omega_r)^2}, \tag{2.30}$$

with the mixing angle θ_n defined as

$$\theta_n = \frac{1}{2}\tan^{-1}\left(\frac{2g_c\sqrt{n+1}}{\omega_q - \omega_r}\right). \tag{2.31}$$

In our experiments in chapters 7 and 8 we will study transitions from the ground to the dressed state with one photonic excitation in the cavity. Therefore $n = 0$ for us and the transition frequency is $\omega_\pm = (E_{\pm,0} - E_{\downarrow,0})/\hbar$. Explicitly, this is

$$\omega_\pm = \frac{\omega_0 + \omega_q}{2} \pm \frac{1}{2}\sqrt{4g^2 + (\omega_0 - \omega_q)^2}. \tag{2.32}$$

2.2.2. Input-Output theory

Input-output theory offers a more direct approach to model the resonator-qubit system. The following paragraphs pertaining to input-output theory were derived and written by Patrick P. Potts for our submitted paper [114] and are used in chapter 8, which discusses the paper.

To derive the response of the resonator, we use the equations of motion [115]

$$\begin{aligned}\partial_t\langle\hat{a}\rangle(t) = -i\omega_0\hat{a}(t) - ig\langle\hat{\sigma}\rangle(t) - \frac{\kappa}{2}\langle\hat{a}\rangle(t)\\ - \sqrt{\kappa_1}\langle\hat{b}_{\mathrm{in},1}\rangle(t) - \sqrt{\kappa_2}\langle\hat{b}_{\mathrm{in},2}\rangle(t),\\ \partial_t\langle\hat{\sigma}\rangle(t) = -i\omega_q\langle\hat{\sigma}\rangle(t) + ig\langle\hat{a}\hat{\sigma}_z\rangle(t) - \gamma\langle\hat{\sigma}\rangle(t).\end{aligned} \tag{2.33}$$

The input couplings are denoted by κ_j and the operators $\hat{b}_{\mathrm{in},j}(t)$ capture a coherent drive in port j. In our experiments $\kappa_1 \approx \kappa_2 \approx \kappa/2$ as the resonator is symmetrically coupled and operates in the strongly over-coupled regime. The output of the cavity can be computed from the input-output relation [115]

$$\langle\hat{b}_{\mathrm{out},j}\rangle(t) = \langle\hat{b}_{\mathrm{in},j}\rangle(t) + \sqrt{\kappa_j}\langle\hat{a}\rangle(t). \tag{2.34}$$

To solve these equations, we approximate [116, 117]

$$\langle\hat{a}\hat{\sigma}_z\rangle(t) \to \langle\hat{a}\rangle(t)\langle\hat{\sigma}_z\rangle, \tag{2.35}$$

where $\langle\hat{\sigma}_z\rangle$ is evaluated at steady state and captures the difference between the population of the excited qubit state and the ground state, accounting for operation at larger temperatures or drive strengths. In our experiments, we operate in the linear regime, $\langle\hat{\sigma}_z\rangle = -1$.

To compute the transmission amplitude, we solve Eqs. (2.33) and (2.34) upon Fourier transformation and set $\langle\hat{b}_{\mathrm{in},2}\rangle(t) = 0$. This results in the transmission amplitude

$$\tau(\omega) = -\frac{\langle\hat{b}_{\mathrm{out},2}\rangle(\omega)}{\langle\hat{b}_{\mathrm{in},1}\rangle(\omega)} = \sqrt{\kappa_1\kappa_2}A(\omega), \tag{2.36}$$

where the minus sign accounts for the phase difference of π between the input and the output port ($\lambda/2$ resonator) and

$$A(\omega) = \frac{\gamma + i(\omega_q - \omega)}{[\kappa/2 + i(\omega_0 - \omega)][\gamma + i(\omega_q - \omega)] - g^2\langle\hat{\sigma}_z\rangle}. \tag{2.37}$$

In the main text, the absolute value squared of this quantity normalized by its maximal value is shown.

The phase of the transmitted signal is given by

$$\begin{aligned}\varphi(\omega) &= -\arctan(\Lambda),\\ \Lambda &= \frac{-2(\omega_q-\omega)g^2\langle\hat{\sigma}_z\rangle - 2(\omega_0-\omega)[\gamma^2+(\omega_q-\omega)^2]}{\kappa[\gamma^2+(\omega_q-\omega)^2]-2\gamma g^2\langle\hat{\sigma}_z\rangle}.\end{aligned} \tag{2.38}$$

As examples, the phase and amplitude of the bare resonance in Coulomb blockade is simultaneously fit in Fig. D.1(a) and in Fig. D.2 the same is done for a linecut of Fig. 8.4(a) at 0.25 T.

Estimation of the photon number

Similarly, we may obtain $\langle\hat{a}\rangle(t)$ by solving Eqs. (2.33). Using $\langle\hat{b}_{\mathrm{in},1}\rangle(t) = \exp(-i\omega_p t)\sqrt{P_{\mathrm{in}}/\omega_p}$, where P_{in} denotes the power in the input field, we find

$$\langle\hat{a}\rangle(t) = -\sqrt{\frac{\kappa_1 P_{\mathrm{in}}}{\hbar\omega_p}}e^{-i\omega_p t}A(\omega_p). \tag{2.39}$$

In the low-drive regime we consider here, we estimate the photon number as

$$n = |\langle\hat{a}\rangle|^2 = \frac{\kappa_1 P_{\mathrm{in}}}{\hbar\omega_p}|A(\omega_p)|^2, \tag{2.40}$$

where we approximate $\kappa_1 \simeq \kappa/2$.

2.2.3. Coupling a resonator to a spin qubit

The quantum coherence lifetime of spins in QDs or defects extends from microseconds [98, 118, 119] to nearly a second [120]. In contrast, the coherence of charge qubits in DQD is typically limited to a few nanoseconds [97, 121, 122]. Moving from charge qubits to spin qubits is therefore of major interest for quantum information processing. Coupling the spin states to a common resonator mode allows to couple two qubits over large distance [74, 75]. However, the spin, unlike the charge, of an electron (or hole) does not directly couple to the electric field of a resonator. To induce such a coupling the spin and charge degrees of freedom need to be hybridized, such that the spin is endowed with an effective electric dipole. This hybridization has been achieved by spin exchange interaction in triple QDs [123], intrinsic spin-orbit coupling of the material [108, 124], or manipulation of magnetic fields for example by integration of micromagnets in the device architecture [71, 74, 75, 118, 125]. In our experiment in chapter 8 we will make use of the intrinsic spin-orbit interaction of an InAs NW. Note, that the above formulas for the interaction of a microwave cavity and a charge qubit also holds for spin qubits, where the charge-photon coupling g_c is replaced with the spin-photon coupling g_s.

2.3. Superconductivity

In this section we will give a brief introduction to superconductivity following references [126] and [127]. We will focus on an intuitive picture for understanding and refer the interested reader to the above references. After we introduced the general concept of superconductivity we will focus on the phenomena that arise when a QD is coupled to a superconductor. As we have discussed in the above section, QDs only allow the tunneling of successive discrete charges. Electrons are strongly confined and repel each other. In contrast in a superconductor, electrons feel an attractive force, that binds them into Cooper-pairs. Therefore, coupling a superconductor to a QD creates a system, where the repulsion of a QD and the attraction of a superconductor compete. These interplay gives rise to a multitude of phenomena, such as Andreev-bound states [51, 128–131], Josephson effect [132, 133], and possibly Majorana bound states [44]. We will look at two such phenomena in particular the induced superconducting gap into a semiconductor and Cooper pair islands.

The most striking feature of a superconductor is its vanishing electrical resistance when cooled down below a critical temperature T_C. This was first observed by Kamerlingh Onnes in 1911 [134]. Some commonly used superconductors are among others Al, Nb or Pb. Another feature of superconductors is the *Meissner-Ochsenfeld effect*, which can also be described as a perfect diamagnetism. Externally applied magnetic fields are expelled from the inside of a superconductor by induced dissipationless surface supercurrents. At a critical field $B_C = \mu_0 H_C$ it is energetically favorable for the superconductor to switch to the normal state and superconductivity breaks down [126]. Macroscopic description of superconductivity explaining these features have been made by the thermodynamic *Ginzburg-Landau* theory [135] and the *London equations* [127]. A microscopic description was given in 1957 by Bardeen, Cooper, and Schrieffer in the BCS theory of superconductivity [136].

2.3.1. Cooper pairs and superconducting gap

The BCS theory is based on the realization by Cooper that the fermionic ground state of the electrons is unstable against any net attraction between two individual electrons. These electrons bind together to form a Cooper pair, which obey bosonic statistics [137]. This attractive force stems from the interaction of the electron with the ion lattice of the superconductor mediated by phonons. In short an electron passing through the ion lattice deforms the positively charged ion lattice due to its negative charge. This creates a retarded positively charged polarization cloud in its path. This in turn will act as an attractive force on a second negatively charged electron. As the polarization cloud is retarded to the movement of the electron, the electron moves $\sim v_F 2\pi/\omega_D \sim 10^8 m/s \cdot 10^{-13} s \sim 100$ nm by the time the maximum ion displacement is reached. Here, we used the Fermi velocity v_F and the Debye frequency ω_D. Over this length scale Coulomb repulsion is screened, allowing the net interaction to be attractive [126].

In a quantum mechanical picture, this can be understood as an exchange of virtual photons by the lattice and the electrons [126, 127]. Under momentum conservation, the exchange of a virtual phonon with lattice vector $\mathbf{q}$ creates two new electron wavevectors $\mathbf{k_1'} = \mathbf{k_1} + \mathbf{q}$ and $\mathbf{k_2'} = \mathbf{k_2} - \mathbf{q}$. The window of phonon frequency that result in an attractive force between the electrons is only possible in a narrow energy window cut of by the Debye energy $\hbar\omega_D$ [127]. As such the phonon-electron exchange is limited to a narrow energy window $E_F + \hbar\omega_D$, given that all states up to the Fermi energy E_F are filled. Therefore, phonon mediated processes have a maximal probability for $\mathbf{k_1} = -\mathbf{k_2}$, i.e. for electrons with opposite momentum. By Pauli's exclusion principle the electron wavefunction must be anti-symmetric under exchange of electrons. The wavevectors $\mathbf{k_1} = -\mathbf{k_2}$ describe a symmetric orbital wavefunction, as such the spin-wavefuntion of the electron has to be an anti-symmetric spin singlet state $|S\rangle = \frac{1}{\sqrt{(2)}}(|\uparrow\downarrow\rangle - |\downarrow\uparrow\rangle)$. This is the description of conventional s-wave superconductivity. We note that there are also more exoctic superconductors predicted with an anti-symmetric orbital wavefuntion and therefore a symmetric spin wavefuntion. This is referred to as p-wave superconductivity, and has been observed in ^{3}He [126, 138]. For our work only s-wave superconductivity is relevant and the Cooper pairs can be described by the notation $(\mathbf{k}\uparrow, -\mathbf{k}\downarrow)$. The Cooper pairs are maximally spin-entangled with a total spin $S = 0$.

The BCS theory now extends on Cooper's work on a single Cooper pair and allows all electrons in the Fermi sea to form Cooper pairs with $(\mathbf{k}\uparrow, -\mathbf{k}\downarrow)$ in a correlated way. This reduces the energy of the system compared to the standard Fermi sea and continues until forming further Cooper pairs does no longer lower the energy. This new ground state is referred to as *BCS ground state*. A theoretical description of this ground state can be found in Ref. [136], while we will focus on the most important results. Unlike the fermionic fermi sea, Cooper pairs obey bosonic statistics. As a result they can be described by a coherent macroscopic wave functions. Furthermore, the excitation spectrum of a superconductor exhibits a gap of 2Δ around the Fermi energy E_F, with Δ the *the superconducting energy gap*. Therefore, an energy of 2Δ is required to break a Cooper pair into two electrons. As these coherent excitation strongly differ from the free electrons excitations of the Fermi gas, they are referred to as *quasiparticles* or *Bogoliubons*. They exhibit a partial electron and hole character. Their dispersion relation is

$$E(\mathbf{k}) = \sqrt{\epsilon(\mathbf{k})^2 + \Delta^2}, \tag{2.41}$$

where $\epsilon(\mathbf{k}) = \hbar^2 k^2/2m - E_F$ is the kinetic energy of a single free electron with respect to the Fermi energy [126]. The dispersion relation exhibits both electron-like ($\epsilon > 0$) and hole-like ($\epsilon < 0$) character, as illustrated in Fig. 2.10(a). For kinetic energies much larger (smaller) than the superconducting gap $\epsilon \gg \Delta$ ($\epsilon \ll \Delta$), the quasiparticles behave like free electrons (free holes) (black dashed lines). At smaller kinetic energies the dispersion relation deviates strongly from free electrons, due to the superconducting gap Δ. No states are lost in the phase transition from the normal to the superconducting state, i.e. $D_N(\epsilon)d\epsilon = D_S(E)dE$. Therefore the quasiparticle density of states (DOS) $D_S(E)$ can be derived as

$$D_S(E) = D_N(\epsilon)\frac{d\epsilon}{dE} = \begin{cases} \frac{|E|}{\sqrt{E^2-\Delta^2}}, & (|E| > \Delta) \\ 0, & (|E| < \Delta) \end{cases} \tag{2.42}$$

Here, we assume the normal state DOS, $D_N(\epsilon)$, to be constant for energies close to the Fermi energy E_F, and therefore $D_N(\epsilon) \approx D_N(0)$ [126]. We plot the normalized DOS in Fig. 2.10(b). We recover the normal DOS for $|E| \gg \Delta$. For $|E| \to \Delta$ the quasiparticle DOS diverges. For energies below $|E| < \Delta$ no quaisparticle states exist and the only states are in the Cooper pair condensate at the Fermi energy E_F.

As has been discussed at the very beginning fo this chapter, superconductors are strongly temperature dependent. Above a critical temperature T_C, they behave exactly like a normal conductor. Therefore, also the superconducting gap Δ is affected by temperature. The gap reduces with incresing temperature until it vanishes at the critical temperatrue T_C. Similarly, quasiparticle excitations increase and the number of Cooper pairs diminish until none are left once T_C is reached. The temperature dependence of Δ is [80, 139]

$$\Delta(T) \approx \Delta_0 \left(1 - \frac{T}{T_C}\right)^{1/2}, \tag{2.43}$$

where $\Delta_0 \approx 1.764\, kT_C$ [126] is the gap at $T = 0$. Hence, temperature can be used to tune a device between the superconducting and normal state. However, due to temperatures strong influence on other device parameters, such as the tunnel rates of QD, it is often not desired to increase the temperature.

Another way to tune of superconductivity is given by their strong magnetic field behavior. The above mentioned Meissner-Ochsenfeld effect or perfect diamagnetism can be explained by the BSC condensate. In a supercondcutor, electrical current is carried by the common motion of Copper-pairs with total center of mass momentum **K** and the ground state and its energy excitation spectrum are not affected by the current flow [126]. Therefore, scattering effects, which would increase electrical resistance, are suppressed by the superconducting gap Δ, as excitations need to be excited above an energy of 2Δ. If the energy associated with supercurrent and the collective center of mass momentum **K** of the Cooper pairs reaches or exceeds 2Δ, Cooper pairs will break up and the superconductor transitions into the normal state. Therefore, if the induced supercurrents expelling the external magnetic field from the superconductor reach this *critical supercurrent*, the superconductor is driven into the normal state. This field is referred to as the *critical field* B_C. Given the often low critical fields of many superconductors and a often weaker effect on many devices of magnetic field compared to temperature, it is often advantageous to make use of the critical field B_C to drive a superconductor into the normal state.

An additional important parameter of a superconductor is the BCS *coherence length* [127]

$$\xi_0 = \frac{\hbar v_F}{\pi\Delta}. \tag{2.44}$$

An intuitive explanation can be given by the spatial extent of a Cooper pair $\delta \sim \hbar/\delta p \sim \hbar p_F/m\delta E \sim \hbar v_F/\Delta$, which uses Heisenberg's Uncertainty relation given an energy uncertainty $\sim \Delta$. Usually, the coherence length ξ_0 ranges from a few nanometers to a few hundred nanometers, which is similar to the above estimation of the retarded ion lattice deformation. As such, the Cooper pairs have a large spatial overlap in the condensate.

2.3.2. Transport in superconductor - normal metal structures

Coupling a superconductor (S) to a normal metal (N) leads to a plethora of interesting effects, as the current in S is carried by Cooper-pairs, while free electrons are responsible for transport in N. We will discuss the most relevant phenomena occuring in N-S devices, which can be expanded to the N-QD-S devices studied in this work.

Andreev reflection and proximity effect

Assuming a completely transparent N-S interface and an electron impinging from N at a subgap energy $|E| < \Delta$, then transport across the interface is blocked, because there are no quasiparticle states below the gap. However, the electron can also not be reflected back into N (Fig. 2.11(a), as normal reflection inverts the momentum. Therefore, a momentum transfer of $\sim 2p_F$ would be necessary. However, for a completely transparent interface, S with its barrier Δ is only able to transfer a momentum of $\delta p = \Delta/v_F$, which is orders of magnitudes smaller than the required energy $2p_F$ [140]. The solution to this problem is given by the so-called *Andreev reflection* (AR) [141], as shown in Fig. 2.11(b). The electron with energy E and momentum $|\mathbf{k}, \uparrow\rangle$ upon impinging on the interface to S, forms a Cooper pair with another electron with energy $-$E and momentum $|-\mathbf{k}, \downarrow\rangle$ while retro-reflecting a positively charged hole. The retro-reflected hole has the same momentum as the incoming electron but

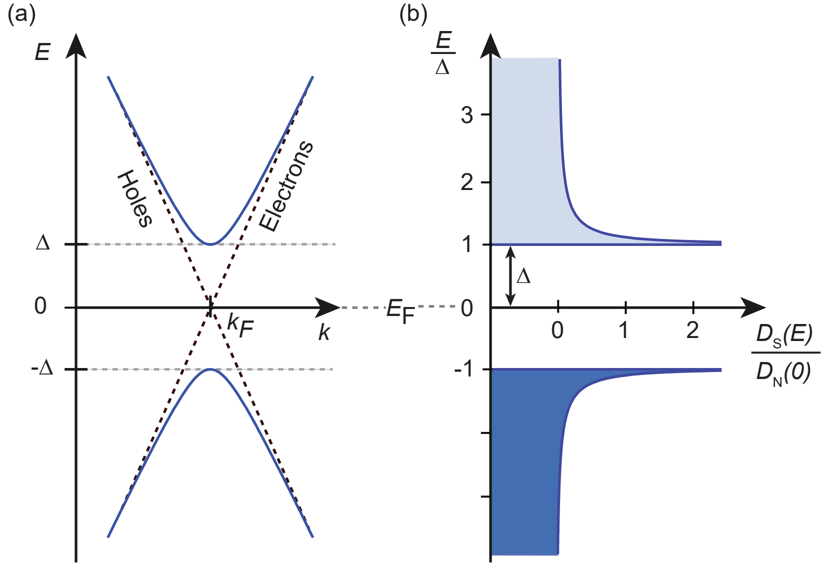

Figure 2.10. Dispersion relation density of states. (a) Dispersion relation of the quaisparticles in a superconductor (blue lines) and normal conductor (black dashed lines). The quaisparticle dispersion relation is gaped by 2Δ. (b) Normalized quasiparticle density of states (DOS) $D_S(E)/(D_N(0)$. Adapted from Refs. [78, 80, 101].

opposite velocity. Thus, a charge of $2e$ is transferred through the interface while momentum is conserved. The charge transfer of $2e$ results in a doubling of the conductance for energies $|E| < \Delta$ compared to the normal state with ideally transparent interfaces.

Transport across an N-S interface for arbitrary transparencies can be described by the BTK model [142]. Hereby, a delta potential $V(x) = Z\hbar v_F \delta(x)$ with the dimensionless barrier strength Z account for elastic scattering due to interface effects such as oxides or band gap misalignment. The transmission coefficient t in the normal state relates to Z with $t = \frac{1}{1+Z^2}$. As already mentioned for a perfect interface $Z = 0$ only AR are allowed and the subgap conductance is twice the normal state conductance $G_S = 2G_N$.

Unfortunately, there are no perfect interfaces in real life due to Fermi velocity mismatch and therefore $Z > 0$. As Z increases, normal reflections become increasingly probable. As seen in Fig. 2.11(c) with $Z = 1$ the subgap conductance becomes reduced and the gap "softens". For large $Z \gg 1$ AR are

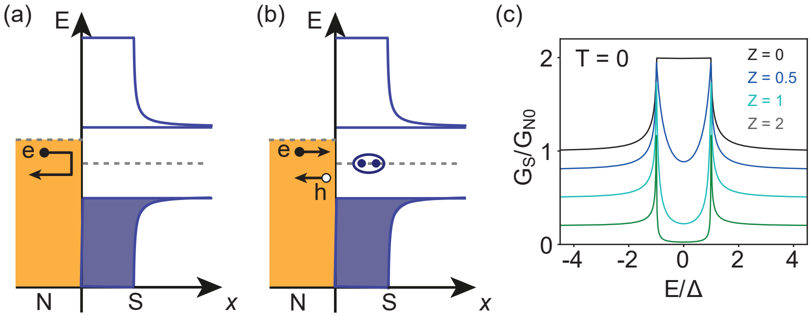

Figure 2.11. Andreev reflection at the N-S interface. Schematic of normal reflection (a) and Andreev reflection (b) for an electron incident from the normal conductor at the S interface. (c) Normalized differential conductance G_S/G_{N0} at the N-S interface according to the BTK-model at $T = 0$ and G_{N0} the differential conductance in the normal state for an ideally transparent interface $Z = 0$. Adapted from [78, 100, 101].

strongly suppressed below the superconducting gap $|E| < \Delta$ and the conductance is reflective of the quasiparticle DOS in S for $|E| > \Delta$. This is generally referred to as a "hard gap" and is corresponding to a tunneling spectroscopy experiment in a N-insulator-S junction.

For a complete picture the time-reversed process also has to be considered. Here, an incident hole is retro-reflected as an electron while removing a Cooper pair from the condensate. As the incident hole and retro-reflected electron keep phase coherence in N for a limited time and distance, there is a non-zero probability to find a Cooper pair in N. Thus, rather than sharply dropping to zero at the interface, the Cooper pair density decays continuously on the length scale of the BCS coherence length ξ in N. This is the so-called *proximity effect* [143]. Thanks to the phase coherence of AR into N, the Cooper pairs "leak" into normal metals in electrical contact with a superconductor. Furthermore, the inverse proximity effect can also happen. Hereby, electrons and holes can enter the superconductor on the lengths scale of the coherence length. This will decrease the density of Cooper pairs at the normal metal superconductor interface.

2.3.3. Crossed Andreev reflection and Andreev bound states

In the following section we will give a very brief summary of crossed Andreev reflections and Andreev bound states. They will not be discussed in detail in the experimental part of this thesis and are added for completeness only. For

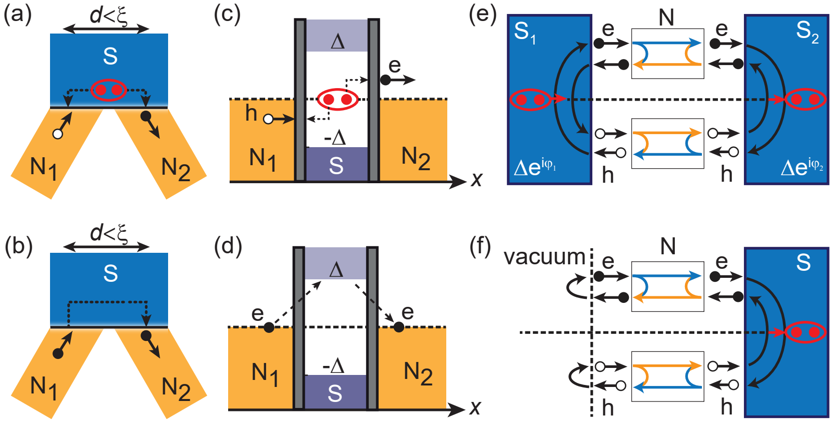

Figure 2.12. Crossed Andreeev reflection and Andreeev bound states. Schematics of crossed Andreev reflection (a) and elastic co-tunneling via virtual quasiparticles states (b). (c), (d) Energy diagrams corresponding to (a) and (b), respectively. (d) Illustration of Andreev bound state formation in an S-N-S junction due to virtual Andreev reflection of electrons and holes. (f) Andreev bound state formation in a N-S device. Adapted from Refs. [78, 80, 101].

a more in depth description, please refer to Refs. [78, 80, 130, 144, 145]

So far, we have neglected the spatial extend $\sim \xi$ of the Cooper pairs along the interface. Hence, an incident electron (or hole) can also be retro-reflected as a hole (or electron) at a distance $d < \xi$ away. For multi-terminal devices, such as two normal metal contacts N coupled to a superconductor S (illustrated in Figs. 2.12(a) and (c)) this can create cross-conductances. This non-local Andreev reflection is referred to as *crossed Andreev reflection* (CAR) [142]. An incident hole from N_1 gets reflected as an electron in N_2. This corresponds to the splitting of a Cooper pair into the normal leads N_1 and N_2. While this is an interesting process to seperate spin-entangled photons, its detection is masked by *elastic co-tunneling*. Analogous to co-tunneling in QDs, an incoming electron can move between N_1 and N_2 through a virtual quasiparticle state in S, as is illustrated in Figs. 2.12(b) and (d)

Let us now consider an S-N-S system, where N has a spatial dimension smaller than the phase coherence length and only a few channels are contributing to transport. In such a system an electron, which is moving from the left to the right lead at an energy $|E| < \Delta$, is Andreev reflected at the N-S interface into a left-moving hole, while creating a Cooper pair in the right lead (S_2). The left moving hole will also be Andreev reflected on the left N-S interface into a right-moving electron while removing two electrons from the left lead (S_1). Hence, a charge of 2e is transferred from the left to the right lead [145].

This system can be described by a scattering matrix formalism [132], which predicts the existence of a discrete set of resonances $E(\phi_2 - \phi_1)$ at energies below the superconducting gap $|E| < \Delta$ and depending on the phase difference $\delta = \phi_2 - \phi_1$ of the two superconductors. These energy state are referred to as *Andreev bound states* (ABS) [145] and schematically illustrated in Fig. 2.12(e). ABS are the mechanism, which carries the supercurrent in mesoscopic structures [132]. This process is often referred to as the *Josephson effect*. In a simple single channel system with transmission T, the ABS energies are $E_{\pm}(\delta) = \pm\Delta\sqrt{1 - T\sin^2\frac{\delta}{2}}$ [145]. Furthermore, ABS can also be formed in N-S junction with only a single superconductor by reflections at the N-vacuum interface, as is illustrated in Fig. 2.12(f).

2.3.4. Superconducting Islands

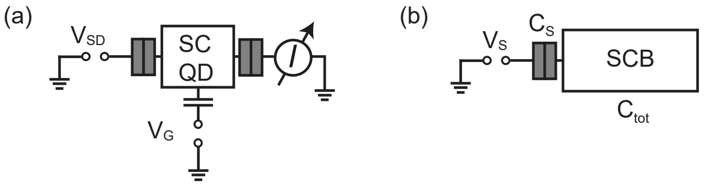

Figure 2.13. Electronic schematic of a superconducting island. (a) Schematic of a proximitized QD tunnel coupled to a source and drain contacts with bias voltage V_{SD} and a capactively coupled plunger gate V_G. (b) Scheme of a superconducting charge box (SCB) tunnel coupled only to one lead with voltage V_S and capacitance C_S and total capacitance C_{tot}.

So far, we have only considered QDs and superconductivity independently. Now, we will consider a system they interplay: a superconducting quantum dots or island. Such a system can be engineered by either proximitzing a semiconducting QD with a superconductor, as illustrated in Fig. 2.13(a) or by tunnel coupling a piece of a superconductor to create a superconducting charge box (SCB) (Fig. 2.13(b)) or a single Cooper pair transistor.

Let us consider a simple S-N tunnel junction, which is biased by voltage V_S, similar to the device illustrated in Fig. 2.13(b). If the tunnel resistance R_t to the SCB is large enough, such that $R_t \gg h/e^2$, then the total charge n on the island is a good quantum number [77, 146, 147]. If the voltage V_S is increased, more electron will accumulate on the SCB in order to minimize the total energy of the circuit. The ground energy of the SCB is then given by [146]

$$E_n = E_c(n - C_S V_S/e)^2 + \mathcal{E}_n, \tag{2.45}$$

where $E_C = e^2/2C_{tot}$ is the energy needed to add one extra electron to the SCB, and $\mathcal{E}_n$ is the non-electrostatic energy part of the SCB. Note, that E_C here differs by a factor of 1/2 from the charging energy we defined for single QDs, as the charging energy gives the difference in electrochemical potential needed to add an extra electron. For a normal charge box $\mathcal{E}_n = 0$, and for a superconducting charge box $\mathcal{E}_n = D_0 p_n$, where D_0 describes the energy difference between odd and even ground states and $p_n = n \bmod 2$. According to the BCS theory $D_0 = \Delta$, where Δ is the superconducting gap of the SCB [146].

The total energy of such a SCB is plotted in Figs. 2.14(a)-(c) as a function of the polarization $C_S V_S/e$ of the island for a number n of several excess electrons residing on the SCB. The odd electron occupations are colored in red and the even ones in blue. For $\Delta = 0$ there is no difference between even and odd occupation. Electron transport on the island can happen whenever the ground state energy of different occupation numbers are degenerate, $E(n) = E(n+1)$. As there there is no difference between the even and odd populated ground state energies, the equilibrium number $\bar{n}$ of electrons at zero temperature exhibits a regular staircase function (Fig. 2.14(d)) and the Coulomb blockade resonances are evenly spaced with a peak distance of $1e/\alpha$ (Fig. 2.14(g)), where α is the lever arm on the island .

At $\Delta < E_C$ the odd states have energy levels, which are higher in energy than the even states (Fig. 2.14(b)). Therefore the even and odd ground state energies are degenerate at different $C_S V_S/e$ and the even steps in $\bar{n}$ are longer than the odd steps in $\bar{n}$ (Fig. 2.14(e)). Consequently, there is also an even-odd spacing of the Coulomb blockade peaks in transport (Fig. 2.14(h)).

Once $\Delta > E_C$ the odd states are so much higher in energy that the even states are always the ground state of the system (Fig. 2.14(c)) and transport is mediated by Andreev reflections at the junction. This results in the SCB only being loaded by Cooper pairs. Consequently, the even steps in the equilibrium number of electrons vanish completely (Fig. 2.14(f)) and transport happens in regular spaced Coulomb blockade resonances with a spacing of $2e/\alpha$ [147].

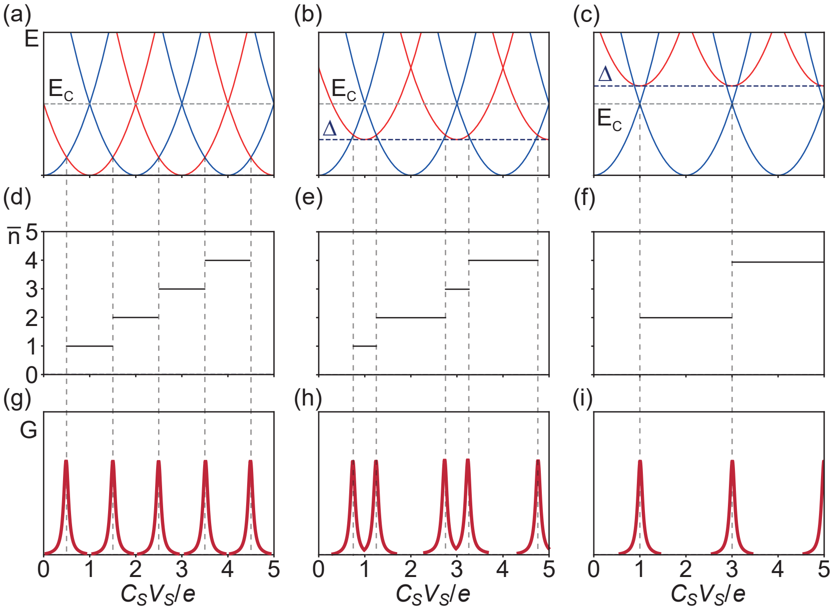

Figure 2.14. Energy and conductance of a superconducting island. Total energy on the island as a function of the polarization C_SV_s/e for several excess electrons n on the island for $\Delta = 0$ (a), $\Delta < E_C$ (b), and $\Delta > E_C$. (d)-(f) Equilibrium number of electrons $\bar{n}$ on the island corresponding to (a), (b), and (c). (g)-(i) Resulting conductance peaks at zero bias corresponding to (a), (b), and (c). An 1e spacing is observed for $\Delta = 0$ (g), an even-odd spacing for $\Delta < E_C$ (h), and a 2e-spacing for $\Delta > E_C$.

3 Experimental Methods

This chapter will focus on the fabrication of the devices discussed in this thesis. The most important fabrication steps are introduced. Exact recipes can be found in Appendix A. Additionally, the low-temperature setups both for low and high-frequency measurements are shown.

3.1. Fabrication

Before any measurements can be conducted a working sample has to be fabricated. For this thesis we worked exclusively with zincblende (ZB) InAs nanowires (NW) with built-in wurtzite (WZ) tunnel barriers. More information about the growth, properties, and characterization of these NWs can be found in chapter 4. To begin, we will introduce the base structure fabrication used for low-frequency measurements, then the resonator fabrication for radio-frequency measurements. We will follow with a brief description of the different ways of NW deposition on the base structures and resonator samples. Then, the cleaning of these samples and contacting procedure for the deposited NWs will be discussed. We use standard fabrication techniques, such as electron-beam lithography (EBL), metallization of the NWs with thermal and e-beam evaporation, as well as standard wet and dry etch methods. This standard techniques will not be discussed in here, more information about them can be found in Refs. [148–150]. We will finish this by briefly discussing the bonding to a chip-carrier or a printed circuit board (PCB). The detailed fabrication recipes can be found in Appendix A.

Base structure for low-frequency measurements

Before depositing the NW a *base structure* has to be fabricated first. The base structure, which consists of large bond pads connected to smaller device pads, as well as a marker grid, allows to locate and align the NWs with high-precision and to connect the NW electrically to the larger measurement setup. We use a highly p-doped silicon (Si) wafer as a substrate. The silicon also acts as a global backgate (BG) and is insulated from the devices by a 400 nm thick thermally grown layer of silicon oxide (SiO_2). In a first step the wafer is cut into 2 cm x 2 cm large pieces. The size is given by the sample space in our

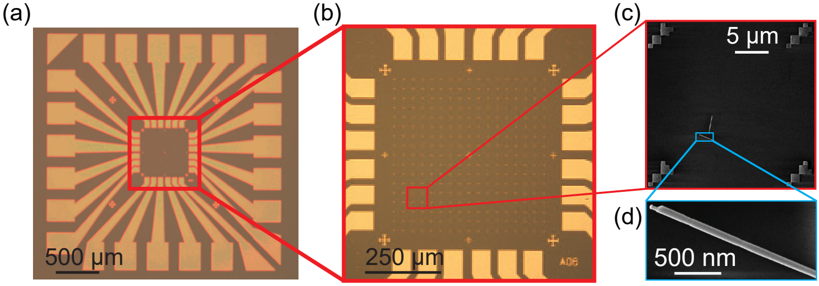

Figure 3.1. Base structure. Optical microscope images of a base structure (a) used for low-frequency measurement and the marker space (b) for NW deposition and alignment. Scanning electron microscope (SEM) image of one marker square with NWs deposited (c) and of a single NW (d). Adapted from refs. [100, 101].

e-Beam writer. The substrate surface is then cleaned first by ultrasonication in acetone and then in isopropanol (IPA) 20 minutes each. The substrate is then blow dried by either compressed air or compressed nitrogen (N2) gas.

The base structure is then fabricated by conventional EBL, and e-Beam evaporation of 5 nm/45 nm titanium/gold (Ti/Au), followed by a lift-off in acetone at 50°C. The resulting base structures consist of a 2 mm by 2 mm area, which contains bonding pads connected to contact leads pads and alignment markers, as is shown in Fig. 3.1(a). The inner part of the base structure, shown in Fig. 3.1(b), contains a 500 μm by 500 μm grid of fine alignment markers, each with an unique shape to allow exact identification of the position. The distance between adjacent markers is 20 μm. A square of four of such markers is shown in an SEM image in Fig. 3.1(c).

Resonators for radio-frequency measurements

The resonators in this thesis were fabricated by J. H. Ungerer and D. Sarmah. For completeness sake we will give a short summary of their fabrication, more detail can be found in the theses of J. H. Ungerer [151] or R. Haller [152].

An ultra-high quality niobium titanium nitrite (NbTiN) film is sputtered on a undoped Si substrate. For best resonator quality the film is directly sputtered on bare Si after an hydrofluoric acid etch step to remove the native SiO_2. Such a film is used for the sample discussed in chapter 7. For an optimization of device-integration with the resonator the film is sputtered on 100 nm of SiO_2. The device discussed in chapter 8 uses such a film.

After sputtering the etch mask for the resonator structure is written with

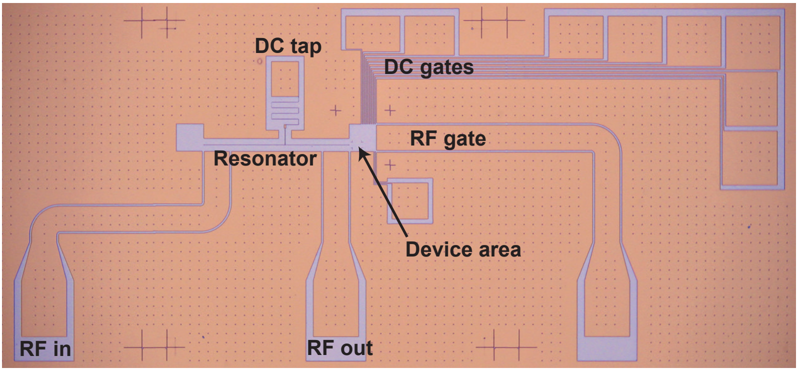

Figure 3.2. Transmission resonator. Optical microscope image of a finished transmission type high-impedance resonator before NW deposition. Picture by D. Sarmah.

standard EBL. The devices used in this work employ high-impedance resonators to increase the coupling strength to the NWs. Our resonators are designed for resonance frequencies of ∼ 3.5 GHz (chapter 7) and ∼ 5.3 GHz (chapter 8). The films have a sheet kinetic inductance of $Ł_{sq} \approx 90$ pH and we make use of narrow center conductors of about 300 nm to 400 nm width to achieve a high impedance of 2.1 kΩ. After EBL, the exposed film regions are dry-etched using a Ar/Cl_2 gas in a reactive ion etching plasma machine. After etching the etch mask is lifted-off in acetone at 50°C. For the resonator fabricated on bare Si a 20 nm hafnium oxide (HfO_2) layer is grown only on the NW deposition region. Accurate 5 nm/45 nm Ti/Au markers for NW alignment are fabricated using standard EBL and e-Beam evaporation either after or before NW deposition. An example of a finished transmission type resonator can be seen in Fig. 3.2.

Nanowire deposition

After completion of the base structures or resonators the NWs are deposited from the growth substrate to the prepatterned device substrate. Two different methods for NW deposition are used due to the different sizes of the deposition areas. For the base structures, which have a 500 μm by 500 μm marker space, the tip of a sharply cut cleanroom tissue is used. The tissue is cut into a small triangle with a sharp tip. By carefully and lightly touching the growth chip surface the NWs are transferred to the tissue. Now, the same tissue is gently touched on the base structure center and some of the NWs will be transferred from the tissue to the substrate. The deposition of the NWs is checked in the optical microscope. The last two step of the procedure are repeated until the desired NW density is reached. After deposition the chip is cleaned in acetone and IPA and blow dried by compressed air or N2. No ultrasonication should be used after deposition of the NWs, as it can move or remove NWs from the substrate.

For the resonator structures the NW area of is too small for the tissue method. Instead the NWs are transferred using a micromanipulator. A glass needle with a pointed end is controlled by a very accurate hydraulic system, allowing accurate placement of the NWs. The needle is first brought into contact with the growth substrate, where NWs stick to the tip of the needle due to van der Waals forces between the needle and the NW. The needle can then be moved to the resonator structure and be brought in contact with the NW area. Some of the NW are removed from the needle and transferred to the substrate by the contact. Again, this procedure is repeated until the desired density of NWs is reached.

After NW deposition and alignment marker fabrication, the NWs are imaged in a SEM. The NWs used in this work posses a GaSb-shell selectively grown on the ZB segments of the NW. This allows us to easily identify the tunnel barriers present in the NWs during imaging. More information about the NWs in particular is found in chapter 4. The GaSb-shell is used to identify the NWs best suited for the experiment and to find the barrier positions, which are measured from the top of the NW. Using images such as the one shown in Fig. 3.1(c) the NW positions are read-out using a Python program written by O. Faist. Using the information of the position of the NW and its barriers the electrical contacts and gates are designed separately for each NW using Elphy.

GaSb-shell removal

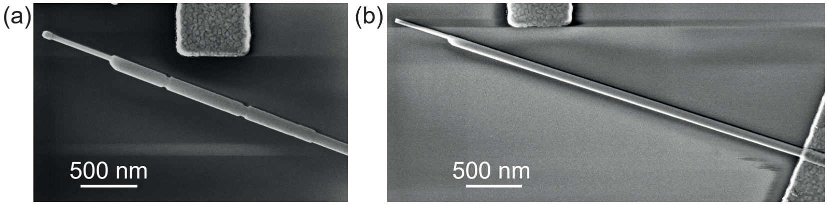

Figure 3.3. GaSb-shell etching. SEM picture of the same NW before (a) and after (b) the GaSb-shell etching. On the bottom right of (b) the metallic clam is visible.

After identifying the position of the wurtzite tunnel barriers using the selectively grown GaSb-shell, the shell serves no purpose anymore and has to be removed before contacting. To do so we first ‘clamp’ the NW by EBL writing and evaporating 5 nm/85 nm Ti/Au on the bottom of the NW, where it wont interfere with the contacts or gates. The clamp serves to hold the NW in place during the wet-etching, its exact form is not important. After lift-off a 1 min 30 W oxygen (O_2) plasma is performed to clean of e-beam resist residues. The GaSb-shell is then etched for 3 minutes 30 seconds in Microposit$^{\mathrm{TM}}$ MF-319 Developer (Tetramethylammoniumhydroxid (TMAH) concentration between 2.14% and 2.5%) under constant movement and afterwards thoroughly rinsed in de-ionized water. Alternatively, an etch window can be opened with standard EBL, while the bottom of the NW is clamped with resist. Note, that we did not observe any differences in etching while varying the time from 3 to 4 minutes, so it is not a very time sensitive process. However, the etchant needs to be fairly fresh. For etchants open longer than six months (irrespective of expiration date) incomplete etching of the GaSb-shell as well etching of the InAs NW was observed. In Fig. 3.3 the same NW is shown, once before etching (a) and one after the etching (b). Parts of the metallic clamp are also visible on the bottom right of Fig. 3.3(b).

Nanowire metallization

After removal of the GaSb-shell the NWs are ready for contacting. The contacts are patterned by standard EBL using a 300 nm thick PMMA resist layer. To clean potential resist residues a 1 min O_2 plasma cleaning at 30 W is performed. The samples are then mounted in an e-Beam or thermal evaporator with built-in ion gun, which mechanically removes material by bombarding it with ions. In order to achieve electrical contact between the metal and the NW, a 2-3 nm thick native oxide layer surrounding the NW has to be removed. We use the in-situ Argon (Ar) milling using the ion gun, to remove the oxide. Once the native oxide is removed, the desired metals can be evaporated, if necessary the sample stage of the evaporator can be cooled with liquid nitrogen. Afterwards, the resist is lifted-off in 50°C acetone. To fabricate top gate (TG) electrodes the removal of the native oxide is skipped, so that it can act as an insulating layer between the gate and the NW. For side gate (SG) fabrication the native oxide does not need to be removed either, but it can be advantageous to evaporate them together with the contacts to decrease the number of fabrication steps.

Furthermore, we have developed a technique to evaporate thin homogeneous Al films on top of NWs. As the film is much thinner than the NW, disconnected Al pads are left in close proximity to the NW, which can be contacted to be used as gate electrodes. Further information can be found in chapter 6.

Bonding of low-frequency samples

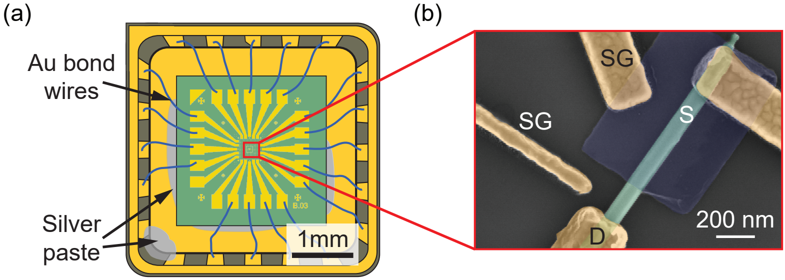

Figure 3.4. Chip carrier with bonded sample. (a) Schematic of a typical sample after bonding. The sample is glued into the chip carrier with conductive silver paste, which also connects the BG. The contacts pads are bonded to the chip carrier with gold wire. b) False-colored SEM image of a finished device with a Ti/Au contact (yellow), a normal SG (yellow), an Al break-off SG (yellow and blue pad) and a thin Al contact (blue) on top of the NW.

To finish the fabrication and measure the device the sample substrate is glued with conductive silver paste to a commercially available non-magnetic chip-carrier. This is schematically shown in Fig. 3.4(a). With the silver paste electrical contact is created between the back of the highly p-doped Si substrate and the chip carrier. This allows to use the Si as a global BG. To connect the gates and contacts standard wire bonding techniques are used to bond the bond pads to the chip carrier via gold wire. It is important that the bonder is properly grounded, as improper grounding can lead to electrostatic discharge (ESD) and explode the NWs. After successful bonding, the chip carrier can be build into the cryogenic measurement setup. If the samples need to be stored before measurements, they are stored in vacuum to avoid degradation of the contacts. However, the samples are not very sensitive to air and can be kept at ambient pressure for a while if needed.

Bonding of high-frequency samples

The bonding of the high-frequency samples is similar to the low-frequency ones. We will note the important differences here. Unlike the commercial chip carriers, we use a PCB designed by L. Y. Cheung. It is modular, allowing to include a bias tee for adding high-frequency and DC signals to the same device

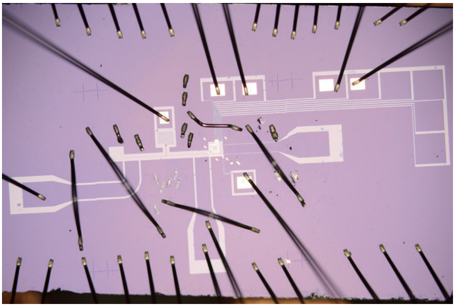

Figure 3.5. Bonded resonator device. Microscope image of a bonded resonator device. The ground plane has to be carefully grounded with plenty of bond wires.

contact. The sample is glued into the PCB with PMMA and baked at 100 °C for 1 minute.

During bonding careful attention has to be paid to properly bond the ground plane of the sample to the ground of the PCB. Due to the high impedance ground plane a single bond is insufficient and as many bond wires as possible should be connected. Furthermore, bond wires should be used to connect parts of the ground plane, which are separated by the resonator structure. Not doing so can lead to spurious resonance modes and lower internal quality factors. Figure 3.5 shows a microscope image of such a bonded resonator device

3.2. Low-frequency measurement setup

It is crucial to have low sub-Kelvin electron temperatures to measure quantum mechanical phenomena. For the QDs measured in this work, the charging energy ranges from a few hundred μeV up to tens of meV. To resolve this QDs the thermal energy must be significantly lower than the charging energy and the single particle level spacing δE. Additionally, to couple superconductor to these devices the electron temperature needs to be lower than the critical temperature and the superconducting gap Δ. We mainly use aluminium as a superconductor with a gap of $\Delta \approx 240$ μeV and a critical temperature of 1.2 K [153, 154]. With commercially available dilution fridges in our laboratory we reach base temperatures below 50 mK, corresponding to an energy of ~ 4 μeV.

Inserting a sample into liquid ^{4}He can rapidly cool it down to 4.2 K. Further cooling can be achieved by pumping on the surface of liquid ^{4}He, as latent heat

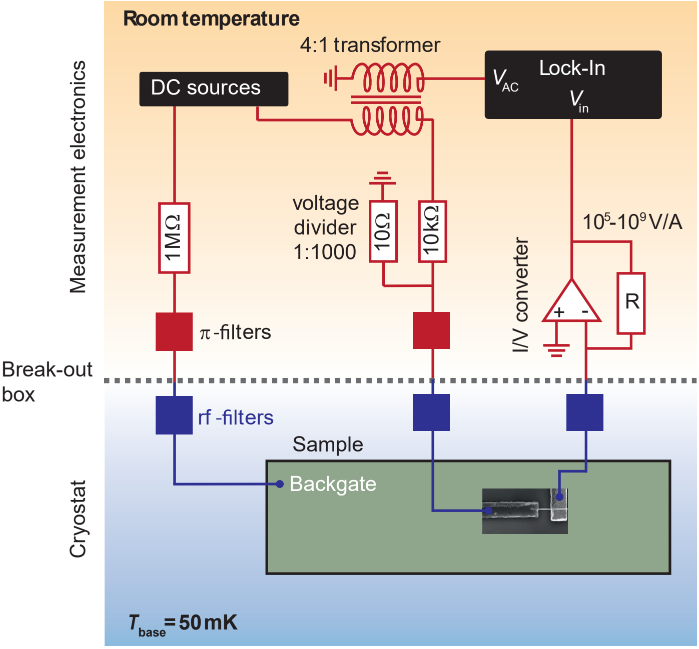
Room temperature
Measurement electronics
4:1 transformer
DC sources
Lock-In
V_{AC}
V_{in}
voltage divider 1:1000
1MΩ
10Ω
10kΩ
10^5-10^9 V/A
I/V converter
R
+
-
π-filters
Break-out box
rf-filters
Sample
Backgate
Cryostat
T_{base} = 50 mK

Figure 3.6. Schematic of low-frequency measurement setup. Standard measurement setup of a voltage biased differential conductance measurement of a NW at low temperature in a dilutrion refrigerator with a base temperature of 50 mK. Adapted from Refs. [78, 79, 100, 101, 144, 150].

is removed by evaporation from the bath. With this method a temperature of 1.2 K can be reached. In order to reach temperatures significantly below this a dilution refrigerator is needed. A mixture of ^{3}He and ^{4}He spontaneously separates into a light ^{3}He-rich and a heavy ^{3}He-poor phase below $\sim$ 870 mK [138, 155]. An osmotic pressure difference is created by pumping the mixture. This drives ^{3}He from the ^{3}He-rich phase into the ^{3}He-poor. Through the dilution of ^{3}He into ^{4}He across the phase boundary the mixing chamber gets cooled [138]. Using this principle base temperatures below 10 mK can be achieved. The cryostats can be equipped with a superconducting magnet, which enables magnetic field studies up to several teslas.

We mount the chip carrier to the cryostat with a commercially available chip socket. The sample and the chip socket are shielded by a Faraday cage. After mounting the inner vacuum chamber (IVC) its volume with the sample is pumped down to very low pressures. To connect our measurement instruments at room temperature we use a home-made breakout box with BNC connectors and grounding switches. The connection to the breakout box is made by twisted-pair lines. The measurement lines are equipped with several filters to filter out high-frequency noise and minimize the electron temperature. We employ a home-built tapeworm filter is mounted on the cold-finger [78, 101, 144, 149, 156]. Its cut-off frequency is 10 MHz. Additional 1 MHz filters are built into the break out box. In general, we observe an electron temperature below 100 mK [100].

We use standard low-frequency lock-in techniques to measure differential conductance. Figure 3.6 shows a basic schematic of the measurement setup for a two-terminal measurement. An AC bias is applied to the source (S) contact with a SR830 lock-in amplifier. A DC voltage supplied by a Yokogawa YK7651 or an in-house low noise high resolution 8 channel digital-to-analog converter (DAC) by Basel Precision Instruments (BPI). We use a 4:1 transformer to superimpose the AC voltage on the DC voltage. Directly on the breakout box a 1:1000 voltage divider is used to reduce the voltage further. Additional DC voltages for gates are supplied by the DAC from BPI. For voltages higher than 10 V a voltage amplifier also by BPI was used. The resulting current from the device is amplified by a low-noise I-V converter from BPI and the output voltage is measured by the lock-in, giving us the differential conductance $G = dI/dV$. The measurement instruments were controlled by QCodes [157], which is a python based data acquisition program framework. Further lab and setup specific code was programmed by Joost Ridderbos and other users in the group.

3.3. Radio-frequency measurement setup

After mounting and bonding the sample onto the PCB, the PCB is closed by a Faraday cage. After connecting the RF and DC connectors the PCB is mounted into an Oxford Triton dilution refrigerator using a bottom loader. The general cooling procedure using a mixture of ^{3}He and ^{4}He is the same as described above for low-frequency measurements, however here we use a cryogen-free dilution refrigerator. It replaces the necessary liquid He bath with a cryocooler.

The measurement setup is schematically shown in Fig. 3.7. The low-frequency instruments and setup are similar as described previously. DC voltages are sourced by a DAC by BPI and filtered by a in-house built low-pass filter at room temperature. Additionally, the DC lines are filtered at the mixing chamber by QDevil low-pass filters. As described above for low-frequency measurements standard lock-in technique is used for measuring differential conductance. To measure currents a Keithley voltage meter is used instead of a lock-in.

For the RF measurements a coherent microwave signal is generated by a vector network analyzer (VNA) from Rohde & Schwarz. At every temperature stage the microwave signal is attenuated, so that the average photon number in the resonator is less than one [158]. We show an example of a transmission resonator coupled to a DQD in Fig. 3.7, as we will use in chapter 8. Two QuinStar isolators with a cut-off frequency of 8 GHz decouple the outcoming microwave signal from the noise of a high electron mobility transistor (HEMT) from Low Noise Factory at the 4 K stage. At room temperature the signal is additionally amplified by two HEMT amplifiers and then measured by the VNA. To perform magnetic field measurements, the system is fitted with a 3-axis superconducting vector magnet at the 4 K stage.

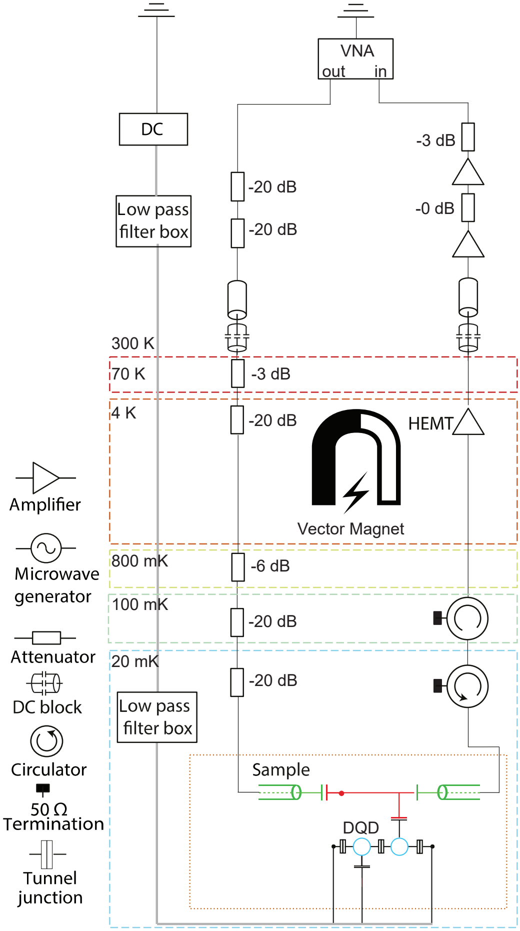
VNA
out
in
DC
Low pass filter box
-20 dB
-20 dB
-3 dB
-0 dB
300 K
70 K
-3 dB
4 K
-20 dB
HEMT
Amplifier
Vector Magnet
Microwave generator
800 mK
-6 dB
100 mK
-20 dB
Attenuator
20 mK
-20 dB
DC block
Low pass filter box
Circulator
Sample
50 Ω Termination
DQD
Tunnel junction

Figure 3.7. Radio-frequency measurement setup At room temperature vector network analyzer (VNA) generates a coherent microwave signal. It is attenuated in the dilution refrigerator. After the resonator it is amplified at cryogenic temperatures by a high electron mobility transistor (HEMT) amplifier and at room temperature by two additional HEMT amplifiers. The microwave signal is then measured in the VNA. Adapted from J. Ungerer [151]

4 Material Platform

This work is based on semiconducting indium arsenide (InAs) nanowire (NWs). We will study InAs NWs in particular, but semiconducting NWs can also be grown from group IV materials (Ge, Si), other III-V compounds (InAs, GaAs, GaP, InP) and II-VI compounds (ZnSe, CdSe) as high purity single crystals [159]. They are pseudo one-dimentionsal nanotstructures with a diameter of a few to tens of nanometers and lengths up to tens of micrometers.

Semiconducting InAs NWs provide an ideal platform for a variety of physical experiments. They offer a low effective mass[160], a small electronic band gap [161], a high mobility [162] (add more zincblende specific), a tunable large Landé g-factor [96, 163–165], and a large spin-orbit interaction [76, 166, 167]. The combination of these properties allows for all electrical control of the electron spin [96, 168, 169], making them a promising candidate for spin qubits [167, 170] and spintronics [171, 172] in general. The large spin-orbit interaction also makes them interesting candidates for the study of topological phenomena, such as Majorana fermions [16, 44, 45, 173, 174], which could enable topological quantum computing [15, 175]. They have further found use in studies of magnetotransport [176, 176–178] and thermoelectrics [179].

In addition to all the general properties of InAs NWs listed above, the NWs used in this work contain in-built, atomically sharp crystal-phase defined tunnel barriers [40]. This allows us to investigate robust single tunnel barriers and QDs without the need of defining the barriers by gating. This approach delivers advantages both in possible scaling of devices, as well as a general understanding of a particular device and the physical location of our measured properties.

In the following we will give a brief introduction into the growth of these NWs. For a more detailed explanation refer to ref. [180]. Afterwards we will give a short introduction to the general electronic properties of InAs. Subsequently, we will show some characterization measurements done on the NWs used in this work.

4.1. Nanowire Growth

For decades free-standing NWs have been grown using vapor-liquid-solid methods [181]. The name originates from the growth of a solid one-dimensional

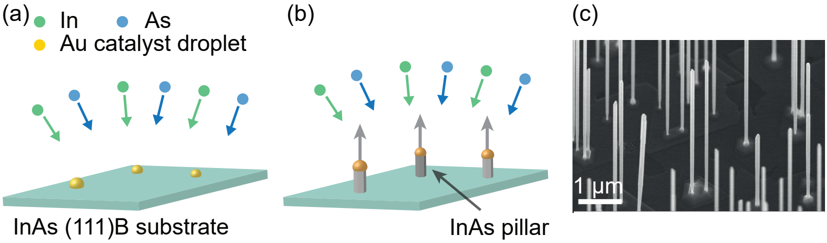

Figure 4.1. Schematic of InAs NW growth. (a) Indium (In, green) and arsenic (As, blue) precursors are accumulating in the liquid gold (Au, yellow) catalysts on an InAs (111)B substrate). (b) The catalysts are saturated and the vertical growth of the NW starts. The catalyst stays on top. (c) Scanning electron image (SEM) image of a free-standing NW "forest", grown with MOVPE. Image provided by S. Lehmann, Lund. Adapted from Refs. [100, 101, 150]

crystal using a vapour-phase precursor, mediated by a liquid alloying material [180, 182, 183]. Examples of growth techniques making use of this method are molecular beam epitaxy (MBE) [28, 183, 184], chemical vapor deposition (CVD) [185], chemical beam epitaxy (CBE) [37, 38, 186], and metal-organic vapor phase epitaxy (MOVPE) [40, 41, 183, 187].

The basic principles of VLS based processes is the accumulation of metal-organic or atomic precursors inside a liquid metallic catalyst (or seed) particle (Fig. 4.1(a)) from a precursor gas. Typically, the catalyst is made of gold, as it has great alloying capabilities and is inert to oxygen. Once the liquid droplet is saturated with the precursor, a crystalline nanowire starts to grow vertically with the metallic catalyst staying on the top of the NW due to surface tension [182]. The radial growth is limited by the catalyst dimensions, as illustrated in Fig 4.1(b). Once the NWs reach the desired length, the growth process is halted by removing the precursors. There are various methods to deposit the catalyst particles, such as direct deposition [188], metal evaporation and subsequent annealing [189], aerosol techniques [190], or metallic arrays defined by electron beam lithography and subsequent metallic evaporation [191]. This latter growth process allows for precise control of the growth parameters. The growth rate can be controlled by the flux of the precursor gas and the length of the NW by the growth time. The diameter of the NW can be controlled by the size of the gold catalyst. It is also possible to lower the growth temperature, so that the vertical growth is suppressed and radial growth is enabled [180].

In the case of InAs the bulk crystal is in zincblende (ZB) crystal-phase, but it is possible to grow both crystalline defect free wurzite (WZ) [192] and zincblende NWs [36, 40, 180] using the right growth parameters and advanced

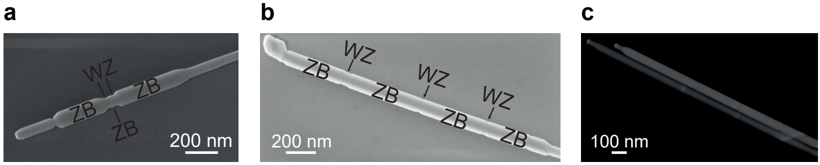

Figure 4.2. SEM images of NWs. SEM image of a ZB InAs NW with a crystal-phase defined small single QD (a) and a long DQD (b). Both have a selectively epitaxially grown GaSb-shell only on the ZB. (c) Scanning trasmission microscope image of such a DQD NW as shown in (b), before growing the GaSb-shell. On the bottom is a schematic of the each NW. The WZ segments are colored in red, ZB segments in green, the GaSb-shell in blue, and the gold particle in gold. Image (c) provided by S. Lehmann, Lund.

growth techniques. It is even possible to switch with atomic precision between ZB and WZ crystal-phase to define a heterostructure within the NW [36, 39, 40]. The NWs used in this work are grown by the group of Kimberly A. Dick-Thelander at Lund University [35, 40]. These NWs are grown in ZB crystal-phase interrupted by short WZ segments of a few tens of nanometers. The used NWs were grown by MOVPE with gold particles as catalyst. The gold particles were distributed onto a $[\bar{1}\bar{1}\bar{1}]$-oriened III-IV substrate by an aerosol technique. The NWs were grown at a temperature of 415 °C with trimethylgallium, trimethylindium, phospone and arsine as precursor gses. The switching between ZB and WZ segments is controlled by tuning only the group V precursor flow [40]. Due to the conduction band offset between ZB and WZ [39, 60, 161], the WZ segments form tunnel barriers for electrons of about ~ 100 meV height. By switching between WZ and ZB single tunnel barriers and QDs can be formed. The precise control of the growth parameters allows for great flexibility in both QD and barrier length. We will later characteristic both single tunnel barriers, single QDs and DQDs. In contrast to earlier experiments [60, 61, 144], the ZB segments have a selectively grown GaSb-shell [35]. This allows us to easily identify the tunnel barrier position by SEM imaging, as the crystal-phase change between ZB and WZ is not easily resolved in a standard SEM. In order not to complicate the transport properties of the NW and QDs the GaSb-shell is etched before contacting, for further information on the etching procedure consult chapter 3 and Appendix A.

For completeness we would like to note, that there are also techniques to grow template-directed NWs and free-standing NWs without seed particle, such as selective area growth [26, 28, 193, 194] and template-assisted growth [27, 41, 42, 187]. These template-direted growths have the advantage of a more scalable approach and can be readily incorporated in existing device structures. However, they are limited in resolution by the method used to define the template and are confined to their growth substrate, giving less flexibility of use [180]. But as lithography method keep increasing in precision and resolution and a less flexible but scalable approach would be preferable for qunatum computing, they might be a very interesting platform for the future. However, this work will focus on the above described ZB InAs NW with crystal-phase defined tunnel barriers.

4.2. Electronic Properties

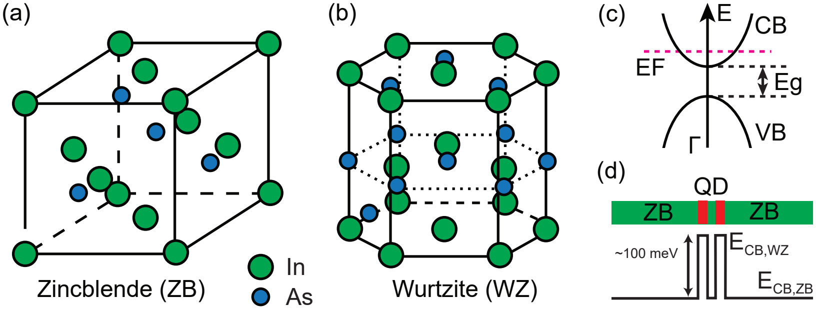

Figure 4.3. Crystal structure and band structure of InAs. Crystal structure of face-centered cubic (fcc) zincblende (ZB) (a) and hexagonal close-packed (hcp) wurtzite (WZ) (b) InAs. (c) Schematic of the electronic band structure of InAs with band gap $E_g = 420$ meV (ZB) [195]. The Fermi energy E_F is pinned to the conduction band in InAs NWs. (d) Schematic of the QD confinement due to the ~ 100 meV difference in conduction band offset of ZB and WZ. Adapted from Refs. [100, 176, 196]

This work makes use of ZB InAs NWs with built-in crystal-phase defined WZ tunnel barriers. ZB InAs has a face-centered cubic lattice structure, as illustrated in Fig. 4.3(a). In contrast, WZ InAs has a hexagonal close-packed crystal structure, seen in Fig. 4.3(b). To define the tunnel barriers we make use of the difference in band gap E_g and the misalignment of the conduction band between ZB and WZ, as is illustrated in Fig. 4.3(d). The band gap of ZB is $E_{ZB} = 0.42$ eV [195], while the bandgap of WZ has been theoretically predicted to be larger [197] up to 126 meV [198] and a lower bound of the bandgap difference of ~ 95 meV has been measured in similar NWs [39]. Additional advantages of InAs NWs are the Fermi level pinning to the surface, allowing for easy to fabricate, low-ohmic contacts [199], as well as the large Landé g-factor $g = -14.9$ [195] and the large spin-orbit interaction [76]. A mean free path of ~ 100 nm has been shown in InAs NWs [200]

Around the Γ point the conduction band has a parabolic dispersion $E_n(k_x) = E_n + \frac{h^2 k_x^2}{2m^*}$ (Fig. 4.3(c)) with an effective electron mass $m^* = 0.023 m_e$ in ZB crystal phase [201], where m_e describes the free electron mass and E_n the mimimum energy of a quantized subband. As new subbands get occupied the current $I = \frac{2e^2}{h} N$ shows step-wise increases in the ballistic quantized conductance with N the number of occupied subbands [202].

In conclusion, InAs NWs serve as an interesting platform for a variety of experiments and applications. They exhibit a large variety of growth possibilities (heterostructures, epitaxial interfaces to metals and other semiconductors), and interesting electronic properities such as large spin-orbit coupling and g-factors. In addition they are easy to contact thanks to the Fermi level pinning in the conduction band. Thus they present an ideal platform for us to study different physical phenomena. We will explore their coupling to superconducting contacts, as would be of interest for topological states such as Majorana fermions [16, 44], and as a platform for charge and spin qubit defined in DQDs.

4.3. Characterization of InAs nanowires

We now characterize the different types of NWs used in this work. We exclusively use zincblende InAs NWs with wurtzite crystal-phase segments actings as tunnel barriers as introduced above. The growth batches vary in length of zincblende segments, number of tunnel barrier, while the width of the wurtzite tunnel barriers is constant around ~ 30 m. In chapters 5 and 6 we use NWs with two tunnel barriers to define either long (~ 300 nm to ~ 1 μm) or short (a few nm) QDs. With the long QDs we also take advantage of their length to put a contact on the QD segment and fabricate three-terminal devices. With those we to study a single tunnel barrier. All of these devices were fabricated with one superconducting (SC) and one or two normal (N) metal contacts. This chapter only discusses the general characterization of the NWs and barriers. The studies of the superconducting properties are reported in chapters 5 and 6. Furthermore, we study DQDs with three tunnel barriers in chapter 7 and 8.

We note, that due the growth method with precursor distribution by aerosol technique every growth chip shows a spread in the NWs with segments lengths around the desired parameters. This is in general an advantage for us, as it allows us to use the same growth chips for different experimental applications by selecting the NWs with the optimal parameters. However, it would also be possible to grow a chip composed of identical NWs using a method of precursor distribution that is more uniform, such as e-beam lithography.

In the following, we first characterize single tunnel barriers, followed by

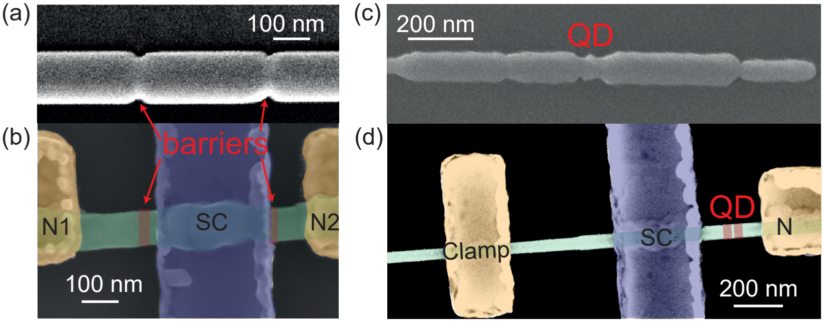

Figure 4.4. Tunnel barrier and single quantum dot devices. SEM images of two of the NWs used for the single tunnel barrier measurements (a), and single QD measurements (c) in this chapter. False-colored SEM image of one of the complete device measured for the single tunnel measurements (b) and a similar complete device as is used for the QD measurements (d). The NW is colored in green, the tunnel barriers in orange, the normal Ti/Au contacts in yellow, and the superconductor in blue.

short and long single QDs. At the end of this chapter discuss the first basic characteristics of a DQD.

4.3.1. Single tunnel barrier

The NWs are electrically contacted as described in chapter 3. To study the properties of a single tunnel barrier, we use NWs with QDs of a length of ∼ 300 nm. Figure 4.4(a) shows an SEM image of such a NW on which we performed the measurements discussed in this section on. We will refer to it as NW$_A$. We fabricate three-terminal devices, where one superconducting (SC) contact is evaporated between the barriers and two normal metals (N1, N2) contacts at the end of the NW. Figure 4.4(b) shows a false-colored SEM image of device A fabricated with NW$_A$. The two SEM images have been manually rescaled and aligned, such that the estimated barrier position after fabrication and the original NW SEM image are aligned.

The superconducting properties and three-terminal measurements of device A will be discussed in detail in chapter 5. For this chapter we will restrict our discussion to only the N1-barrier-SC junction. For device A the source-drain bias voltage V_{SD} was applied on SC and the differential current I on both N1 and N2 was measured. We estimate a distance between the tunnel barrier and the SC of about $d_{SC} \sim 20$ nm from SEM images before and after etching of the GaSb-shell. In Fig. 4.5 we compare the differential conductance

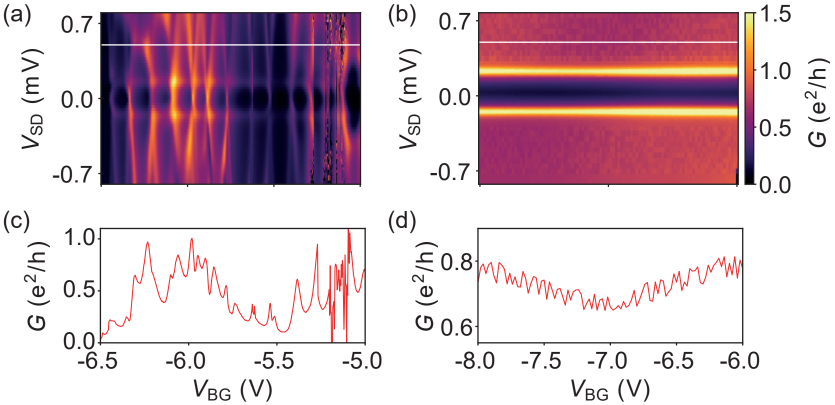

Figure 4.5. Quantum dot features vs clean barrier. Differential conductance $G = dI/dV$ for a tunnel barrier junction of length $d_{SC} \sim 85$ nm ((a), device B) and $d_{SC} \sim 20$ nm ((b), device A). The longer junction exhibits features of a QD. The short junction a clean tunnel barrier. (c), (d) traces from (a), (b) at $V_{SD} = 0.5$ mV (white line).

$G = dI/dV$ plotted as a function of V_{SD} and BG voltage V_{BG} of device A and device B. The latter was fabricated from NWs of the same growth and with the same contact configuration. However, the distance between the tunnel barrier and the SC contact is larger, namely about $d_{SC} \sim 85$ nm. Data of device B is shown in Fig. 4.5(a) and of device A in Fig. 4.5(a). We find fairly little change in the normal state conductance, as is illustrated in the cross section at $V_{SD} = 0.5$ mV in Fig. 4.5(d). In contrast, device B shows a clear signature of a QD strongly coupled to the leads. We explain this by the formation of a spurious QD between the tunnel barrier and the SC contact. To illustrate this further Fig. 4.5(c) shows a cross section from the conductance measurement of device B taken at $V_{SD} = 0.5$ mV as well. In comparison to device A the conductance is less constant and shows oscillations typical for Coulomb blockade resonances at high source-drain bias. In contrast we note, that device A shows characteristics consistent with a clean tunnel barrier with from +7 V to −38 V. Unfortunately, the device did not survive more negative voltages. On the whole range for device A we see small fluctuation in conductance and less conductance at more negative V_{BG} as the charge carriers in the NWs get more and more depleted. We never observe any clear discrete states as we see for device B.

We have observed a general trend of more clean barriers for shorter distances between SC and barrier. In devices where the SC overlaps the barrier no QDs have been observed and the devices always show a clean albeit very weak barrier. The distance between the N contact and the barrier seems to have less influence on the cleanliness of the tunnel barrier For examples we can see a clean barrier in device A, despite a distance of $d_{N1} \sim 160$ nm between N1 and the barrier. From this we conclude that we likely form QDs between the tunnel barrier and the SC, which we can suppress by bringing the SC contact closer to the barrier than $d_{SC} \sim 80$ nm. Alternatively, if the barrier is close enough, the SC might contact screen the gate voltage and confined states could not be discriminated in spectroscopy. A possible explanation to the difference in sensitivity to the length of the N-barrier junction to the SC-barrier junction, could be that a normal contact has a lesser screening effect. This, however does not readily explain why we still observe a clean gap at finite magnetic fields, where the SC contact also turns normal conducting.

To confirm that we indeed perform tunnel spectroscopy on the superconducting gap we apply an out-of-plane magnetic field B_Z. The conductance as a function of B_Z and V_{SD} at $V_{BG} = -6$ V is shown in Fig. 4.6(a). A closing of the superconducting gap is observed around 25 mT. This agrees well with previously observed critical fields of Al in our lab of 10 mT to 100 mT and literature values [153, 154]. Furthermore, the inset in Fig. 4.6(b) shows two line cross sections of Fig. 4.6(a) at a $B_Z = 0$ mT (red) and $B_Z = 50$ mT (blue). Without superconductivity we observe a constant conductance independent of source-drain bias, as is characteristic for a clean tunnel barrier.

To study the influence of the tunnel barriers, we compare the conductance for two NW segments with and without built-in tunnel barriers. As is seen in Fig. 4.4(b) in the device A a barrier is present between N1 and SC, while the one between N2 and SC is shorted by SC. In Fig. 4.6(b) the back gate voltage dependence of the conductance measured on SC in the gap at $V_{SD} = 0$ is shown, where V_{SD} is applied on N1 of device A. A clear dependence on V_{BG} is shown with the conductance decreasing more than two orders of magnitude from above 3 G to near depletion. The same data plotted in log scale can be found in Appendix B.1. In comparison the gate dependence (see Appendix B.1) of the SC-N2 junction is much weaker and the overall conductance is much higher. Hence, we conclude that there is indeed the tunnel barrier over which most of the voltage drops occurs, compared to the contacts or possible impurities in the NW. Without tunnel barrier we observe conductances up to nearly 25 e^2/h, showing that our contacts are of good quality and that the NWs have many-modes contributing to transport.

4.3.2. Single quantum dot

Here, the device is contacted on one side with a normal Ti/Au contact and on the other side with a superconductor (SC) Ti/Al. Between the two contacts is a crystal-phase defined double barrier QD as shown in Fig. 4.4(d). In Fig. 4.7

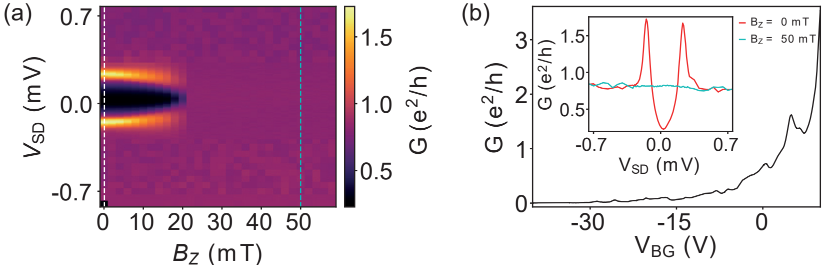

Figure 4.6. Magnetic field and gate dependence. (a) Differential conductance $G = dI/dV$ in dependence of source-drain bias V_{SD} and magnetic field B_Z at a constant backgate $V_{BG} = -6$ V. The superconducting gap closes at around ~ 25 mT. (b) Backgate dependence of the conductance in the gap at $V_{SD} = 0$. Inset: Cross sections of (a) at 0 (red) and 50 mT (blue).

we show Coulomb blockade diamonds of a single QD as a function of the global back gate voltage V_{BG}. The small SC gap is hardly visible at low V_{BG}, as has been previously observed in similar NWs [60, 144].

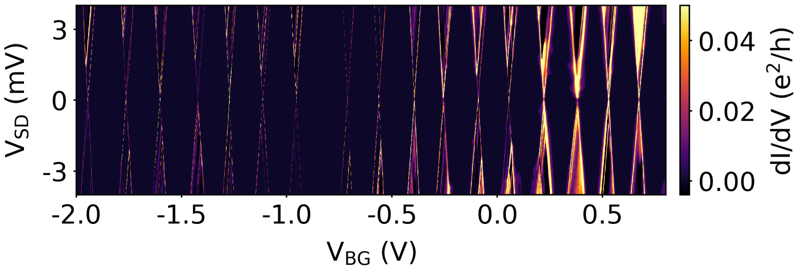

Figure 4.7. Single quantum dot. Coulomb blockade diamond measurement of a single QD as a function of the backgate voltage V_{BG} and V_{SD}.

We extract a lever arm of $\alpha \approx 0.07$ at low V_{BG}, a charging energy $E_C \approx 11.2$ meV, and a single level spacing $\delta E \approx 1.2$ meV. In Appendix B.2 α and the addition energy E_{add} is plotted as a function of V_{BG} for a range of $V_{BG} = -2$ V to $V_{BG} = +2$ V. A general decrease of the E_{add} and α is observed. This is commonly observed in QDs at higher electron fillings, as Coulomb screening increases the more electrons are accumulated on the QD [77, 100].

The tunnel coupling of the QD is tunable by the BG voltage, as is illustrated in Fig. 4.8(a). The total tunnel coupling $\Gamma = \Gamma_1 + \Gamma_2$, where $\Gamma_{1,2}$ are the tunnel

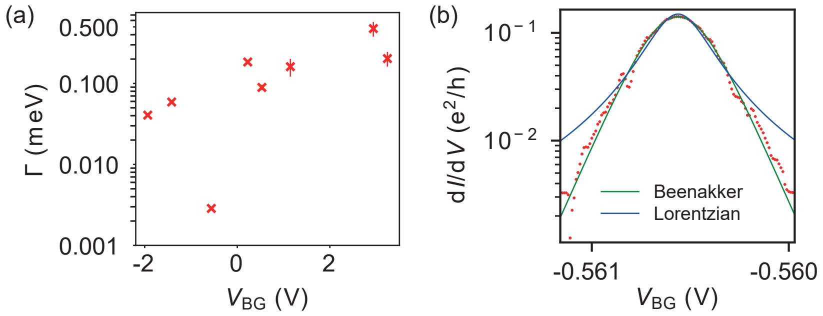

Figure 4.8. Gate dependence of Γ. (a) Extracted tunnel coupling Γ of several of the Coulomb peaks in Fig. 4.7 in dependence of V_{BG}. (b) Only Coulomb peak with $\Gamma < 10$ μeV. The blue and green line are a lift-time broadened (Lorentzian) and thermally broadened (Beenakker) fit to the data, illustrating that the resonance is thermally broadened.

couplings to lead 1 or 2 respectively, is extracted by numerically fitting eqs. 2.4 and 2.5 to the Coulomb bockade resonances and taking $\Gamma_{1,2}$ from the better fit. To remove effects from the SC contacts the resonances were measured at an out-of-plane field $B_Z = 50$ mT. We observe a tunability of Γ over three orders of magnitudes, although most tunnel couplings are above 40 μeV and only one resonance is thermally broadened. It might be possible to observe even a larger range of Γ by measuring at more positive V_{BG}. In similar NWs with crystal-phase defined QDs Γs from 50 μeV up to above 1 meV have been observed and extracted by numerically fitting [60].

We show the data and the fit of the single temperature broadened Coulomb resonance in Fig. 4.8(b), it yields a reasonable electron temperature of 92 mK. It is not exactly clear as to why this particular resonance is less tunnel broadened, as there are several broadened resonances at even lower BG voltages. Possibly, at these particular voltages the transport modes are decoupled. However, the physical reasons of this are unclear.

4.3.3. Double quantum dot

Adding a third barrier to the NW results in a DQD. Figure 4.9(a) shows a false-colored SEM image of such a device. The NW (green) has a DQD defined by three tunnel barriers (red). It is contacted by Ti/Au on both ends and three side gates (SGs) are used to tune the DQD. The central gate V_M is mostly fixed to a constant volt. The device is grounded on one end and connected to a resonator with bias-tap on the other side. In Fig. 4.9(b) we show the

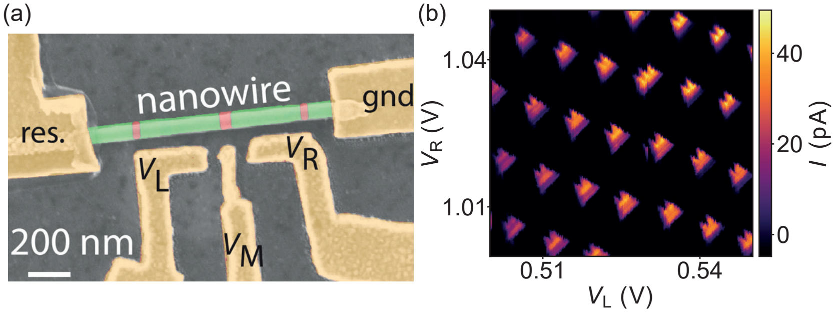

Figure 4.9. Charge stability diagram of a DQD. (a) False-colored SEM image of the device measured. NW (green) with three in-built tunnel barriers (red) defining a DQD. (b) Charge stability diagram measured in dependence of gates V_R and V_L with $V_M = 2$ V. An effective source-drain bias of 100 μV was applied.

measured charge stability diagram measured at a 100 μV bias. We observe textbook bias triangles as described in chapter 2.

From the bias triangles we extract the lever arms and capacitances of our device. Namely, $\alpha_{L,1} = 0.22$ for the left gate on QD1 and $\alpha_{R,2} = 0.14$ for the right gate on QD2, as well as cross-lever arms $\alpha_{L,2} = 0.06$ and $\alpha_{R,1} = 0.03$. The lever arms show that we have a small cross coupling and stronger lever arms for the SGs.

We note, that basically no gate tuning was necessary to observe the charge stability diagram. The DQDs merely has to be gated positively enough, such that a measurable current can be observed. Due to the in-built tunnel barriers the DQD is then observed as soon as a current can be detected and no tedious adjusting of several gates is necessary. However, due to the size of the QDs ($\sim$ 300 nm each) the DQD cannot be depleted to the last electrons due to the NW charge carriers depleting beforehand. Therefore, the exact electron number on the DQD is unknown and the charge parity of the DQD cannot be easily determined.

The inter-dot tunnel rate can be tuned by filling the DQD. In chapter 7 we extract inter-dot tunnel rates in a range from 45 μeV to 0.36 meV. The device could be further tuned into the single QD regime, where the inter-dot tunnel barrier is so weak that the electron wavefuntion delocalizes over both QDs and effectively one large QD is observed [77, 81]. Further information can be found in chapter 7.

Furthermore, the device yield is very high. The device shown here was the first DQD device fabricated. Three out of three correctly contacted samples were measured and showed the clear characteristic of a DQD. This high device yield makes these NWs a promising platform for experiments were only a low number of devices can be cooled down at the same time, such as RF-measurements were only one device can be coupled to a resonator. They have also shown themself to be fairly robust to electro static discharge for quasi one-dimensional systems. Presumably, due to their fairly large ($\sim$ 80 nm) diameter.

A more detailed discussion of the device shown here including radio-frequency (RF) measurements can be found in chapter 7 and a second DQD device coupled to a resonator is shown in chapter 8.

4.4. Summary and Outlook

We have shown characterization measurements of single tunnel barriers, single QDs and DQDs. For short distances $d_{SC} < 80$ nm between the SC contact and a tunnel barrier, an ideal barrier characteristic can be observed. For longer distances spurious QDs are formed between the barrier and the SC contact. The length of the NW segment between the N contact and the barrier does not seem to have as much influence.

Magnetic field measurements confirm that the NWs are in good electrical contact to the superconductor and the barriers allow us to perform tunnel-spectroscopy, which shows the BCS coherence peaks at $V_{SD} \approx 150$ μV, and a conductance suppression of a factor $\sim 6 - 15$ at $V_{SD} = 0$. Furthermore, we show that we can tune the in-gap conductivity with the back gate voltage by more than two orders of magnitude if a barrier is present.

We present the Coulomb diamonds of a single QD and extract the tunnel couplings for several resonances. We find tunnel rates Γ from 4 μeV up to 0.5 meV in a back gate voltage range from -2 to 3 V. Most resonances are life time broadened with $\Gamma > 40$ μeV, with the exception of a single temperature broadened resonance with significantly lower Γ. We note, that a larger range of tunnel rates may be observed by a more in-depth study and a greater gate voltage range.

We present a very-regular charge-stability diagram of a DQD. The bias triangles are aligned in the honeycomb pattern allowing us to extract some of the basic characteristics of the DQD. We will later make use of these nice DQDs to couple them to a resonator to form a charge and spin qubit.

In conclusion, we show NWs with built-in tunnel barriers and good contact quality. By adding tunnel barriers in series QDs can be formed. Here, examples of single and double QDs are shown, but it would be possible to extend the growth to triple or more QDs and arrays or even one-dimensional superlattices [203] if desired. Serial QDs, such as DQDs, are an ideal platform for spin and charge qubits. The well-defined DQDs shown here, streamline the fabrication process and create a high device yield. We will further discuss DQDs coupled to resonators to create charge and spin qubits in chapter 7 and chapter 8.

5 Spectroscopy of the superconducting proximity region

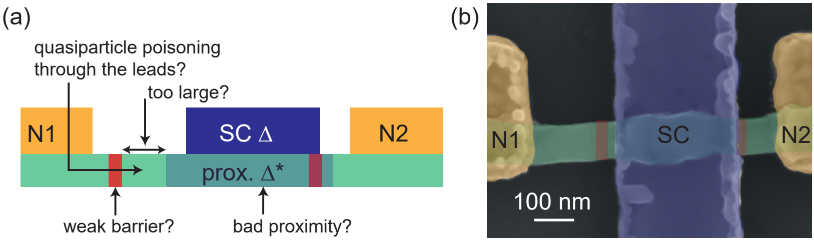

Figure 5.1. Three-terminal device. (a) Schematic of the three-terminal superconductor-NW hybrid device. The texts note some of the possible causes of a soft superconducting gap. (b) False-colored SEM image of the device discussed in this chapter. NW (green) with wurtzite tunnel barriers (orange) contacted on the outside with normal contacts Ti/Au and between the barriers with superconducting Ti/Al.

In this chapter we discuss our results of coupling evaporated superconducting (SC) Al contacts to InAs nanowires. We will make use of the well-defined QDs or tunnel barriers described in chapter 4 to investigate the SC gap induced in the NW. In practice, we study three-terminal devices, as illustrated in Fig. 5.1. The measurements discussed in chapter 4 already demonstrated a "soft" proximity gap. While the distinction between a hard and soft proximity gap is not properly defined, a common used definition is the suppression of the in-gap conductance to the normal out-of gap conductance by a factor of 50 [204, 205]. In contrast, we tend to observe a suppression of about $\sim 8 - 15$ in our devices (see Fig. 4.6a) or Fig. 5.8), clearly demonstrating a much softer SC gap.

In this chapter we will first show that there is a proxmity region and the experiments do not probe indirectly the bulk Al gap. By using three-terminal device structures we can exclude the possibility of tunneling proceses from the normal conducting NW into the SC bulk Al.

In a next step we then discuss possible reasons for the soft superconducting gap, such as a too large distance between the tunnel barrier and the SC, too weak tunnel barriers, quasiparticle poisoning by the lead segments, or a "bad" induced proximity effect in the NW. These possible causes are schematically illustrated in Fig. 5.1(a).

5.1. Three-terminal measurements

5.1.1. The conductance of adjacent contacts

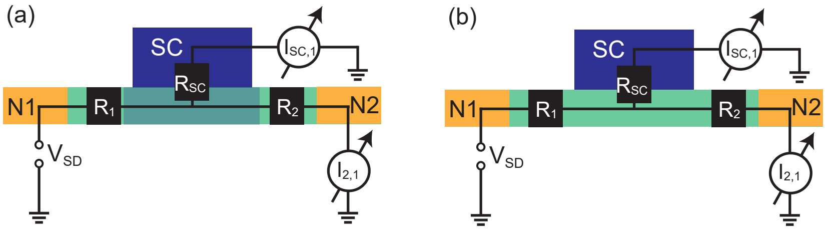

Figure 5.2. Three-terminal device schematic with and without induced SC gap. The NW is illustrated in green, normal contacts N1 and N2 in yellow, and the SC contact in blue. An induced proximity region is depicted by a light blue region in (a) and missing in (b). The tunnel barriers and contact resistances have been replaced by resistances R_1, R_2, and R_{SC}, where $R_1 \gg R_2, R_{SC}$ due to the tunnel barrier included in R_1. V_{SD} is applied on the normal contact N1 and the current $I_{SC,1}$ and $I_{2,1}$ are measured on SC and N2 respectively.

To prove that we indeed perform spectroscopy on an induced SC region below SC and not on the bulk SC reservoir, we perform three-terminal measurements, as is illustrated in Fig. 5.2. The goal is to discriminate two different explanations for our measurements, the case in Fig. 5.2(a) with an induced gap (light blue area) and the case in Fig. 5.2(b) without. If we assume no proximity region, we only expect a N-S interface at the interface to the SC contact. The interfaces to N1 and N2 would be normal. If we assume a proximity region below SC, there is an N-S interface from both N1 and N2 to the proximity region.

We assume a simplified model, where tunnel barrier, contact and NW resistance are combined into one resistance $R_{1,2,SC}$ for each junction of the three-terminal device. Here, $R_1 \gg R_2, R_{SC}$ as the NW segment between N1 and SC is the only junction with a built-in tunnel barrier. The following measurements were performed in all possible three-terminal configurations, where the bias voltage V_{SD} is applied on one of the three contacts and the current on the other two is measured using standard lock-in measurements. We will denote $G_{j,k} = \frac{dI_j}{dV_k} = \frac{I_j^{(ac)}}{V_k^{(ac)}}$ as the conductance measured on contact j with V_{SD} applied on contact k, an example for these schemes and notation can be found in Fig. 5.2. For the case where the SC induces a proximity gap the

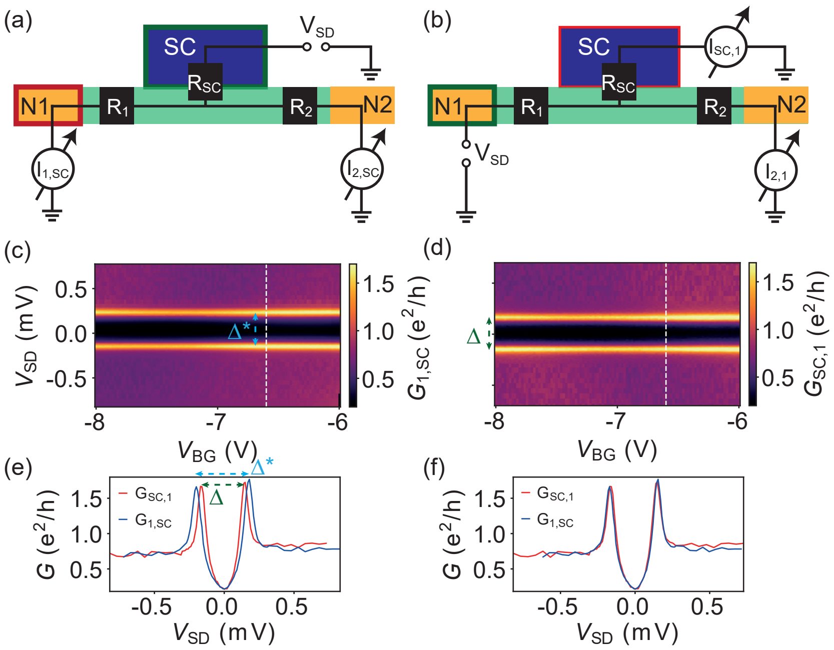

Figure 5.3. Conductance on the left NW side. Comparison of differential conductance $G_{1,SC} = dI_1/dV_{SC}$ in configuration (a) where V_{SD} is applied on SC and $I_{1,SC}$ is measured on N1 and (b) conductance $G_{SC,1} = dI_{SC}/dV_1$ where V_{SD} is applied on N1 and $I_{SC,1}$ is measured on SC. (c), (d) Differential conductance as a function of V_{SD} and V_{BG} in configurations (a) and (b), respectively. e) Differential conductance in dependence of V_{SD} taken at $V_{BG} = -6.6$ V (dashed white line in (c) and (d)) for the configuration in (a) (blue) and (b) (red), only offsets in V_{SD} were subtracted and V_{SD} of $G_{1,SC}$ was reversed. Two different proximity gaps are observed, Δ and Δ^*. (f) Same measurement as in (e), but the data was additionally corrected for the applied V_{SD} accounting the voltage division resulting form the resistances $R_{1,2,SC}$.

resistances $R_{1,2}$ have the character of an N-S interface and therefore a V_{SD} dependent characteristic as described by the BTK-model [136]. In the case, in which SC does not induce a proximity gap only the resistance R_{SC} is described by an N-S interface, while $R_{1,2}$ are normal, V_{SD} independent resistors. For the adjacent contact measurement, which always involve SC, we will assume that R_1 and R_2 are constant without any V_{SD} dependence that a proximity region would entail. In this section we model our data using intuitive electronic elements, such as voltage and current dividers based on the respective lumped circuit elements defined above.

We study the difference between $G_{SC,1}$ and $G_{1,SC}$ (see Fig. 5.3(a) and (b)). For these measurements $I_{2,1}$ was also measured, and hence the electrostatic potential on N2 is zero. However, $G_{2,1}$ will be discussed in the next section. In these two configurations always the same section of the NW and the same tunnel barrier are probed.

Naively, in a two-terminal measurement, we would expect no difference besides a sign change in V_{SD}, as $+V_{SD}$ applied on N1 is equivalent to applying $-V_{SD}$ on SC, i.e. $G_{SC,1}(V) = G_{1,SC}(-V)$. In the experiment we observe a different picture, due to the existence of the third terminal.

Figure 5.3(c) and (d) show the differential conductance $G_{kj} = dI_k/dV_j$ as a function of V_{SD} and V_{BG} corresponding to the measurement configurations shown in Fig. 5.3(a) and (b), respectively. Both measurements show a clean soft superconducting gap with little modulation in the conductance above the gap, as has been introduced in chapter 3. As we just discussed, the asymmetry of the normal state conductance $G_{SC,1}$ and $G_{1,SC}$ in V_{SD} for $|V_{SD}| > \Delta$, is identical with respect of a change in sign of V_{SD}, i.e. $G_{SC,1}(V) = G_{1,SC}(-V)$ $\forall\, V \in |V_{SD}| > \Delta$.

To better compare this we study the conductance in dependence of V_{SD} at fixed $V_{BG} = -6.6$ V in Figs. 5.3(e) and (f). Both data sets were corrected for a small offset in V_{SD} created by the IV-converter and V_{SD} was reversed for $G_{1,SC}$. While two very similar gaps are observed, the $G_{1,SC}$ exhibits a slightly larger gap. We explain this effect by a simple loaded voltage divider with R_2 as the load resistance. Depending on whether V_{SD} is applied on SC or N1 the input and output resistances switch and due to the very different resistances with $R_1 >> R_2, R_{SC}$ the actual applied V_{SD}^* on R_1 and R_{SC} differs from V_{SD}. Assuming V_{SD} is applied on SC the parallel load on the voltage divider is

$$R_P = R_1 \parallel R_2 = \frac{R_1 R_2}{R_1 + R_2}. \tag{5.1}$$

From our measurements of $G_{1,SC}$ we estimate $R_1 \approx 32$ kΩ from the above gap resistance at $V_{BG} = -6$ V. Using conductance $G_{2,SC}$ for the above gap resistance in the same gate range we estimate $R_2 + R_{SC} \approx 1$ kΩ. Since $R_1 \gg R_2, R_{SC}$ we can assume, that the above-gap measured resistance on N1 when V_{SD} is applied on SC is a good approximation of R_1. However, R_2 and R_{SC} have comparable values and we cannot attribute a fixed ratio. For the calculations we assume that $R_{SC} \approx 140$ Ω and $R_2 \approx 860$ Ω. Taking R_2 as the load resistance we can calculate R_P. We now calculate the voltage V^*_{SD,R_1} dropping over R_1, when V_{SD} is applied to SC

$$V^*_{SD,R_1} = V_{SD}\frac{R_P}{R_{SC}+R_P} \approx 0.86V_{SD} \tag{5.2}$$

and the voltage dropping over R_{SC} is

$$V^*_{SD,R_{SC}} = V_{SD}\left(1-\frac{R_P}{R_{SC}+R_P}\right) \approx 0.14V_{SD} \tag{5.3}$$

In contrast if V_{SD} is applied on N1, R_1 replaces R_{SC}, so that R_P only becomes smaller, in the above equation. Since R_1 is two orders of magnitude larger than the other resistances, the above term of the voltage across R_{SC} approaches zero and nearly all the drops over R_1. The equation for the voltage dropping across R_1 if V_{SD} is applied on N1 becomes

$$V^*_{SD,R_1} = V_{SD}\left(1-\frac{R_P}{R_1+R_P}\right) \approx 0.996V_{SD}, \tag{5.4}$$

with the parallel resistance now defined by $R_P = R_2 \parallel R_{SC}$. This clearly shows that $G_{SC,1}$ is barely affected by the voltage divider. Plotting $G_{SC,1}$ and $G_{1,SC}$ with the correct V^*_{SD,R_1} and $V^*_{SD,R_{SC}}$ gives Fig. 5.3f), which shows almost perfect agreement between the two data sets, showing that we can explain the difference in Δ using a simple voltage divider model with reasonable values for R_1, R_2, and R_{SC}. In turn these results show that the exact values for R_2 and R_{SC} can vary. As long as they have a ratio between 1:4 and 1:8 the extracted Δs are identical within a $\sim 5\%$ error margin. Furthermore, to obtain a SC gap of 160 μeV $\geq |\Delta| \geq$ 150 μeV, R_1 has to be about twice larger than the sum of $R_2 + R_{SC}$. The second condition is easily fulfilled given the above gap resistances extracted from $I_{1,SC}$ and $I_{2,SC}$.

We can perform the same analysis for the other NW side, i.e with V_{SD} applied on SC (or N2) and the current is measured on either N2 (or SC), while N1 is grounded. Since R_1 is now the parallel load resistor and much higher in resistance than the other resistors it does not influence the voltage divider. Using the same analysis as above, we obtain $V^*_{SD,R_S} \approx 0.86V_{SD}$ and $V^*_{SD,R_{SC}} \approx 0.14V_{SD}$ independent of configuration. Figure 5.4 shows the results in conductances analogous to Fig. 5.3 for the right NW side involving contacts SC and N2. The overall conductance between SC and N2 is much higher as expected, as the right tunnel barrier is shorted by the SC contact. This justifies the assumption $R_2, R_{SC} \ll R_1$.

Comparing Fig. 5.4(c) and (d) shows little influence of the measurement configurations in Fig. 5.4(a) and (b) on the differential conductance. This is further confirmed by the Fig. 5.4(e), where the conductances G for both configurations are plotted as a function of V_{SD} at a constant $V_{BG} = -6.6$ V, with the data corrected for small offsets in V_{SD}, and with V_{SD} inverted for

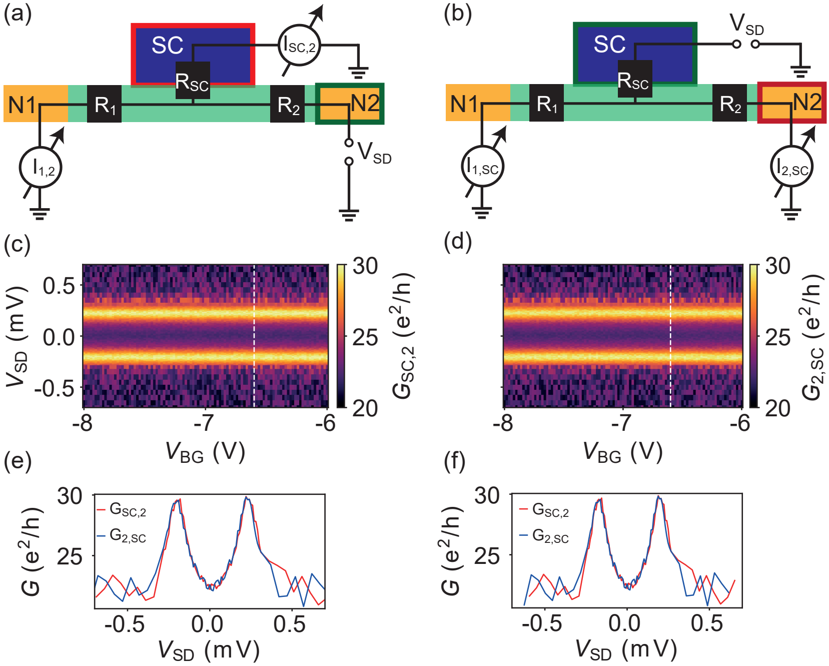

Figure 5.4. Conductance on right NW side. Comparison of differential conductance $G_{2,SC} = dI_2/dV_{SC}$ in configuration (a) where V_{SD} is applied on SC and $I_{2,SC}$ is measured on N2 and (b) $G_{SC,2} = dI_{SC}/dV_2$ where V_{SD} is applied on N2 and $I_{SC,2}$ is measured on SC. (c), (d) Differential conductance as a function of V_{SD} and V_{BG} in configurations a) and (b), respectively. (e) Differential conductance in dependence of V_{SD} taken at $V_{BG} = -6.6$ V (dashed white line in c) and d)) for the configuration in (a) (blue) and (b) (red), only offsets in V_{SD} were subtracted and V_{SD} of G_{SC-N2} was reversed. (f) Same measurement as in e), but the data was additionally corrected for the applied V_{SD} accounting the voltage division resulting form the resistances $R_{1,2,SC}$.

$G_{2,SC}$. The curves show very good agreement. In Fig. 5.4(f) the same data is plotted but now corrected for the voltage division factor of 0.86 described above. As the curves were already nearly identical and the same factor was applied on them, they still are virtually identical. The only effect of the divider was a reduction of the aparent induced superconducting gap from $\Delta^* \approx 200$ μeV to $\Delta^* \approx 170$ μeV. We note that, while both values are within the range of observed of SC gaps for Al [206], the smaller value is much closer to what we commonly find in our devices.

These experiments show the importance of a careful consideration, what voltages are effectively developing at which position in a device and which voltage drops are actually measured. In two-terminal measurements such effects can often not be properly pinpointed as there are too many unknowns about the device and only one way to measure. In contrast, three-terminal measurements allow to measure in additional configuration, as we have shown here. However, the extra contacts also complicate the system, requiring careful consideration and analysis to not reach wrong conclusions due to a faulty understanding of the voltages applied and measured. In our case here, it would have been very easy to conclude that we measure an inhomogeneous induced superconducting gap, of $\Delta^* = 210\ \mu$eV on the rights side and $\Delta^* = 190\ \mu$eV on the left side, even though we can attribute variability to a simple voltage divider picture. Our built-in tunnel barriers and our precise knowledge of their position grant us an additional advantage here, as it makes our device easier to understand.

We note that the above voltage divider analysis was not reliant on assuming a proximity region below the SC. The resistances R_1, R_2, and R_{SC} were assumed to be constant and based on the measured above-gap resistances. The observed SC gap could originate purely from the SC contact and the voltage divider characteristic is mainly dominated by the larger resistance R_1. However, we note that we observed good agreement between $G_{SC,1}$ and $G_{1,SC}$ assuming that the measured voltage drops over R_1 overall. If we assume that we observe the voltage drop over R_{SC}, then with $V^*_{SD,R_{SC}} \approx 0.004 V_{SD}$ for $G_{SC,1}$ and $V^*_{SD,R_{SC}} \approx 0.14 V_{SD}$ for $G_{1,SC}$ we would obtain a very bad agreement between the two data sets. For $G_{SC,2}$ and $G_{2,SC}$ the effectively applied voltage on R_{SC} is $V^*_{SD,R_{SC}} \approx 0.14 V_{SD}$ independent of configuration. Hence, the data sets would still be in good agreement. However the apparent induced gap would reduce to $\Delta^* \approx 30\ \mu$eV, which is much smaller than what is usually observed both in our lab and literature [60, 144, 206]. We consider this as a first indication that we do indeed perform spectroscopy on a proximity region and not on the bulk SC contact. To further strengthen this finding, we now consider three-terminal measurements, with V_{SD} applied to either N1 or N2, while the current is measured on both SC and the other normal contact.

5.1.2. The conductance across the whole device

The three-terminal device allows more experiments, namely with V_{SD} applied to N1 and the current measured in both SC and N2. A schematic of this configuration can be found in Fig. 5.5(a) and (b). In Fig. 5.5(c) and (d) the conductances $G_{SC,1}$ (c) and $G_{2,1}$ (d) are plotted as a function of V_{BG} and V_{SD}. Note, that Fig. 5.5c) is the same as Fig. 5.3d) but shown again for completeness. We observe a very similar SC gap in both, $G_{SC,1}$ and $G_{2,1}$,

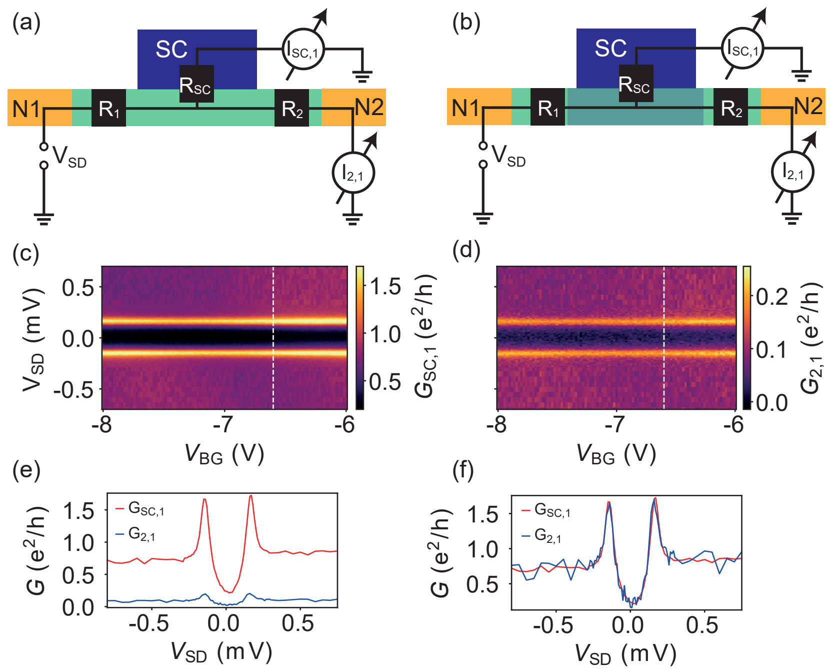

Figure 5.5. Conductance with bias voltage on N1. Schematic of the measurement where V_{SD} is applied on N1 and I is measured on SC and N2. The schematic illustrates the case without an induced proximity region (a) and with proximity region (b). (c) (d) Conductance $G_{SC,1}$ ($G_{2,1}$ as a function of V_{BG} and V_{SD}. e) Conductance G in dependence of V_{SD} for fixed $V_{BG} = -6.6$ V, no data processing has been done. f) Same as e) but $G_{2,1}$ has been scaled by a factor of 8.2, which results in very similar characteristics.

but the amplitude of $G_{2,1}$ is much smaller. To illustrate this we plot G in dependence of V_{SD} at $V_{BG} = -6.6$ V in Fig. 5.5e). The difference in amplitude is obvious. However, when the $G_{2,1}$ is multiplied by a factor of 8.2 the two data sets are nearly identical as is seen if Fig. 5.5(f). We explain this factor by R_1 being so much larger than all other resistances in the device, that it acts similar to a current source. Thus, only about $\frac{1}{8}$th of the current flows into N2 and the apparent conductance dI/dV is smaller by the same factor. We note, that our previously used resistances for R_S and R_SC have a ratio of $\frac{R_S}{R_{SC}} \approx 6.4$, which is smaller than the observed ratio between $G_{SC,1}$ and $G_{2,1}$. Using values for R_S and R_{SC} resulting in a ratio of $\sim 1/8$, leads to $G_{SC,1}$ and

$G_{1,SC}$ not agreeing as well anymore after correcting for the voltage divider. From this we conclude that there are additional effects besides a simple current divider affecting the measurement.

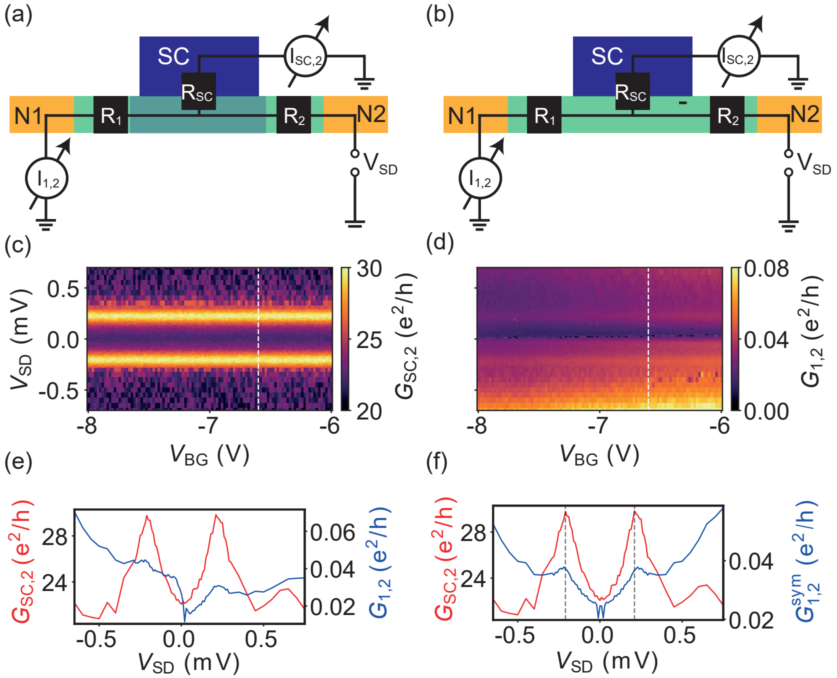

Figure 5.6. The conductance with bias voltage on N2. Schematic of the measurement setup where V_{SD} is applied on N2 and I is measured on SC and N1. The schematic illustrates the case without an induced proximity region (a) and with proximity region (b). (c) (d) Conductance $G_{SC,2}$ ($G_{1,2}$) as a function of V_{BG} and V_{SD}. e) Conductances $G_{SC,2}$ (red) and $G_{1,2}$ (blue) in dependence of V_{SD} for fixed $V_{BG} = -6.6$ V, no data processing has been done. (f) Same as (e) but for $G_{2,1}$ only the symmetric component is shown.

If V_{SD} is applied on N2 and the conductance is measured on SC and N1, as illustrated in Fig. 5.6(a) and (b), a very different characteristic is observed. Figure 5.6(c) shows $G_{SC,2}$, which has already been shown in Fig. 5.4(c). As before, we observe a SC gap with $\Delta^* = 210$ μeV, due to the voltage divider. However, unlike in Fig. 5.5(d) conductance $G_{1,2}$ does not show a clear SC gap with suppressed conductance. The most prominent feature is a distinct dip in conductance at $V_{SD} = 0$. To further illustrate this, Fig. 5.4(e) depicts the conductances $G_{SC,2}$ (red) and $G_{2,1}$ (blue) as a function of V_{SD} at fixed $V_{BG} = -6.6$ V. For $G_{1,2}$ we observe a signal asymmetric in V_{SD}, with no clear BCS coherence peaks. We observe that if we only take the symmetric component of $G_{1,2}$ with

$$G_{1,2}^{sym}(V) = \frac{1}{2}\left(G_{1,2}(V) + G_{1,2}(-V)\right), \tag{5.5}$$

and

$$G_{1,2}^{asym}(V) = \frac{1}{2}\left(G_{1,2}(V) - G_{1,2}(-V)\right), \tag{5.6}$$

we recover a signal that resembles a SC gap with coherence peaks corresponding to the ones found in $G_{SC,2}$. From this we conclude that we still observe the signatures of a SC gap in $G_{1,2}$. The origin of this large asymmetry is not exactly clear. A possible explanation could be finite bias effects [207], which could be very pronounced due to the tunnel barriers being distributed asymmetrically in the system as well as different junction lengths, and thus different screening effects.

We further note, that assigning $G_{LL} = G_{1,SC}$ and $G_{LR} = G_{1,2}$ we do not recover the, theoretically predicted [207, 208] and experimentally observed at low V_{SD} [209], symmetry relation $G_{LL}^{asym}(V) = -G_{LR}^{asym}(V)$ or the corresponding $G_{RR}^{asym}(V) = -G_{RL}^{asym}(V)$. We note that our measurement technique is not identical and unlike ref. [209], we do observe significant voltage divider effects as described above. Furthermore, the data presented in ref. [209] mainly focuses on bound states, which are not observed in this device. This symmetry relation is due to electron-hole symmetry. Thus, a tentative possible reason why we do not observe this, might be electron-hole asymmetry in our device. Possible origins could be the above mentioned finite bias effects [207], which might be amplified by the very open junction on the right NW side, or quasiparticle poisoning [207]. However, given our very asymmetric device structure and possible serial resistances of the built-in barriers and contact resistances might play a bigger role.

We now further our understanding on whether or not there is a proximity region below the SC in our device. We will first assume the case without a proximity region, illustrated in Fig. 5.6(b). Here, there is only one N-S interface to SC. Therefore, we assume that $R_1, R_2 = const.$ with respect to V_{SD}. Combining this assumption with the measurements of $G_{2,SC}$ in Fig. 5.4, we can conclude that R_{SC} has a dependence on V_{SD} similar to the curve in Fig. 5.4f) scaled by R_2. We now assume again $R_2 = 860\ \Omega$ and $R_1 = 32\ \mathrm{k}\Omega$, and assume $R_{SC} = 140\ \Omega$. Using again the model of a voltage divider, we find the voltage across R_1 to be similar to an inverted SC gap. Larger conductance on the coherence peaks of R_{SC} will result in a lower voltage drop over R_1. Assuming a constant resistance R_1 the current flowing into N1 should have the form of an inverted gap. However, this does not correspond to $G_{1,2}$, as seen in Fig. 5.6(d). Note, that assuming the measured $R_{SC,1}$ as resistance for R_1 also does not result in $G_{1,2}$.

Similarly, we now consider the case where V_{SD} is applied on N1 and we look at conductance $G_{2,1}$. Let us assume that only R_2 is constant and R_1 and R_{SC} both show the characteristic of a SC gap. Then the voltage dropping over R_2, using our voltage divider model, again shows the characteristic of an inverted SC gap and cannot result in the gapped conductance $G_{2,1}$.

From both these arguments, we conclude that both resistor R_1 and R_2 in our model are required to have a N-S interface characteristic, which suggest that a superconducting proximity region is induced in the NW segment below SC.

5.2. Superconducting proximity gap

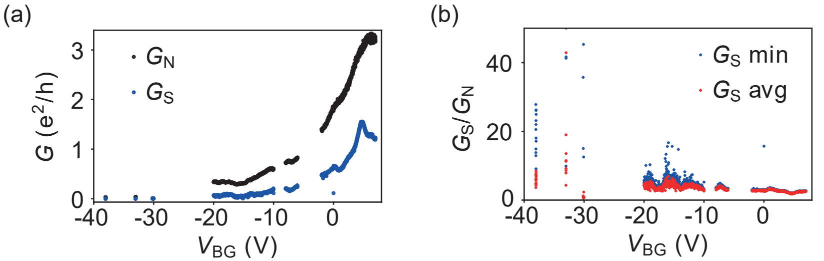

Figure 5.7. V_{BG} dependence of the below and above SC gap conductance. (a) Conductance G_N (G_S) above (below) the SC gap as a function of V_{BG}. (b) Suppression factor G_N/G_S as a function of V_{BG}. For the blue markers the minimum conductance was chosen for G_S and for the red markers the average of a few data points of the in-gap conductance was chosen. The above gap conductance G_N was always averaged over a few data points.

After characterizing the three-terminal measurements and arguing that we do indeed perform spectroscopy on an induced SC proximity region, we will now study the measured induced gap in more detail. Note, that all of the conductances discussed here correspond $G_{SC,1}$ of the previous section, which includes a built-in tunnel barrier between N1 and SC. In chapter 4 we have already shown the gate-dependence of the zero-bias conductance $G_S = G(V = 0)$ in the SC gap. In Fig. 5.7(a) we now show both the zero-bias and above-gap conductances, G_S and G_N respectively, as a function of V_{BG}. Both conductances decrease with more negative V_{BG} and G_S is reduced compared to G_N.

To study the subgap suppression, we show the suppression factor G_N/G_S as a function of V_{BG} in Fig. 5.7(b). Here, the absolute minimum in the gap is plotted in red, while the average over 10 μV in the gap is plotted in blue. As a result, we find an increase in suppression at more negative V_{BG}. The distribution in the suppression value increases at more negative V_{BG} due to worse signal to noise ratio for lower signal at low V_{BG}. A not noise dominated suppression of above ~ 50, a often cited criteria for a hard gap [204, 205], is not observed.

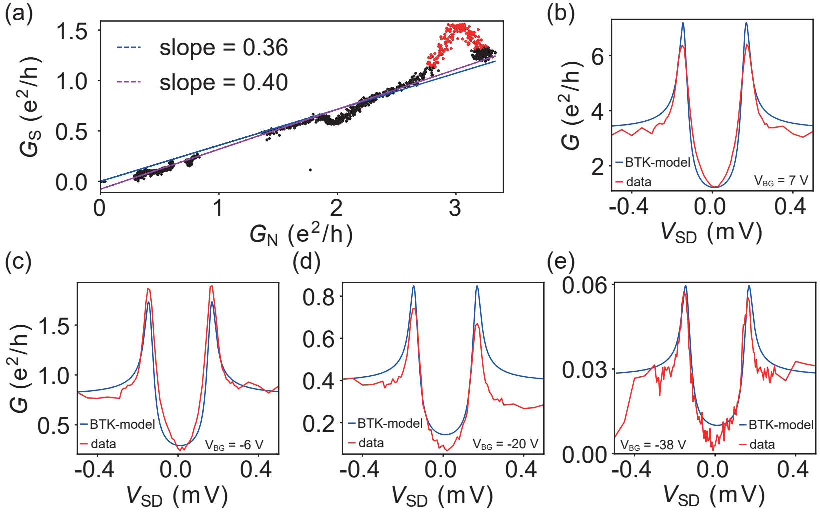

Figure 5.8. G_S as function of G_N and BTK-model. (a) In-gap Differential conductance G_S in dependence of above-gap conductance G_N. The blue dashed line is a linear fit to the data, excluding the red points. The purple dashed line is a linear fit with a y-axis offset. (b)-(e) Tunneling spectroscopy of the induced-gap (red) at different V_{BG}. The blue curve is calulated form the BTK-model [136] using temperature $T = 0.1$ K, SC gap $\Delta = 155$ μeV, and transmission through the barrier $t = 0.44$.

The general trend we find in these data can be understood based on the conductance through an N-S interface [210] given by $G_S = \frac{4e^2}{h} \sum_{n=1}^{N} \frac{t_n^2}{(2-t_n)^2}$, with N the number of modes, and t_n the transmission coefficient of mode n, while normal state conductance for the same multi-channel system would follow [210, 211], $G_N = \frac{2e^2}{h} \sum_{n=1}^{N} t_n$. To compare our data to these expressions, we plot the minimal conductance G_S as a function of the above-gap conductance G_N in Fig. 5.8(a). We observe a linear dependence of G_S on G_N. We fit a linear function to the data excluding the red data points. The blue dashed line describes a homogeneous linear fit with slope $m_1 = 0.36$ and the purple dashed line describes a linear fit with slope $m_2 = 0.43$ and a finite offset in the y-axis. While the purple line shows a better qualitative fit to the selected data, we would expect the curve to pass the origin, as both G_N and G_S should be zero when no modes with finite transmission are present in the system.

Comparing the conductance through an N-S interface formula to a the normal state conductance, assuming a constant number of modes and identical $t_n = t \,\forall\, n$ we would expect a dependence of $r = G_S/G_N = \frac{2t}{(2-t)^2}$. However, we clearly observe a linear dependence of r in V_{BG}. From this we conclude that the transmission of the transport modes does not change much with gate voltage. We extract an average transmission $\bar{t} = 0.44 \pm 0.05$ over all modes based on the slope of Fig. 5.8(a). We understand this as the transmission coefficient through the built-in tunnel barrier between N1 and SC. We use $\bar{t}$ to model our SC interface with the BTK-model [136]. In Figs. 5.8(b)-(e) the data of the tunneling spectroscopy at different V_{BG} is plotted in blue. The red data is the BTK-model using $\bar{t}$, which corresponds to a barrier strength of $Z = 1.14 \pm 0.09$, an induced SC gap $\Delta^* = 155$ μeV, and the fixed temperature $T = 0.1$ K. We see a general but not great agreement between the BTK-model and our data. We note, that the softness at less negative V_{BG} cannot be well-modeled even by adding a phenomenological Dynes-parameter [212] to add poisoning to the model. Each of Figs. 5.8(b)-(e) could be fitted better by adjusting some of the parameters, however parameters such as the temperature are expected to stay constant throughout the measurements. From this we conclude that there is probably still some small variation in the transmission t on V_{BG}.

In general, we can capture the general characteristic for reasonable parameters using the BTK-model. We observe that a possible reason for our soft gap might be insufficiently strong barriers. The fact that t and therefore the tunnel barrier seems weakly back gate dependent or even independent is puzzling. In chapter 4 we showed that tunnel rates Γ of a QD are tunable. Based on our previous discussion in chapter 4 we speculate the barrier region might be screened by the very close (about ~ 20 nm) SC contact and a (nearly) constant, badly tunable tunnel barrier results.

Now we discuss the impact of the distance between tunnel barrier and SC. We estimate a distance between SC contact and tunnel barrier of about $\sim$ 20 nm on the side of contact N1 and for the N2 contact side 0 from SEM images. The tunnel barrier is shorted by the SC contact on the N2 contact side, as shown by the much larger conductance we measure on that NW side. We can also model the conductance $G_{SC,2}$ with the BTK-model, we need a much higher transmission of about $t \approx 0.7$. This again agrees well with our observation, that no built-in barrier is present on that side and that t corresponds to the transmission through the barrier on the N1-SC side. Note, that to get decent agreement with the BTK-model we need to add a Dynes-parameter much larger than on the N1 side. Using a similarly large Dynes-parameter to model $G_{SC,1}$ results in a much too soft gap.

We speculate about two possible explanations. The proximity gap gets poisoned from the normal conducting contacts N1 and N2, since there is a much weaker barrier between N2 and the proximity region more quasiparticles can poison the gap. Another possible explanation is the number of modes in the system. The conductance $G_{SC,2}$ is nearly an order magnitude larger than $G_{SC,1}$, therefore we would expect a much larger number of modes to contribute to transport. Possibly some of these modes couple weaker or not at all to the SC, which leads to an increased poisoning.

Furthermore, we would like to point out that we have not seen any general influence of the distance between the tunnel barrier and the SC contact on the hardness of the gap. As long as the tunnel barrier is not shorted a suppression of about a factor of $6-15$ is observed. This has been seen in devices with close SC contacts to the barrier, such as the one discussed here, as well as devices were the distance between SC an barrier was above 100 nm.

5.3. Summary and Outlook

In conclusion, we have shown evidence for an induced SC proximity region in an InAs NW using three-terminal measurements. We have shown how very asymmetric tunnel barriers can lead to voltage division effects in the measurements. While they might seem trivial at first glance, their presence can distort experimentally extracted parameters such as the induced SC gap Δ^*. We have further shown an increase of the suppression factor G_N/G_S ("gap hardness") for more negative back gate voltages.

Furthermore, we observe a linear dependence of G_S on G_N, implying that our back gate mainly tunes the number of modes contributing to transport and not their transmissions. We have extracted average transmissions of all modes of $\bar{t} \approx 0.44 \pm 0.05$ with a built-in tunnel barrier and $\bar{t} \approx 0.7$ for a bare NW segment. With these transmission values we can model both gaps with the BTK-model. We get a good general agreement for a large gate range with some discrepancies. These cannot be explained by simply adding a Dynes-parameter to include quasiparticle poisoning for the gap measured on the built-in tunnel barrier.

For the bare NW segment, we need to include substantial quasiparticle poisoning into the model via a Dynes-parameter to get good agreement to the data. We speculate that this is either due to a very high number of modes, which do not all couple sufficiently to the SC or quasiparticle poisoning through the leads, which is unhindered without any barrier. We note, that one possible reason that we do not observe a hard gap, could be simply too weak tunnel barriers. However, this does not explain the difference in poisoning with or without tunnel barrier.

We observe that, for tunnel barriers very close to the SC we do not observe any tunability of the barrier. We speculate that this is due to screening effects of the SC contacts. This could further explain, why we do not observe spurious QDs for such close barriers. However, in general we have not observed any dependence of the gap hardness on the distance between tunnel barrier an SC contact.

As the height of the tunnel barrier is given by the offset in conduction band of wurtzite and zincblende, the barrier height cannot be tuned by growth in this NWs. It would be possible to grow longer tunnel barriers, which should exponentially suppress transport. The SC contact could also be placed further away from the barrier to allow for more gate tunability. However, this would possibly destroy the clean tunnel barrier and lead to spurious QD formation, which is undesired. We note that similar soft gaps have been observed in hard-wall InAs NW with InP barriers [100]. However, high gate voltages were necessary to observe superconductivity in that work, which might have decreased the barrier strength.

To study whether the origin of our soft gap lies in the weak tunnel barrier or in quasiparticle poisoning, we will investigate a Cooper pair island in the next chapter. By studying the parity of the Cooper pair island in dependence of magnetic field, we hope to gain some further knowledge of this issues.

6 Charge sensing of a superconducting charge box

In this chapter we discuss our results of a superconducting island fabricated in the proximity region of a crystal-phase defined InAs NW. By evaporating a homogeneous aluminium (Al) film much thinner than the NW, the Al disconnects at the edge of the NW, creating a disconnected thin film on the NW with strongly coupled self-aligned Al pads, which can be used as side gates (SGs). However, in the fabrication process the two Al SGs were not sufficiently etched to completely remove the native oxide before the contact lead evaporation. The resulting bad contacts created a superconducting charge box (SCB) ("Cooper pair island") in each SG, for which the QD in the NW acts as a charge detector. We will show clear evidence of Cooper pair islands in the SG, such as $2e$-periodicity in the superconducting state and a halving of the capactive shift in the detection in the normal state. Furthermore, we will present time-resolved measurements of Cooper pair tunneling via charge detection. However, for the proximitized QD in the NW none of the above mentioned signatures of Cooper pair islands could be found. We see evidence of superconductivity, but no sign of the 2e-periodicity of the discrete charge we would expect of a unpoisoned Cooper pair island. From the clear differnce of the bare Al-island to the NW-island, we conclude that our Al is of good quality itself and the reason we do not measure a Cooper pair island in the NW must lie either with the induced superconductivity or the NW itself. We will conclude that the most likely reason, lies with the many conductance channels in the NW. We hypothize that no all of these channels couple well to the SC leading to unproximitzed channels poisoning induced superconductivity.

6.1. Cooper pair island device

A false colored SEM picture of a typical device is shown in Fig. 6 a). The sample was fabricated with standard e-beam lithography as explained in chapter 3. We will only quickly note the important differences to the standard fabrication. The Cooper pair island is defined by two wurtzite barriers (red), which are more than 1 μm apart. A thin film of Al is evaporated between these barriers to create the Cooper pair island. We evaporate 12 nm of pure Al at a sample holder temperature of -75°C. As the NWs have a width of around 80 to 100

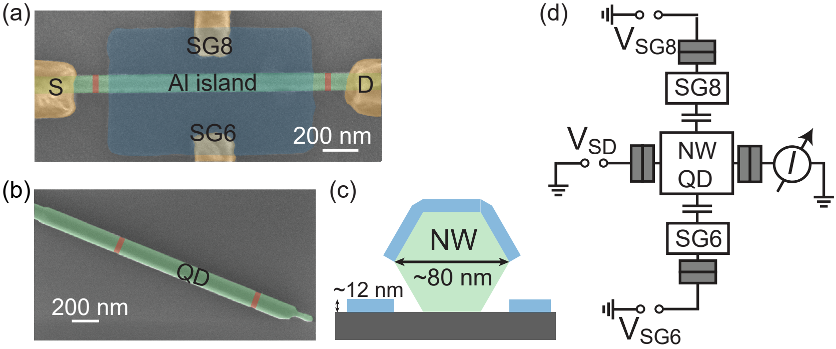

Figure 6.1. Nanowire QD and SG charge boxes. a) False color SEM picture of a similar device as discussed in this chapter. The normal contacts and gates made from Ti/Au are colored in yellow. The superconducting island is blue. The NW is colored in green, the wurtzite barriers are colored red. b) False colored SEM picture of the NW measured before any contacting or etching was done. The colors are the same as for a). c) Schematic cross-section of the device. The NW (green) has an hexagonal shape, which shadows the area below. A thin (∼ 12 nm) layer of Al breaks off at the edges of the NW and a thin isolated Al island is left on the NW. d) Electronic schematic of the device. The NW QD is both capacitively and tunnel coupled to the source drain leads. A bias voltage is applied and the current is measured. The SGs couple capacitively to the NW QD. They are tunnel coupled to their respective leads leading to the formation of superconducting charge boxes.

nm and a hexagonal shape, the Al is to thin to connect both the substrate and the NW top. Therefore, it will be disconnected at the edge, leaving us with a thin Al film on the top two or three facets of the NW (depending whether the NW lies ridge up of face up), and with two large pads of superconducting Al very close to the NW. In a next step we contact both the NW and these Al pads with Ti/Au contacts. Before evaporation a in-situ Ar milling step of 30 s is done to remove the native oxide on the NW and the Al. If desired additional SGs can be fabricated. Contacting the thin Al pads creates two SGs very close to the NW. As they are evaporated simultaneously with the island, they are self aligned and mainly tune the NW below the superconductor. Due to their close proximity we find lever arms of around 0.53 eV/V if both SGs are swept together, much larger than the lever arm to the global Si back gate of 0.04 eV/V. In conclusion we fabricate very strongly coupled self aligned SGs to a superconducting island on the NW.

6.2. QD as charge sensor for the superconducting charge boxes

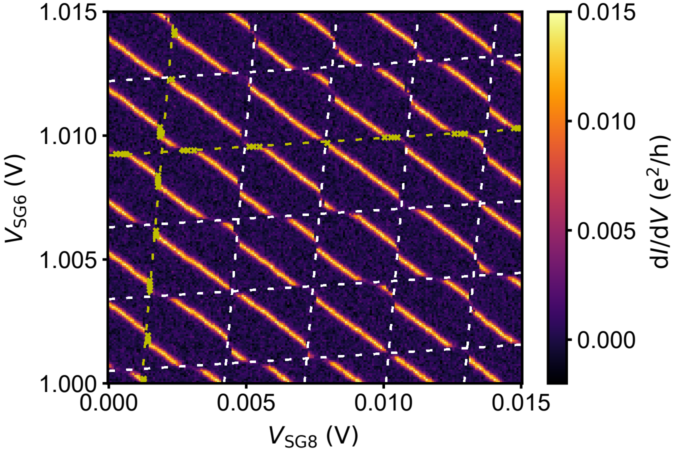

Figure 6.2. Large gate-gate map of the Cooper pair island. The differential conductance $\mathrm{d}I/\mathrm{d}V$ in dependence of SG voltages V_{SG8} and V_{SG6} at zero external magnetic field. The bright diagonal lines are the QD resonances. They are periodically shifted in gate voltage, as we would expect for a parallel TQD. The white dashed lines are a guide to the eye to the shifts. The yellow dashed lines were fitted to the yellow crosses and their slopes used for the white dashed lines.

Figure 6.2 shows the conductance of the NW as a function of V_{SG8}) and V_{SG6}. The single QD resonances are clearly visible as bright lines. From the negative slope of -0.83 of the resonances, we conclude that we have very similar lever arms of the Al SGs on the device, as one would expect from the symmetric device geometry. The most striking feature is the periodic shift of the resonances. The yellow points, where the shift was observed, were manually extracted and a linear fit interpolates over the full gate voltage range (yellow dashed line). We extract a slope of $a_h = 0.071$ and $a_v = 12.65$ for the horizontal and vertical line respectively. Using the same slopes and manually optimizing the offset, the white dashed lines were added. The difference between the y-axis offsets at the origin of two neighboring lines is 37.1 ± 0.7 mV for the vertical lines and 2.92 ± 0.04 mV for the horizontal lines. Note, that the spacing for horizontal lines is smaller due to extracting the vertical offset at the origin. The lines are very evenly spaced, confirming a periodic shift of the resonance lines.

We attribute these shifts of the resonance lines to the formation of capacitively coupled charge boxes in both Al SGs. Our data resembles serial triple quantum dots (TQD) [93]. However, as the SCB are in the SGs and not the NW, they only couple capacitively and we do not observe any conductance change at the intersection of the single charging lines as is usual for serial TQDs. In our case, whenever a charge tunnels into one of the SCBs the electrostatic potential in the vicinity of the NW QD is changed. Due to the proximity to the NW, the NW QD is sensitive to this potential change and the Coulomb blockade resonances get shifted. Since the Coulomb blockade resonances are narrow they are very sensitive even to tiny changes in the electrostatic potential and our NW QD can be used as a charge detector for the charge on the SCBs. We see that $a_h \ll 1$ and $a_v \gg 1$, which shows that these shifts are mainly tuned by one gate with very little cross talk, further confirming our assumption that these charge boxes reside in the SGs. After the initial measurements, additional leads were fabricated on the Al pads of similar devices of the same fabrication batch with the same etching recipe. Between two leads connected by the Al pad we measured a resistance of a few MΩ at room temperature. This shows that our SGs are not well-connected to the bond pads, presumably due to insufficient etching of the native oxide. These thin insulating layers create tunnel barriers, allowing the formation of charge boxes on the Al pad [213]. In the first part of this chapter we will focus on characterizing the SCB using the NW QD as a charge detector. We will return to the properties of the NW QD in more detail later.

6.2.1. Magnetic field dependence

Gate dependence of SG QDs

In Fig. 6.3 we show a zoom-in on four "squares" of these capacitive shifts at an out-of-plane magnetic field B_Z of 0 (a), 10 mT (b), 24 mT (c), and 40 mT (d). For Figs. 6.3a) and b) two white dashed lines mark the edges of the shifts, from the distance between the two lines we later extract their error in gate space. We see that at zero field and 10 mT there are only two shifts in the V_{SG8} and V_{SG6} interval investigated here. At 24 mT this lines start to split into two at the same time the capacitive shift starts to decrease. At 40 mT the lines are completely split into four nearly equidistantly spaced lines for V_{SG6} and three for V_{SG8} as one of the lines moved out of the measurement window. Again, we note that the capacitive shift of the lines is much less pronounced at larger B_Z. The full data set with all magnetic field maps can be found in Appendix C.1.

In a next step we investigate the shift of the charge detection signal, i.e.

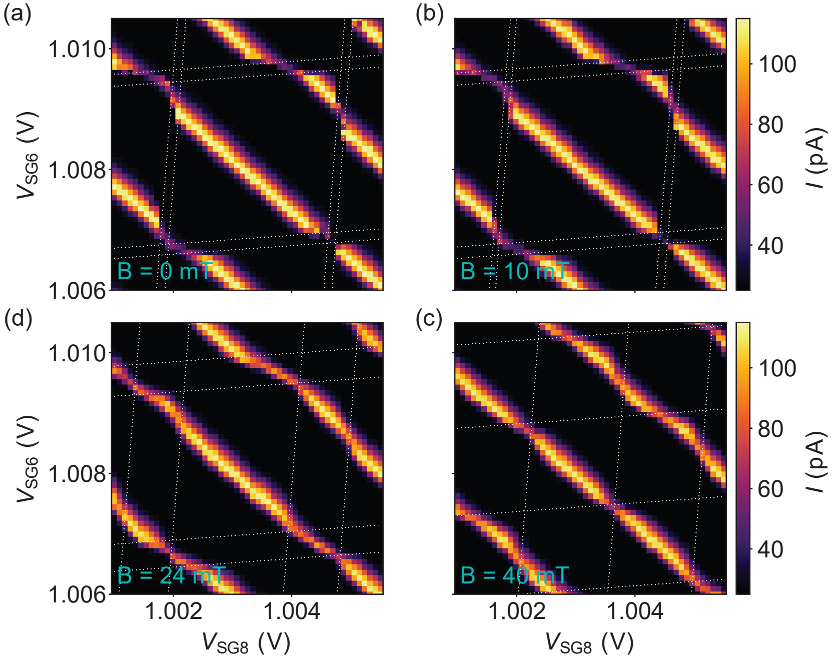

Figure 6.3. SG maps at different magnetic fields. Current measured through the DQD in dependence of both SG voltages V_{SG8} and V_{SG6} for out-of-plane magnetic fields 0 mT (a), 10 mT (b), 24 mT (c), and 40 mT (d). The white dashed lines mark the borders of the shifts of the resonance lines in (a) and (b), corresponding to single charging of Cooper pairs in the SCBs. In (c) and (d) the lines split into two additional shifts, because superconductivity is destroyed and the island becomes charged by electrons.

we extract the offset between the white dashed lines and plot them against the magnetic field. The result is shown in Fig. 6.4. We note that as all the lines are parallel, it does not matter in what voltage we take the offset or their exact value. For simplicity, we take the offset in V_{SG6}. We can view this as a projection of both sets of lines on the V_{SG6} axis. As our NW QD effectively acts as a charge detector for the SCBs, observing a shift is equivalent to a Coulomb blockade resonance occurring in one of the SCBs. This allows us to extract the magnetic field dependence of the charge states of the SCBs in Fig. 6.4. We see that the peaks do not significantly change in magnetic fields up to 20 mT. For higher fields, they split into two lines, which move apart until they become

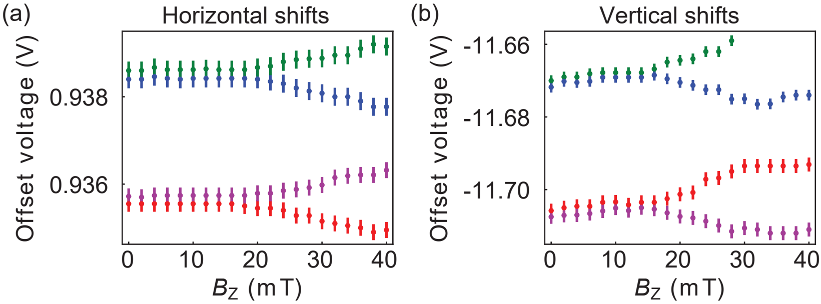

Figure 6.4. Gate vs magnetic field dependence of the SCBs. The extracted offset voltage in V_{SG6} for the white dashed lines in Fig. 6.3 is plotted against the applied magnetic field B_Z. As the NW QD acts as a charge detector, this is effectively projecting the Coulomb resonances of the side-coupled QDs on V_{SG6} as a function of the applied magnetic field.

constant at a field around 40 mT. This are the characteristics we expect from a Cooper pair island [43, 214, 215]. At low field, due to the superconductivity, only Cooper pairs are allowed to enter or exit the island, leading to Coulomb blockade resonances with a spacing of $2e/\alpha$ in gate voltage. As the magnetic field is increased the superconducting gap shrinks until it is smaller than the charging Energy $\Delta < E_C$. This allows the transport of single electrons on to the charge boxes, leading to Coulomb blockade resonances with a spacing of $1e/\alpha$. Comparing the peak spacings at low field, from zero to 10 mT, and around 40 mT for the horizontal resonances originating from SG_6 and from 30 to 40 mT for the vertical resonances originating from SG_8, yields a ratio of 2.0 ± 0.1 for the SG_6 resonances and 1.97 ± 0.09 for the SG_8 resonances. This is in good agreement with the expected ratio of 2 for a Cooper pair island without quasiparticle poisoning.

Amplitude of capacitive charge sensing signal

To further prove that we are detecting a double electron charging on the Cooper pair boxes with our NW QD, we extract the capacitive shift for every magnetic field map in Appendix C.1. As a illustration we show two SG_6-SG_8 maps at 0 mT and 40 mT in Figs. 6.5(a) and (b), respectively. On the top right the resonances of the SCBs do not cross on the resonance of the NW QD. Hence, the capacitive shifts do not compensate each other due to the symmetry of the system. Therefore, we use the top right line to extract the shifts. We denote the line defined by the red points in Fig. 6.5 as the not shifted resonance and the blue marks as the shifted one. We fit parallel lines through

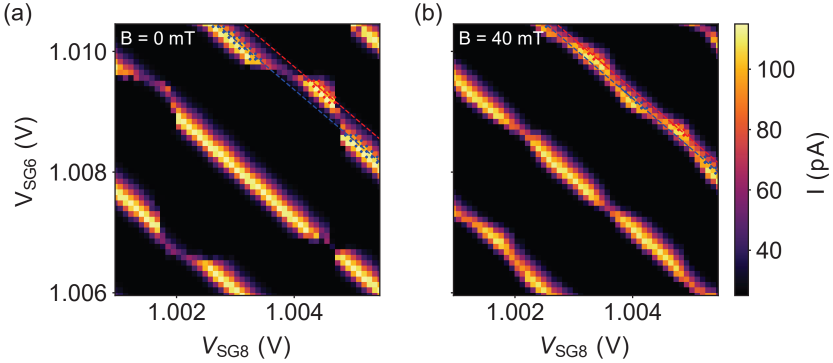

Figure 6.5. Capacitive shift extraction. Two example maps of the capacitive shift extraction at 0 mT (a) and 40 mT (b). The measurements points marked in red describe the unshifted resonance line, the blue one the capacitively shifted resonance. The red and blue lines are fit through these points with the same slope given by the blue line.

both datasets and extract the x and y-axis offsets of these lines. As the lines are parallel the offset difference corresponds to the voltage shift necessary to compensate the electrical potential shift due to the additional charge on the Cooper pair boxes either on V_{SG8} or on V_{SG6}, respectively.

In Fig. 6.6 we plot the extracted voltage shifts against magnetic field B_Z. Figure 6.6(a) shows the absolute extracted voltage shifts, while 6.6(b) shows the same data normalized to the respective average of the extracted shifts up to 18 mT. We see a similar characteristics as in Fig. 6.4, namely that the shifts stays constant up to around 15 mT. At higher magnetic fields the shifts decreases drastically until they saturate at half the zero field value. This behavior is again well described by the notion that the SGs form superconducting charge boxes, with charges that we detect with our NW QD as charge sensor. Below the critical field of Al the SCBs are charged up by integer numbers of Cooper pairs with an electric charge of $2e$. As superconductivity is destroyed at higher magnetic fields, the islands become populated by single electrons with an electric charge of e. For this reason, we would expect capacitive shifts of half the magnitude in the normal state as compared to the superconducting state, as observed here. We take an average at low field (0 to 18 mT) and high field (24 to 40 mT) and calculate their ratio to be 2.1 ± 0.3 for both V_{SG6} and V_{SG8}.

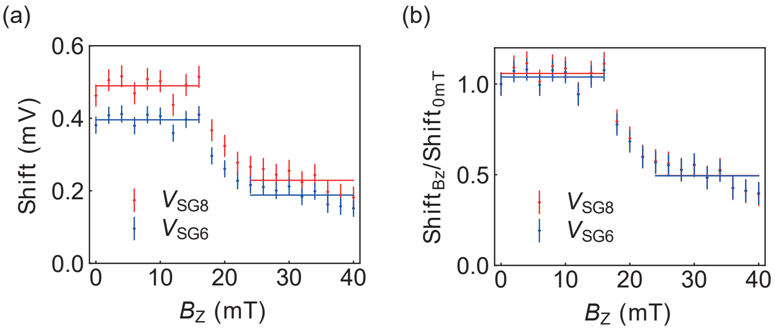

Figure 6.6. Magnetic field dependence of the capacitive shift. (a) shows the absolute extracted shift in values of V_{SG8} (red) and V_{SG6} (blue). The horizontal lines show the averaged shift for high and low fields respectively. (b) shows the normalized capacitive shift by the average at low field.

6.2.2. Time-resolved tunnel events

To further study the Cooper-pair islands in the SGs, we performed time-resolved charge detection measurements. Figure 6.7(a) shows a SG$_6$-SG$_8$ map similar to what has been discussed above to study the magnetic field dependence. However, here the current $I(t)$ is measured as a function of time t for each gate voltage of the map and and the color scale corresponds to the average current I_{avg} of each time-trace. This alone is not significantly different from standard measurements, but the recorded data in addition allows us to investigate the fluctuations around the average number. In contrast to standard experiments, we set the integration time as low as possible, such that we still have a reasonable signal-to-noise ratio, and perform the averaging numerically. The average time between two measurements points is about $\delta t \sim 36$ ms, faster measurements were not possible with our standard setup.

Three of these time-dependent current measurements are shown in Fig. 6.7(b). The colors of the lines corresponds to the marked gate voltages in Fig. 6.7(a). We observe three qualitatively different characteristics. For the green curve distinct steps in the current can be observed. In Fig. 6.7(c) the corresponding histogram is shown. The measured current range is separated in 100 equally sized intervals ("bins") and the number of data points in each interval is counted. Two distinct peaks are visible, corresponding to the two distinct current values observed in Fig. 6.7(b). The solid black line is a bimodal ($\mathcal{B}$)

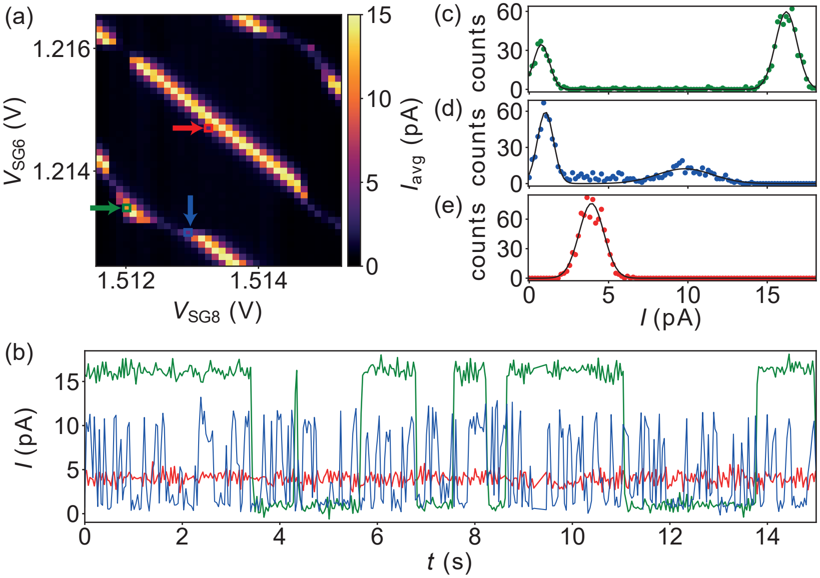

Figure 6.7. Time-resolved tunneling of a Cooper-pair. (a) Averaged current of a series of time-resolved current measurements. Each point in V_{SG8} and V_{SG6} corresponds to the average current of a single time-dependent current measurement. (b) The time dependence of the current for the three points with marked borders (red, blue, green) with corresponding line color. (c), (d), (e) Histograms of (b) with corresponding colors. The black line is a bimodal (c,d) or gaussian (e) fit to the data.

fit of two Gaussian ($\mathcal{N}$) to the data with:

$$\mathcal{N}(x, \mu, \sigma) = \exp\left(\frac{(x-\mu)^2}{2\sigma^2}\right) \tag{6.1}$$

$$\mathcal{B} = pA \cdot \mathcal{N}(x, \mu_1, \sigma_1) + (1-p)A \cdot \mathcal{N}(x, \mu_2, \sigma_2), \tag{6.2}$$

where $\mu_{1,2}$ describes the position of the Gaussian and σ the standard deviation, parameters A and p describe the absolute and relative height of the two Gaussian composing the bimodal distribution.

The histogram further illustrates the observation from Fig. 6.7(b), that there are two discrete signal levels between two distinct current values. We perform the same analysis for the blue curve in Fig. 6.7(b), with the resulting histogram and fit shown in Fig. 6.7(d). While there are still two peaks as in Fig. 6.7(c), the peak at higher current is not as prominent. There are a significant amount of counts in between the peaks. We explain this by different rates in the current switches, as can be seen in Fig. 6.7(b), for the blue curve no clear plateaus at the higher current value are observed only switches between the two current values within a few measurement points. The switching between current values happens at different rates. We will come back to this observation later. In Fig. 6.7(e) the histogram for the red curve in Fig. 6.7(b) is shown. Here, the data is described by a single Gaussian $A \cdot \mathcal{N}$. Note, that we observe four distinct current values in the three time dependent measurements shown, as the current values measured depend on the NW sensor-QD resonance position.

To analyze the data more quantitatively we extract the number of steps in current per time trace. For each time trace the derivative is taken and the derivative is compared to a threshold values. If the derivative exceeds the threshold a up (down) step is counted for a positive (negative) derivative. The number of up steps and down steps are then added and divided by two to obtain the total number of steps n_s in a time trace. Note, that the threshold current and derivative values depend on the maximum current measured in the device. As this can differ between different measurement, i.e. because of a different bias voltage, this value has to be adjusted between data sets with different measurement parameters, but should stay consistent within one data set. Also, this method might ignore some steps with a low current difference, due to the bad signal-to-noise ratio. However, for most of the data set the algorithm performs adequate as verified by manual inspection. Once we extract the number of steps n_s per trace, we calculate the rate $\Gamma = \frac{n_s}{t_{meas}}$ by dividing the step number by the total measurement time $t_{meas} \approx 29$ s of one time trace.

Figure 6.8(a) shows the extracted switching rates as a function of the gate voltages V_{SG8} and V_{SG6}. We observe rates ranging from 0.05 Hz up to rates of 8.0 Hz. Given the average waiting time between two measurement points $\delta t \sim$ 36 ms, the maximal detectable rate for our system assuming perfect detection is $\frac{1}{3\delta t} \approx 9.5$ Hz as the maximum number of switches would correspond to one step up and down within three measurement points. Conversely, the minimal detectable rate is $\frac{1}{t_{meas}} \approx 0.034$ Hz, corresponding to one step in the total measurement time. We conclude, that while we could increase the lower limit of Γ by measuring longer, we are limited by our type of measurement for high frequencies. In Fig. 6.7(b) the limitation is already clearly visible in the blue curve. We mainly detect single peaks not plateaus. Additionally, in Fig. 6.7(d) we observe a significant amount of counts between the two peaks, signifying that the switching happens so fast, that the instrument cannot resolve the signal anymore.

Figure 6.8(b) shows the average current I_{avg} per time trace vs. V_{SG8} and V_{SG6}. To illustrate the distributions of slow and fast tunnel rates better we mark point with switching rates > 1 Hz with white borders and the ones with switching rates > 0.05 Hz with blue borders. All points without marked borders did not show any detectable switching. As a guide to the eye pink-

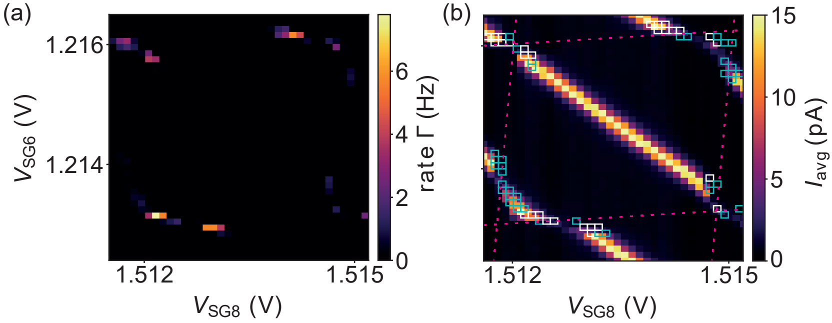

Figure 6.8. Switching rates. (a) Extracted switching rate Γ as a function of V_{SG6} and V_{SG8} between the high and low current values in the time-resolved measurements. (b) Averaged Current I_{avg} of the time dependent current traces in dependence of V_{SG8} and V_{SG6}. The borders mark points with switching rates $\Gamma > 1$ Hz (white) and with rates $\Gamma > 0.05$ Hz (blue). The pink dashed lines are a guide to the eye for the position of the resonances of the SCBs.

dashed lines were added to where the SCBs are on resonance. We observe that all the switching happens in vicinity to the resonance points of the SCBs. As a general trend we find faster switching rates for the resonances corresponding to the QD in SG_6 ("horizontal" pink-dashed lines) and slower rates for the QD in SG_8 ("vertical" pink-dashed lines).

We will now discuss the physical origin of the observations made above. We have shown already that the NW QD is strongly capacitively coupled to the SCBs. We see this from the strongly visible shift in the NW-QD resonances. In combination with the fact, that we only observe steps in current when the SCBs are close to resonance, we conclude that our NW QD acts as a charge detector to the SCBs and we detect the loading and unloading of the SCBs in the time-resolved measurements. As previously shown, that the SCBs are proper Cooper pair islands, we conclude that we observe single Cooper pairs tunneling into and out of the SCBs.

Furthermore, we find different tunnel rates between the two SCBs. We are not sure about the physical origin of this difference in tunnel rates. Both SGs were fabricated in the same fabrication steps and so were the Au leads connecting them to the bond pads. The overlap between the Al pads and the Au leads are nearly identical. From the design they are estimated to be about 0.016 $\mu\mathrm{m}^2$ for SG_8 and 0.015 $\mu\mathrm{m}^2$ for SG_6. We see that SG_8 has the slightly larger overlap area, which does not agree with the observation of a significantly slower tunnel rate. We speculate the non-identical native oxide layers and the partial etching could be responsible for the difference.

We note, that the NW-QD is not an ideal charge detector as tuning the SCBs also strongly tunes the NW QD due to the strong lever arm and the absence of other gates apart from the global BG. Therefore, it is not possible for the NW QD to stay on resonance and act as a detector while independently tuning the SCBs. We also observe this in the different current levels in Fig. 6.7(b). The sensitivity of the charge detection depends on the slope of the Coulomb blockade resonance of the detector QD. The higher the slope, the stronger the detection signal. Hence, we see the largest currents (and best signal-to-noise ratio) at the side of the NW-QD resonance, the further we move away from there the smaller step in current becomes. Consequently, if the NW-QD is in blockade, no detection can happen. This could possibly be counteracted with additional SGs although the high lever arm of the Al SGs might make this challenging.

We compare the measurement in Fig. 6.8 in the superconducting state at zero magnetic field to the measurements shown in Fig. 6.9 performed in an out-of-plane magnetic field of 40 mT. In Fig. 6.8(a) we plot again the averaged current I_{avg} for each time trace for the whole V_{SG8} vs V_{SG6} map. As before, we observe a decrease in resonance shift and half the distance between two charge box resonances. Figure 6.9(b) shows the corresponding extracted tunnel rates Γ. We detect switching only at two points in the whole map. Both of these we attribute to noise in the current being detected as step by the algorithm by direct inspection. Note, that we could have filtered this points out by increasing the threshold currents, but refrained as we wanted to compare the data sets with the same analysis. Checking the actual time traces corresponding to these points reveals no steps (see Appendix C.2)), just noise. This finding of no switching events in N-state can have two origins: first, too fast and too many tunneling events for the detector, second, too slow and too few tunneling events to observe in t_{meas}. According to the BTK-model [136], interfaces with low transparencies strongly suppress superconductivity in the gap, most states are normal reflected and very little Andreev reflection is possible. From the low tunnel rates we detect in the few Hertz range, we can safely assume that our interfaces have low transparency. As we have detected 2e-periodicity for the Cooper pair islands in the SGs, we can assume that quasiparticle poisoning is very low and the Al of the SGs indeed shows a hard superconducting gap. As the magnetic field is increased and the induced superconducting gap becomes smaller than the charging energy $E_C > \Delta^*$, single electron transport on the charge box in enabled. Therefore, increasing the transparency and the tunnel rates.

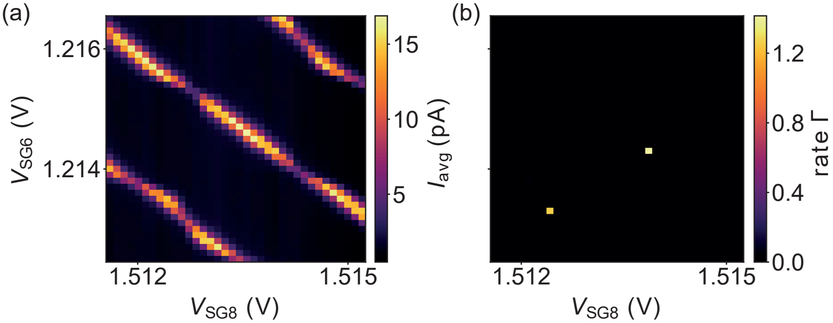

Figure 6.9. Time-resolved measurements 40 mT. (a) Averaged current I_{avg} per time-resolved trace in dependence of V_{SG8} and V_{SG6} at an out-of-plane magnetic field of 40 mT. (b) Corresponding extracted rates Γ. The only $\Gamma > 0$ extracted are attributed to noise and no measurable rates are extracted.

6.3. Proximitized nanowire quantum dot

In the previous part of this chapter we have shown that we can make a Cooper pair island with the bare Al SGs on the substrate. However, our goal was to make a Cooper pair island on the NW, so far we have not discussed signatures of that. Therefore, we will now focus in this section on the actual NW QD. Figure 6.10 shows four measurements of Coulomb diamonds. Figures 6.10(c) and (d) were measured on the same NW used above as a charge sensor. Figures 6.10(a) and (b) were measured on a similar NW from the same fabrication batch. They show very similar characteristics, but with different addition energies.

In Fig. 6.10(a) the differential conductance $G = dI/dV$ is shown as a function of both Al SGs with the same voltage V_{Al} applied to both SGs. and the bias voltage V_{SD} at zero magnetic field and a $V_{BG} = 0$ V. For $|V_{SD}| \leq \pm 100$ μV the conductance is suppressed, as expected from standard QDs coupled to one superconducting reservoir [60, 78, 127, 144, 148, 216, 217]. The position is marked in Fig. 6.10(a) with white dashed lines. In Fig. 6.10(b) the same measurement at a constant magnetic field $B_Z = 0.5$ T is shown. We observe that the suppression of conductance at $|V_{SD}| \leq \pm 100$ μV has vanished. In general, Fig. 6.10(b) shows a larger conductance overall. As 100 μV is a reasonable value for a small induced superconducting gap Δ^* of Al and its effects vanish with a low magnetic field, we attribute the suppression of conductance at $|V_{SD}| \leq \pm 100$ μV to the induced proximity superconductivity. Note, that the charging energy $E_C \approx 320 \pm 10$ μeV in Fig. 6.10(a) is clearly larger than $2\Delta^*$ (note, the factor of 1/2 due to the definition of E_C, also see chapter 2),

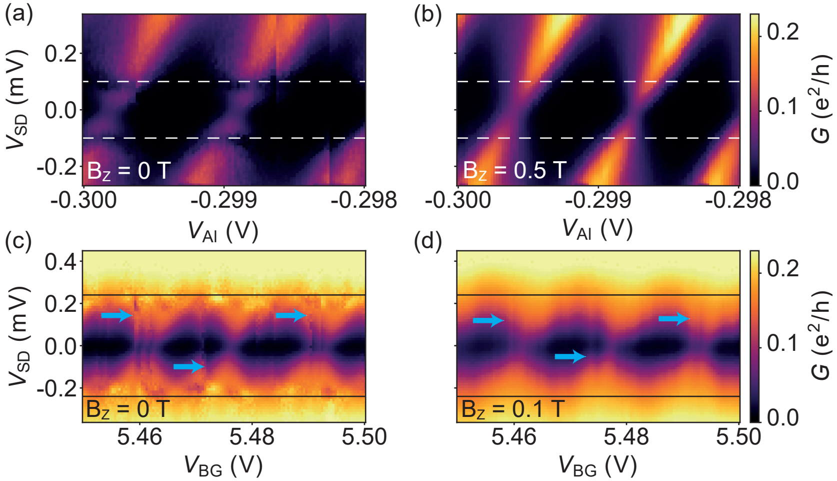

Figure 6.10. Coulomb blockade diamonds of a superconducting island. (a) Differential conductance $G = dI/dV$ as a function of the bias voltage V_{SD} and voltage V_{Al} applied to both SGs at zero magnetic field and back gate $V_{BG} = 0$. (b) Same measurement but at magnetic field $B_Z = 0.5$ T. The white dashed lines are guides to the eye at $V_{SD} = 100$ μV in both graphs. (c) Coulomb blockade diamonds as a function of V_{BG} and V_{SD} at zero magnetic field and $V_{Al} = 0.5$. (d) Same as (c) but at $B_Z = 0.1T$. The black lines are guides to the eye at $V_{SD} = 240$ μV. The jumps in (c) and (d) are reproducible and induced by the SCBs. Three of these jumps are marked by blue arrows. There amplitude is reduced in (d) as superconductivity in the SCB is destroyed and the capacitive shift is halved.

therefore a proper Cooper pair island with 2e-periodicity would not be expected. However, for E_C not much larger than Δ^* even-odd effects in E_C would be expected for an unpoisoned Cooper pair island [146, 147], as we have discussed in chapter 2. The system most closely resembles a proximitized QD with $E_C > \Delta^*$ [60, 78, 127, 144, 148, 216, 217].

Figure 6.10(c) and (d) show a similar Coulomb diamond measurement at a higher gate voltages. Here, the conductance is measured as a function of V_{BG} and V_{SD}, while $V_{Al} = -0.5$ V. Similar to Fig. 6.10a) and b) at zero magnetic field there are features visible which vanish at a finite magnetic field above the critical field of Al. In Fig. 6.10(c) and (d) the black line serves as a guide to the eye at $V_{SD} = 240$ μeV, corresponding to the bulk superconducting gap of Al [206, 218]. Here, we estimate a charging energy $E_C \approx 100 \pm 20$ μeV. Note, that the estimation of the charging energy and the lever arms becomes difficult for such low charging energies, as there are no sharp borders of the Coulomb blockade diamonds. If we assume the same induced superconducting gap Δ^* as above, then $E_C/2 < \Delta^*$ for Fig. 6.10(c). However, the applied gate voltages are much more positive, which would locate the electron wavefunction further away from the superconductor and reduce the coupling. From this logic, we should assume that the induced superconducting gap is smaller and it is unclear if $E_C/2 < \Delta^*$. Clearly, there is no 2e-periodicity or even-odd effects in E_C visible when comparing to the data in the normal state at finite magnetic field. We therefore have to assume that our superconducting island is too poisoned to observe 2e-periodicity due to bad coupling to the superconductor or the induced superconducting gap is too small.

The features looking similar to gate jumps (blue arrows) in Figs. 6.10(c) and d) are reproducible. They occur due to charging of the SCBs, as discussed previously. Note, the reduction in visibility in Fig. 6.10(d) compared to Fig. 6.10(c), due to the halving of the discrete charges loaded onto the SCBs. From our previous analysis we would also expect a doubling of the number of jumps as the Cooper pair island becomes normal conducting and charged by electrons with a 1e-periodicity. However, due to the small jumps this is difficult to resolve.

To improve the device quality, we fabricated a new device to remove the features of the SCBs but keep the advantage of the close SGs. The general device structure is similar to the device shown in Fig. 6.1(a), however to guarantee a good contact to the Al SGs, a 9 nm thin layer of gold was evaporated before the Al SG. The thin layer of gold acts as a bridge to the leads connecting them to the bond pads. As gold does not oxidize under normal condition, the contact resistance should be low. Furthermore, the Ar-milling time was increased in order to establish better contact to the Al and the overlap area was increased. At room temperature the resistance between two leads going to the same Al pad were found to be below 300 Ω. Accounting for resistances of the probe setup, we can assume that for this sample a good metallic contact to the Al SG is present. Additionally, the leads were made from Ti/Al to act as a quasiparticle trap for the Al-island. To further improve the interface between the Al-island and the NW a 1 nm thin sticking layer of Ti was evaporated before the Al deposition. As expected from the room-temperature characterization the device showed no sign of SCBs in the gate-gate maps. And only a single QD was observed. We can conclude that the bad contact problem to the SGs has been solved.

Figure 6.11(a) and (b) show Coulomb diamonds measured on this device as a function of V_{BG} and with $V_{Al} = 0$. As seen in the previous device, applying a magnetic field and destroying superconductivity in Al does not change the periodicity of the Coulomb resonances. Unlike the previous device, there are no clear features to associate with a superconducting gap edge. However, some signatures of superconductivity, such as a general decrease in current

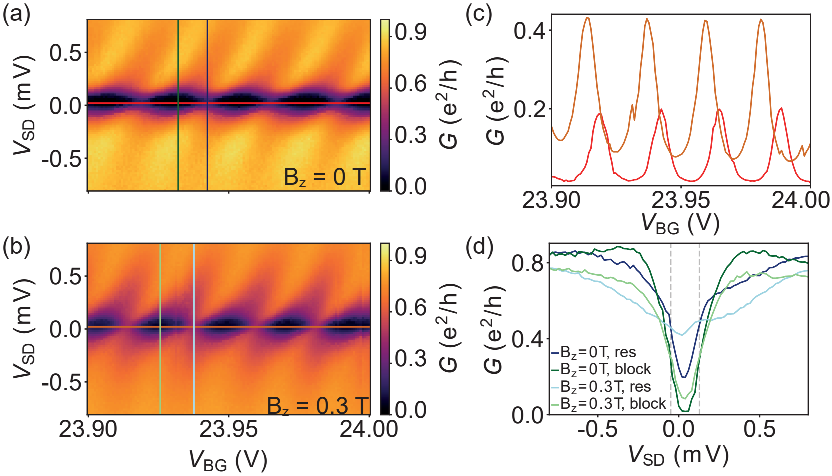

Figure 6.11. Coulomb blockade diamonds of a superconducting island. (a) and (b) Conductance $G = dI/dV$ as a function of the back gate V_{BG} and bias voltage V_{SD} with $V_{Al} = 0$, $B_Z = 0$ (a) and $B_Z = 0.3$ T (b). The colored lines correspond to line traces in (c), (d) with the corresponding colors. c) Conductance at $V_{SD} = 0$ as a function of V_{BG} for (a) (red) and (b) (brown). (d) Conductance on resonance (blue) and in blockade (green) in dependence of V_{SD} for (a) (dark green, dark blue) and (b) (light green, light blue).

is seen. Specifically, we observe a suppression in current in the device at $B_Z = 0.3$ T above the charging energy compared to zero magnetic field in the superconducting state. However, at $|eV_{SD}| < E_C$ the conductance is decreased at $B_Z = 0$, compared to $B_Z = 0.3$ T. This is shown in Fig. 6.11(c) with a cross section at $V_{SD} = 0$ for both Figs. 6.11(a) (red) and (b) (brown). Both the absolute conductance and relative height of the Coulomb blockade resonances is increased at finite magnetic field.

Similarly, Fig. 6.11(d) shows the conductance as a function of V_{SD} for constant V_{BG} taken at positions corresponding to Coulomb blockade (green lines) and on resonance (blue lines). As already seen in Figs. 6.11(a) and (b) the conductance at large V_{SD} decreases at finite magnetic fields and for small V_{SD} the conductance is increased. However, no clear sign of superconductivity is observed compared to the previous devices.

In conclusion this device shows no change from $2e$ to $1e$ periodicity, when going from the superconducting to the normal state, but resolves the "jumps" from the badly contacted SGs. Furthermore, unlike the previous device we observe no clear superconducting gap either. We observe some differences in conductance at zero and finite magnetic field, however we cannot definitely attribute those to superconductivity. We speculate that at positive V_{BG}, transport is dominated by the electrons accumulated at the bottom of the NW. As these modes are further away from the superconductor on top of the NW, they are less strongly proximitized. Alternatively, it is possible that adding the 1 nm Ti sticking layer negatively influenced the induced superconductivity with such a thin Al layer. However, Ti is also a superconductor by itself below 300 mK [219] and therefore unlikely to destroy it. However, its addition might worsen the interface between Al and the InAs NW, which in turn could weaken the induced superconductivity. Furthermore, the effects we observed at the gap edge in previous devices were due to quasiparticle poisoning from the leads. As the leads are supercondcuting themself now, such effects should lessen. However, the superconducting leads could also hinder us. It has been shown that single Cooper pair transistors are poisoned and 1e-periodic if Δ^* of the outer leads is larger than Δ^* of the island [220]. If the proximity gap is indeed so small, this might also be the case for us, although it does not explain why we didn't observe 2e-periodicity for the island with normal leads.

6.4. Summary and outlook

We have fabricated and measured several different Cooper pair island devices, where a $\sim 1\ \mu$m long QD was proximitized by a thin cold-evaporated layer of Al. By taking advantage of the 60 to 80 nm thick NWs the Al on top of the NW breaks-off from the Al evaporated on the substrate. This allows to selectively coat only the NW top-surface with Al, while also creating large Al pads to use as extremely close SGs. We have shown large lever arms on these SGs of up to 0.53 eV/V if both SGs are used simultaneously.

A bad contact interface between the Al SG pads and the connecting contact leads, due to insufficient removal of the native oxide, lead to the formation of QDs in the SGs. We have taken advantage of the extremely close NW to use it as a charge detector for the SCBs. We observe 2e-periodicity typical of a Cooper pair island, as well as half the capacitive shift at finite field in the charge boxes. From this we conclude that our SCBs form proper Cooper pair island. We then use the NW QD to detect the tunneling of a single Cooper pair in the SCBs and observe different tunnel rates between the two QDs. Note, that with small adjustments to the fabrication and device design, the SCBs should also be usable as charge detector. This could potentially be used to have a very strongly coupled charge detector to the NW.

For the NW QD however, no sign of a Cooper pair island could be found in several devices. We have observed charging energies E_C below the usual values of the induced superconducting gap Δ^* without any signature of a Cooper pair island. To reach such low charging energies however, the device needs to be strongly positively gated. At around zero gate voltages, the charging energies are above Δ^*. We speculate that these large positive gate voltages might have a negative influence on our induced superconductivity as transport would happen preferentially at the bottom of the NW, closer to the gate but further from the superconductor.

Everything leads to the question, why can we not measure a Cooper pair island in the NW? We have clearly demonstrated that the Al itself forms a Cooper pair island when not in contact with the NW. The prerequisite, that $E_C/2 < \Delta^*$ is fulfilled. In the previous chapter we have shown that we do indeed induce superconductivity in the NW. Given all these arguments, we are left to conclude that our superconducting island is either too strongly poisoned by quasiparticles, or still hosts NW modes not coupled to the superconductor. As to their origin, the fact that we did not observe any improvement by replacing the normal contacts with Al, suggests that the origin of the quasiparticle poisoning lies in insuffiecient proximitization of all the transport modes of the NW. If the quasiparticles were originating in the leads and tunneling into the superconducting island due to weak tunnel barriers, then proximitizing the leads should prohibit or at least reduce this effect. But this is not our observation, if anything adding superconducting leads to the device seems to decrease the signatures of superconductivity. This leads us to conclude that the most likely reason for our strong poisoning lies by not proximitized transport the NW. So far, hard superconducting gaps and 2e-periodicity have only been shown in thinner InAs NWs with Al epitaxially grown clean interface due to in-situ MBE growth [29, 33, 43, 193, 204]. For InSb nanowires a similarly epitaxial interface has been achieved by radical hydrogen-cleaning before deposition [194, 215]. Furthermore, our NWs are thicker than conventional wurtzite InAs NWs and we have already shown in chapter 5 that we observe many modes in transport. Unfortunately, the method of radical hydrogen-cleaning is not available to us and so far it has not been possible to grow these types of NWs with built-in barriers with an epitaxial Al shell. A possibility to further study whether a bad interface to the superconductor or too many-modes are the problem, similar studies could be done with thinner NWs with built-in barriers and a evaporated superconductor.

Given that the so-far successful methods of achieving a hard gap and an unpoisoned Cooper pair island in InAs NWs [33, 43, 215] are not available to us at the moment, using these NWs to study superconducting effects such as Majorana fermions and topological superconductivity does not seem like a fruitful approach. Instead we will now take advantage of another property of our NWs, the very nice and well-defined QDs and tunnel barriers. We have already shown that the tunnel barriers are robust to gating effects and allow for a large range of tunnel rates. Furthermore, their built-in approach allows to tailor the QDs to specific problems and reduces extra complications in the device design like pinch-off gates. In addition, the number of serial QDs can be adjusted as needed during growth. Therefore, we will now switch topics to study qubits in double QDs in the following two chapters 7 and 8.

7 Dispersive sensing of a double qunatum dot

The previous chapters have shown, that with our current possibilities our NWs are not ideal platforms for expirements based on induced superconductivity. Therefore, we will now leave out superconductivity and focus on experiments which potentially profit from well-defined QDs.

In the past, QDs and especially DQDS have proven themselves as a promising platform for both charge [73, 221, 222] and spin qubits [72, 98, 124, 167, 223]. At the same time cirquit quantum electrodynamics, originally pioneered by superconducting qubits [63–65], offers the possibility to couple qubits over large distances [67] and high-fidelity non-demolition read-out [66]. We will combine both of these system using our NWs with crystal-phase defined DQDs and coupling them to a high-impedance superconducting resonator. The inbuilt QDs remove the needs for pinch-off gates, which negatively affect the resonator quality due to cross-capacitances. Additionally, they offer us a high yield of well-working devices, which is a big advantage if only one device can be coupled to a resonator and cooled down in the dilution refrigerator at once. Furthermore, as discussed in chapter 4 InAs NWs have an intrinsic strong spin-orbit interaction. This enables spin manipulation and read-out while streamlining the device architecture due to removing external sources of charge-to-spin coupling, such as micromagnets [71, 74, 75, 224].

In this chapter, we will demonstrate coupling of a high impedance resonator to the charge degree of freedom in a DQD in an InAs nanowire. We will estimate the charge-photon coupling strength and linewidth of the charge state. This chapter is part of a collaborative work with J.H. Ungerer and the same analysis and similar figures can be found in his thesis [151].

7.1. The resonator-nanowire hybrid device

A schematic of the device under test is shown in Fig. 7.1. We couple a high-impedance NbTiN coplanar transmission line resonator to a zincblende InAs NW (green) with a crystal-phase defined DQD (red: barriers). Each of the QDs has a size of about ~ 300 nm. The occupation of the DQD is controlled with the SGs V_R and V_L. Gate V_M is connected but generally left at constant voltage, often at $V_M = 0$. The NW lies on a 20 nm thick hafnium dioxide (HfO_2) layer which insulates the device from the intrinsic Si substrate. The

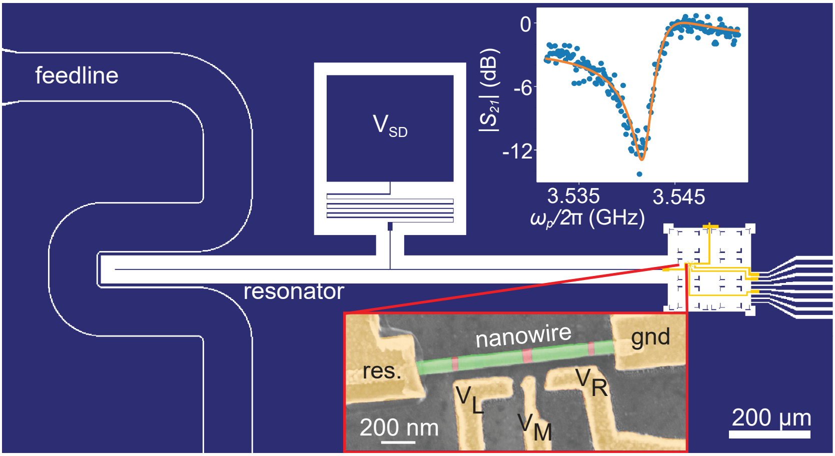

Figure 7.1. Device schematic and bare resonator curve. Design of the resonator etch-mask on NbTiN film (blue) and (bottom inset) false-colored SEM image of the device. The NW (green) with crystal-phase defined tunnel barriers (red) is coupled to the resonator through a contact. Top inset: Bare resonator transmission $|S_{21}|$ in dependence of the probe frequency ω_p. The orange line is a circular fit to the data [225]. Adapted from J. H. Ungerer [151].

device is galvanically connected to the NbTiN ground plane with one of the contacts. The other contact is coupled to the right voltage anti-node of the resonator. So the NW can be voltage biased through the resonator with voltage V_{SD} applied to the bias tap at the node of $\lambda/2$ mode of the resonator.

The resonator, made from a high-impedance NbTiN film (blue), is grown directly on Si after an HF cleaning step to remove the native oxide. The resonator is capcitively coupled to a feedline and the transmission through the feedline is measured. In the community, people refer this type of resonator to a notch-type resonator. The bare resonator curve is shown in the top inset of Fig. 7.1. Using a circular fit to the data, we extract a bare resonance frequency of $\omega_0/2\pi = 3.543$ GHz and a bare linewidth of $\kappa/2\pi \approx 10$ MHz. More details on the resonator fabrication and resonators in general can be found in the thesis of J. H. Ungerer [151].

7.2. Dispersive read-out

To dispersively measure our device with the resonator, we fix the frequency of the probe signal close to the bare resonance frequency, at the point of maximum slope of the magnitude or phase. In Fig. 7.2 we measure both the DC current through the device (a) and the resonator response S_{21} (b) simultaneously while changing the SG voltages V_R and V_L at a constant source-drain bias $V_{SD} = 100\ \mu$V.Both measurements outline a typical DQD charge stability diagram.

However, it is also obvious that the resonator senses different physical quantities than the current. The typical bias triangles are visible in both figures, however they are more pronounced in the current measurement, where they are the only visible feature. In the resonator response we also detect inter-dot transitions and dot-to-lead transitions where QD levels are aligned to each other or to the Fermi levels in the leads. This difference can be explained by the fact, that for the DC measurement only net-currents from source to drain can be measured. Hence, the DC measurement is not sensitive to tunneling processes which do not create a net-current. Only when all the electrochemical potentials align such that transport through the whole device is possible, a current can be measured [81]. In contrast the resonator has a dipole coupling to the charges tunneling in the DQD [226]. Therefore, no net-current is necessary to detect with a resonator and the single charging lines are visible.

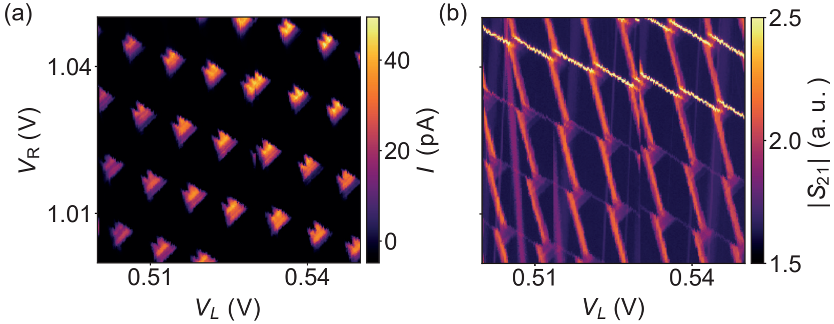

Figure 7.2. Charge stability diagram. (a) Measured current in dependence of SG voltages V_L and V_R at a source-drain bias $V_{SD} = 100\ \mu$V and $V_M = 2$ V. The typical bias triangles are observed. (b) The same measurement, but showing the magnitude of the resonator response $|S_{21}|$.

Additionally, we also observe some features on top of the honey-comb pattern. In Fig. 7.2b) they present as faint vertical lines, but they can also show in different forms. As they do not interact with the DQD system, we attribute them to the substrate or the measurement setup. A possible explanation would be some charged impurities on the substrate that interact with the resonator and the gates. We usually try to do detailed measurements in absence of those spurious features.

As mentioned already in chapter 4 we extract lever arm $\alpha_{L,1} = 0.22$ for the left gate on QD1 and $\alpha_{R,2} = 0.14$ for the right gate on QD2, and cross-lever arms $\alpha_{L,2} = 0.06$ and $\alpha_{R,1} = 0.03$. Thus we have little cross coupling.

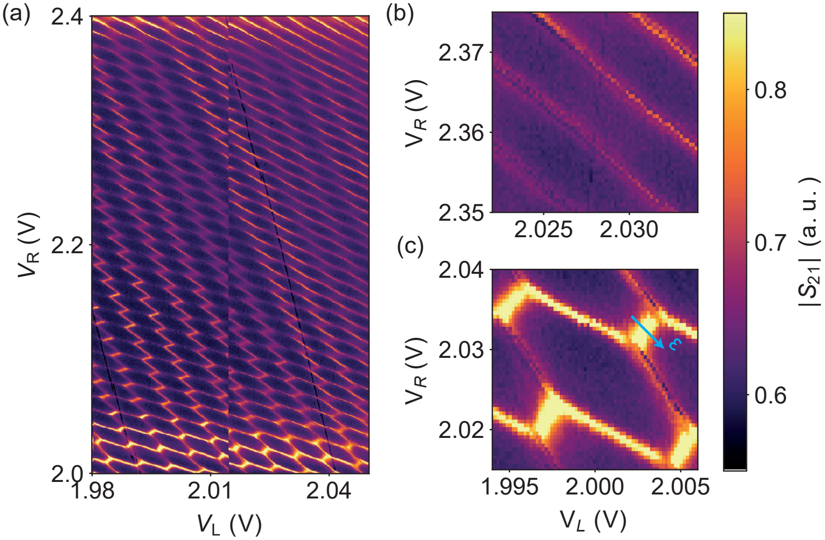

Figure 7.3. Dispserive read-out. Resonator reflection $|S_{21}|$ as a function of the SG voltages V_L and V_R. The evolution from a clear DQD (c) to a single QD (b) is seen. (b) and (c) are digital zoom-ins of (a).

One big advantage of using resonator read-out compared to current measurement or charge detection is the speed at which measurments can be done. Figure 7.3 shows the reflection $|S_{21}|$ in dependence of the two SGs V_L and V_R, (b) and (c) show digital zoom-ins into the map. This measurement serves to illustrate two points; first, the time advantage that can be gained by dispersive resonator read-out, and, second, the tunability of our DQD system.

To the first point, this measurement took a bit less than 6 hours to complete with 401 x 801 data points measured, illustrated the zoom-ins in (b) and (c) which show high resolution. It was measured with a bandwith of 100 HZ, corresponding to a measurement rate of one data point per 10 ms. In chapter 6 we have shown that our minimal measurement time with a standard voltmeter is about $\sim$ 35 ms. However, note that measuring at this rate significantly reduces our singal-to-noise ratio and is not advised standard procedure.

For standard lock-in measurements, we normally integrate at least for 100 ms. It is obivous that we are easily 3−10 times faster in dispersive RF-measurements without pushing the limits of the setup. For the second point, the measurement shows that we can tune our DQD from a clearly tunnel-coupled DQD with a characteristic honeycomb charge stability diagram [62, 77, 81] to a single QD [62, 77, 227], where the tunneling between the two QDs is so strong, that the electron wavefunction becomes strongly delocalized over both QDs. We note, that for our system the tunnel barriers are quite stable to gating, using a negative gate voltage V_M to decrease the tunnel coupling has not shown much effect. It has shown to be more promising to fill or deplete the DQD with gate voltages V_R and V_L in order to change the inter-dot tunnel rate. We assume filling or depleting changes the orbital wavefunction of the DQD, which can influence the inter-dot tunnel rate. Hence, it is easier for us to increase the tunnel rates until the DQD becomes a single QD than decreasing the tunnel rates. However, this limited tunability could be mitigated by growing the NWs with a desired tunnel rate. Future investigation into NWs with longer tunnel barriers are planned.

7.3. Charge qubit

We will now study the charge two-level system created at the inter-dot transition. As previously explained in chapter 2, finite tunnel coupling lifts the degeneracy of dot states at the inter-dot transition, forming a two-level system. We will refer to this as a charge qubit in this chapter. To investigate this, we focus on an inter-dot transition and observe the change in the resonator behavior, while we move along the detuning line through the transition, as is illustrated by the blue arrow in Fig. 7.3(c).

We study the resonator interaction with the charge qubit by varying the probe frequency ω_p while moving along the detuning axis ϵ (see Fig. 7.3(c)) through the inter-dot transition. While doing so we keep the average number of photons in the resonator $n_{ph} \ll 1$ and measure at a bandwidth of 10 Hz. The result is shown in Fig. 7.4(a). We observe two changes in the resonator response. The resonance frequency shifts lower and the linewidth of the resonator increases. This is visible in Fig. 7.4(b), where two line-cuts of Fig. 7.4(a) at a detuning $\epsilon = 46$ GHz (blue) and $\epsilon = 3$ GHz (red) are plotted. To quantify the resonator response as a function of ϵ we perform a circular fit of S_{21} [225] to the data, as illustrated in Fig. 7.4(b). From the fit we extract the resonance frequency ω_r and resonance linewidth δ_ω, which are shown in Fig. 7.4(c) and Fig. 7.4(d) respectively. As we observe a shift of the resonance frequency and no anti-crossing between resonator and two-level system, we de-

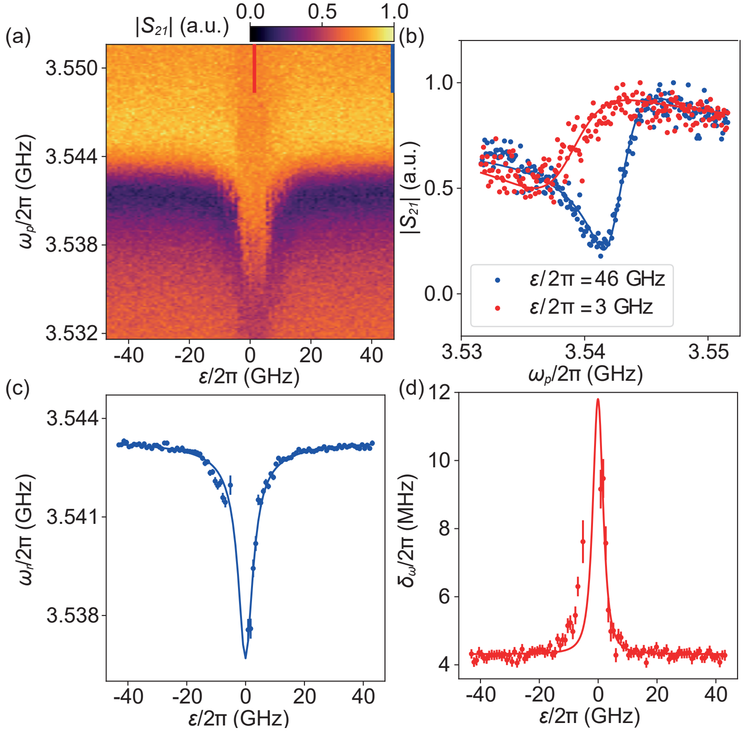

Figure 7.4. Dispersive sensing. (a) Reflection amplitude $|S_{21}|$ in dependence of resonator probe frequency ω_p and detuning ϵ of an inter-dot transition. b) Two line cuts of (a) at detuning $\epsilon = 46$ GHz (blue) and $\epsilon = 3$ GHz (red). A clear shift of both the resonance position and broadening of the linewidth is visible. The solid lines are circular fits [225] of S_{21} to the data. c) Extracted resonance frequencies ω_p from the fits in (b) for all traces in (a), where fitting was possible. (d) Extracted dressed resonator linewidth from the fits in (b). Solid lines in (c) and (d) are fits to the data using equations 7.1 and 7.2, respectively [64]. Figure adapted from J. H. Ungerer [151].

termine that we are operating in the dispersive regime, i.e the qubit frequency is larger than the resonator frequency $\omega_q = \sqrt{(2t)^2 + \epsilon^2} > \omega_0$, where t is the tunnel coupling between the two QDs [64, 65, 81].

The interaction between the charge qubit and the resonator can be described by the Jaynes-Cummings model [228]. Hereby, the energy of the dressed states

$\omega_{\psi\pm}$ is given by [64]

$$\omega_{\psi\pm} = \frac{\omega_0 + \omega_q}{2} \pm \frac{1}{2}\sqrt{4g^2 + (\omega_0 - \omega_q)^2}, \tag{7.1}$$

where $g = g_0 \cdot 2t/\omega_q(\epsilon)$ describes the effective charge-photon coupling strength accounting for the mixing angle at finite detuning. The resonator is sensitive to the ground state transition to the first excited state $|\psi_-\rangle$. The dressed resonator linewidth is then

$$\delta_\omega = |\langle\psi_-|g,1\rangle|^2\kappa + |\langle\psi_-|e,0\rangle|^2 2\gamma = \cos^2(\theta)\kappa + \sin^2(\theta)2\gamma, \tag{7.2}$$

where κ is the bare resonator linewidth and γ is the qubit linewidth and the mixing angle $\theta = \frac{1}{2}\tan^{-1}(\frac{2g}{\omega_q - \omega_0})$ [64].

We can now fit equations 7.1 and 7.2 to the extracted resonance frequencies and linewidths of several inter-dot transitions including the one shown in Fig. 7.4(c) and (d). We can extract the charge-photon coupling g_0 and inter-dot tunnel rate t. Using these values as parameters for equation 7.2, we extract the qubit linewidth γ. The results are shown in Fig. 7.5, where we plot

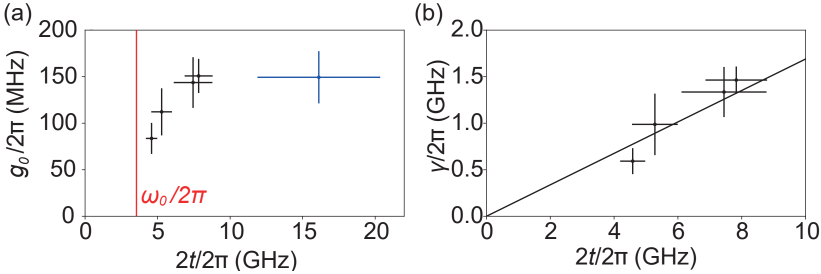

Figure 7.5. Extracted charge-photon coupling, qubit linewidth, and tunnel rate. (a) Extracted charge-photon coupling as a function of the inter-dot tunnel rate for five different inter-dot transitions. The red line denotes the bare resonator frequency $\omega_0/2\pi$. (b) Extracted qubit linewidth as a function of the tunnel rate for the same inter-dot transitions as in (a). The black line is a linear fit with slope $m = 0.17 \pm 0.02$. Adapted from J. Ungerer [151]

g_0 and γ as a function of t for five inter-dot transitions. For the charge-photon coupling Fig. 7.5(a) we observe no clear trend. In contrast for γ in Fig. 7.5(b) we observe a linear dependence on the t. For the inter-dot transition with largest t (blue point in Fig. 7.5(a), no broadening of the dressed resonator is observed and therefore no corresponding γ could be determined. Consequently, the data point is missing in Fig. 7.5(b). We observe qubit linewidths of about $\gamma \sim 1$ GHz, which indicates a large charge qubit decoherence. Similarly large γ's have been observed in NW DQDs [229, 230]. We speculate that oxides at the NW surface combined with large surface to volume ratio induce large charge noise.

7.4. The strongly dispersive regime and the Bloch-Siegert shift

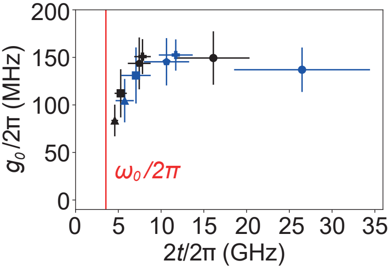

Figure 7.6. Jaynes-Cummings model vs Block-Siegert shift. Extracted charge-photon couplings g_0 as a function of extracted tunnel rate $2t$ using the Jaynes-Cummings model (black) and including the Block-Siegert shifts (blue). Shared symbols on the data points denote the same inter-dot transition. Figure adapted from J. H. Ungerer [151].

So far, we have analyzed our data using the Jaynes-Cummings Hamiltonian. However, the Jaynes-Cummings Hamiltonian makes use of the rotating-wave approximation, neglecting the counter-rotating term. In the very open regime, where the tunnel rates t and resulting qubit frequency ω_q are much larger than the resonator frequency ω_0, the counter-rotating terms start to matter. By including them the dressed resonator frequency in equation 2.32 can be rewritten as [65, 231]

$$\omega_{\Psi_\pm} = \omega_0 \pm \left(\frac{g^2}{\omega_q - \omega_0} + \frac{g^2}{\omega_q + \omega_0} \right), \tag{7.3}$$

where the term $g^2/(\omega_q - \omega_r)$ is called Lamb-shift and $g^2/(\omega_q + \omega_r)$ the Block-Siegert shift. We now repeat the analysis done for Fig. 7.5 with equation 7.3. The comparison between the two analyses is shown in Fig. 7.6. We note, that the extracted g_0 are similar in both models, however the extracted tunnel rates increasingly differ the more dispersive the system is.

7.5. Crossing of the charge qubit

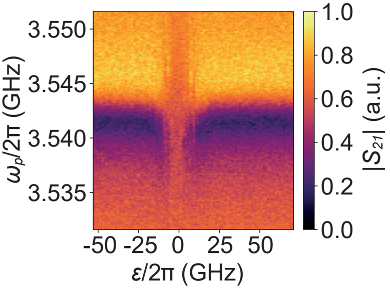

Figure 7.7. Crossing of resonator and qubit frequency. a) Resonator reflection amplitude $|S_{21}|$ in dependence of resonator probe frequency ω_p and detuning ϵ of an inter-dot transition, where the qubit frequency ω_q is below the resonator frequncy ω_0. The resonance is completely smeared out and not resolvable anymore due to the large qubit linewidth γ. Figure adapted from J. H. Ungerer [151].

While the most inter-dot transitions are largely detuned from the resonator frequency, we can find a few inter-dot transitions where the tunnel rate is similar to the resonator frequency. By varying ϵ the qubit frequeny $\omega_q = \sqrt{(2t)^2 + \epsilon^2)}$ can become resonant with the resonator frequency. The resonator response of such a inter-dot transition is shown in Fig. 7.7. In the following we show that at low detuning, the linewidth of the resonance is dominated by the qubit linewidth and the resonator response cannot be resolved anymore.

We can explain the much worse dressed resonator quality compared to the dispersive regime by looking at equation 7.2. As ω_q approaches ω_0 the dressed linewidth will approach $\delta_\omega \to \frac{1}{2}\kappa + \gamma$. Given our above extracted values for $\kappa \sim 10$ MHz and $\gamma \sim 1$ GHz, it follow that $\kappa \ll \gamma$. This means that, assuming constant qubit linewidth γ, the closer our qubit frequency ω_q is to our resonator frequency ω_0, the larger our dressed linewidth δ_ω becomes. Above we extract $\gamma \sim 0.5$ to 1 GHz. This large qubit linewidth ultimately makes it impossible to properly resolve the qubit in the resonant regime.

7.6. Summary and Outlook

We have successfully coupled an InAs NW DQD to a high-impedance resonator. Using the resonator we performed dispersive read-out on the DQD.

We have shown some of the advantages of resonator read-out over conventional low-frequency transport measurements, such as faster data acquisition and sensitivity to the quantum capacitance of the system instead of electrical current.

Furthermore, we used the resonator to probe the two-level system of our DQD at the inter-dot transition. We observe a dispersive shift of the resonance frequency. By using the Jaynes-Cummings model we could extract charge-photon coupling g from 70 to 150 MHz and a qubit linewidth of about ~ 1 GHz. The large qubit linewidth γ makes it impossible for us to resolve an anti-crossing in the resonant regime, when $\omega_q = \omega_0$.

We speculate that the large qubit linewidth is due to charge noise of the InAs NW and the substrate. While improving the charge noise of the InAs NW without changing the material and loosing our in-built DQDs is very difficult, we can improve on the substrate quality. For this device we sputtered the resonator on bare undoped silicone to maximize the resonator quality. However, this required an ALD grown oxide layer to insulate the NW from the substrate. Unfortunately, our ALD oxide quality is not great and creating a large number of gate jumps. As a consequence, the device was not stable enough to stay on a charge transition long enough to perform magnetic field measurements reasonably. Therefore, we decided to get rid of the ALD oxide on future devices and instead sputter the resonator on global thermally grown SiO_2 layer. While the oxide decreases the resonator quality, its effect is negligible as the quality factor of a high-impedance resonator is already limited by the coupling to the NW and losses through the gates [232, 233]. For more information about the resonators and the influences of the different oxides, please refer to J.H. Ungerer's thesis [151] and Ref. [234].

In conclusion, while the linewidth of our charge qubit is far from ideal, we still think that the advantages the in-built DQDs and high device yield offer justify further investigation of this type of devices. We hope to limit our charge noise and increase the stability of devices by optimizing substrate oxides. Furthermore, if our large linewidth is indeed due to charge noise, moving from charge to spin qubits might significantly improve it, as charge noise can be reduced in spin qubits. [235–237].

8 Strong coupling between a microwave photon and a singlet-triplet qubit

In chapter 7 we suffered from poor oxide quality used to insulate the device from intrinsic Si. In this device we removed all atomic layer deposition (ALD) oxides and replaced them with a 100 nm thermally grown SiO_2. This has shown a much better device quality. This increased device stability allows us to apply a magnetic field to the device and measure a novel singlet-triplet qubit mediated by the intrinsic spin-orbit interaction in zincblende InAs NWs [76, 166, 167]. The following chapter has been published in similar form in Nature Communications [238]. It is a work with equal collaboration with J.H. Ungerer and therefore also found in similar form in his thesis [151].

Strong coupling between a microwave photon and a singlet-triplet qubit

J. H. Ungerer,[1,2,*] A. Pally,[1,*] A. Kononov,[1] S. Lehmann,[3] J. Ridderbos,[1,†]
P. P. Potts,[1,2] C. Thelander,[3] K.A. Dick,[4] V.F. Maisi,[3], P. Scarlino,[5],
A. Baumgartner[1,2] and C. Schönenberger[1,2]
[1]Department of Physics, University of Basel, Klingelbergstrasse 82 CH-4056, Switzerland
[2]Swiss Nanoscience Institute, University of Basel, Klingelbergstrasse 82 CH-4056, Switzerland
[3] Solid State Physics and NanoLund, Lund University, Box 118, S-22100 Lund, Sweden
[4] Centre for Analysis and Synthesis, Lund University, Box 124, S-22100 Lund, Sweden
[5] Institute of Physics and Center for Quantum Science and Engineering, Ecole Polytechnique Fédérale de Lausanne, CH-1015 Lausanne, Switzerland
[*] Equal contributions
[†] Current address: MESA Institute for Nanotechnology, University of Twente, P.O. Box 217, 7500 AE Enschede, The Netherlands

Abstract

Tremendous progress in few-qubit quantum processing has been achieved lately using superconducting resonators coupled to gate voltage defined quantum dots. While the strong coupling regime has been demonstrated recently for odd charge parity flopping mode spin qubits, first attempts towards coupling a resonator to even charge parity singlet-triplet spin qubits have resulted only in weak spin-photon coupling strengths. Here, we integrate a zincblende InAs nanowire double quantum dot with strong spin-orbit interaction in a magnetic-field resilient, high-quality resonator. In contrast to conventional strategies, the quantum confinement is achieved using deterministically grown wurtzite tunnel barriers without resorting to electrical gating. Our experiments on even charge parity states and at large magnetic fields, allow to identify the relevant spin states and to measure the spin decoherence rates and spin-photon coupling strengths. Most importantly, we find an anti-crossing between the resonator mode in the single photon limit and a singlet-triplet qubit with an electron spin-photon coupling strength of $g/2\pi = 139 \pm 4$ MHz. Combined with the resonator decay rate $\kappa/2\pi = 19.8 \pm 0.2\,$MHz and the qubit dephasing rate $\gamma/2\pi = 116 \pm 7\,$MHz, our system achieves the strong coupling regime in which the coherent coupling exceeds qubit and resonator linewidth. These results pave the way towards large-scale quantum system based on singlet-triplet qubits.

8.1. Introduction

Spin qubits in semiconductors are promising candidates for scalable quantum information processing due to long coherence times and fast manipulation [102, 239–241]. For the qubit readout, circuit quantum electrodynamics based on superconducting resonators [242], allows a direct and fast measurement of qubit states and their dynamics [124]. Recently, resonators were used to achieve charge-photon [68, 243], spin-photon [70, 71, 123] as well as coherent coupling of distant charge [73] and spin qubits [74, 75], enabling coherent information exchange between distant qubits. However, the small electric and magnetic moments of individual electrons require complicated device architectures such as micromagnets, and a large number of surface gates that render scaling up to more complex architectures challenging. These approaches typically achieve a relatively weak electron spin-photon coupling on the order of $\sim 10 - 30\,\mathrm{MHz}$. In addition to single electron spin qubits, also spin qubits based on two electrons in a double quantum dot (DQD), e.g. in a singlet-triplet qubit have been demonstrated [244]. Spin qubits based on two electrons typically offer a large hybridization of the spin and charge degree of freedom compared to single-electron spin qubits in principle allowing even stronger coupling strengths. So far, however, the experimentally achieved coupling strengths in such systems [245, 246] remained well below the strong coupling limit in which the coherent coupling rate exceeds both, the cavity mode decay rate and the qubit linewidth.

Here, we demonstrate that the strong coupling regime between a singlet-triplet qubit and a single photon in a superconducting resonator can be reached. We achieve this strong coupling by carefully designing the resonator and by using a DQD defined by in-situ grown tunnel barriers in a semiconductor with a large spin-orbit interaction. The tunnel barriers consist of InAs segments in the wurtzite crystal-phase with an atomically sharp interface to the zincblende bulk of the nanowire (NW) [40]. These crystal-phase barriers are highly reproducible and render the need of barrier gates obsolete, simplifying integration with superconducting resonators and making the nanowires a viable prototype for scalable quantum computing architectures.

In this work, we make use of the large spin-orbit interaction in these nanowires [76] to define a singlet-triplet qubit at a finite in-plane magnetic field in which the $T^+_{1,1}$ and $S_{2,0}$ states hybridize, forming a quantum two-level system. Incorporating a NW with a magnetic-field resilient resonator based on NbTiN [234, 247] allows us to measure an avoided crossing between the singlet-triplet qubit and a single-photon excitation of the resonator at a magnetic-field strength of $B = 300\,\mathrm{mT}$. The measured coupling strength is very large compared to previously reported electron spin-photon coupling [70, 71, 123], which enables us to reach the strong coupling regime. In addition, by analyzing the response of the hybridized resonator-qubit system for varying magnetic-field strengths, we perform qubit spectroscopy [224, 243, 248]. This allows us to identify the specific spin states and to quantitatively extract the relevant device properties.

8.2. Device characterization

Details about the NW properties and their growth can be found in the supplementary. The resonator-qubit system of device A is shown in Fig. 8.1(a), including a false-colored SEM-image of the crystal-phase defined NW DQD. We report similar experiments for two devices, A and B, with B discussed in the SI material. They are measured in a dilution refrigerator with a base temperature of 70 mK. The DQD forms in the 490 nm and 370 nm long zincblende segments (green), separated by 30 nm long wurtzite (red) tunnel barriers with a conduction band offset of ∼100 meV [35], as illustrated in Fig. 8.1(b). A high-impedance, half-wave coplanar-waveguide resonator is capacitively coupled to the DQD at its voltage anti-node via a sidegate. In addition, the same sidegate can be used to tune the DQD charge states using a dc voltage (V_R) applied at the resonator voltage node. The DQD state is probed by reading out the resonator rf-transmission. We extract the bare resonance frequency of the resonator $\omega_0/2\pi = 5.1705 \pm 0.0003\,\mathrm{GHz}$ at zero magnetic field and the bare decay rate $\kappa|_{B=0}/2\pi = 27.3 \pm 0.6$ MHz. The resonator design and fitting are described in detail in methods section D.1 and 2.2.2.

In the following, we prepare the DQD in an even charge configuration in the many-electron regime (see methods D.5), described by a two-electron Hamiltonian given in methods section 2.1.6. Figure 8.1(c) shows the eigenvalues of this Hamiltonian as a function of external magnetic field B at a fixed DQD detuning. At zero magnetic field, the detuning renders the singlet $S_{2,0}$ the ground state, for which both electrons reside in the same dot. Without spin-rotating tunneling, this, and the $S_{1,1}$ state, with the electrons distributed to different dots, form a charge qubit [81]. The subscripts describe the dot electron occupation of the left and right dot, respectively. By applying an external magnetic field, the Zeeman effect lowers the energy of the triplet $T^+_{1,1}$ state, that becomes the ground state for sufficiently high magnetic fields. In the presence of a spin-rotating tunneling $t = \Delta_{\mathrm{SO}}/2$ induced by the intrinsic spin-orbit interaction Δ_{SO}, the energy levels of the hybridized $S_{2,0}$ and $T^+_{1,1}$ states are split. The two new eigenstates of the avoided crossing form a singlet-triplet qubit shown schematically in Figs. 8.1(a) and (b).

We now focus on one particular inter-dot transition (IDT) marked by a green rectangle in Fig. 8.2(a). The same IDT is shown in Fig. 8.2(b) and (c) at $B = 0$ T and $B = 300$ mT respectively, with $\alpha = 57°$. In Fig. 8.2(d) we show the normalized transmission $(A/A_0)^2$ at $B = 0$ T, while varying the probe frequency ω_p and relative detuning $\varepsilon_{\mathrm{rel}}$, illustrated by the white line in Fig. 8.2(b). An electron can now reside on either of the two tunnel-coupled dots, constituting a charge qubit. At the IDT, close to charge degeneracy, the electrical dipole moment of the charge qubit interacts with the resonator, resulting in a dispersive shift of the resonance frequency. By fitting input-output theory (see theory section 2.2.2) to this particular IDT, we

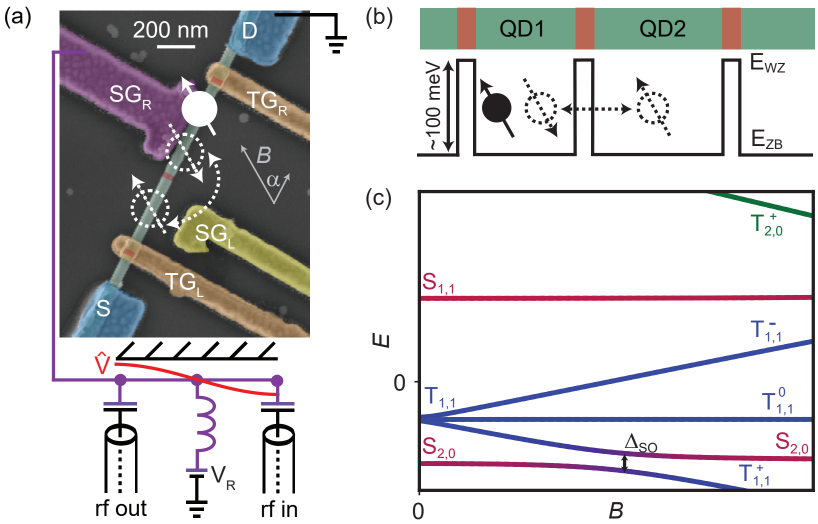

Figure 8.1. Coupled resonator-qubit system (a) False colored SEM-image of device A. The NW (green) is divided into two segments by an in-situ grown tunnel barrier (red), thus forming the DQD system. The NW ends are contacted by two Ti/Au contacts (S,D) and the NW segements can be electrically tuned by two Ti/Au sidegates SG_R (purple) and SG_L (yellow). A high-impedance, half-wave resonator is connected to SG_R. Top gates (orange) are kept at a constant voltage of -0.28 V. The magnetic field is applied in-plane at an angle α with respect to the NW axis, as illustrated by the grey arrow. The white arrows illustrate an even charge configuration with the two degenerate DQD states $T^+_{1,1}$ and $S_{2,0}$. (b) Schematic of the crystal-phase defined DQD. The conduction band of wurzite and zincblende are offset by ~ 100 meV, resulting in a tunnel barrier between the zincblende segments. The intrinsic spin-orbit interaction enables spin-rotating tunneling between these segments. (c) Energy levels of an even charge configuration as a function of magnetic field B at a fixed positive detuning ε between the dot levels. At finite magnetic fields, $T^+_{1,1}$ (blue) hybridizes with $S_{2,0}$ (red) defining a singlet-triplet qubit with an energy splitting given by the spin-orbit interaction strength Δ_{SO}.

Figure 8.2(a) shows the charge stability diagram of device A at a magnetic field of 600 mT with the angle $\alpha = 164°$ with respect to the NW axis (See Fig. 8.1(a)) detected as a shift in the transmission phase φ of the resonator, plotted as a function of the two gate voltages V_L and V_R at a fixed probe frequency of $\omega_p/2\pi = 5.174$ GHz, close to resonance. We observe a characteristic honeycomb pattern of the charge stability diagram of a DQD. Using a capacitance model [81, 222], we extract the gate-to-dot capacitances $C_{R2} = 44 \pm 2\,\mathrm{aF}$, $C_{L2} = 2.0 \pm 0.2\,\mathrm{aF}$, $C_{R1} = 5 \pm 2\,\mathrm{aF}$ and $C_{L1} = 4.6 \pm 0.2\,\mathrm{aF}$ for device A.

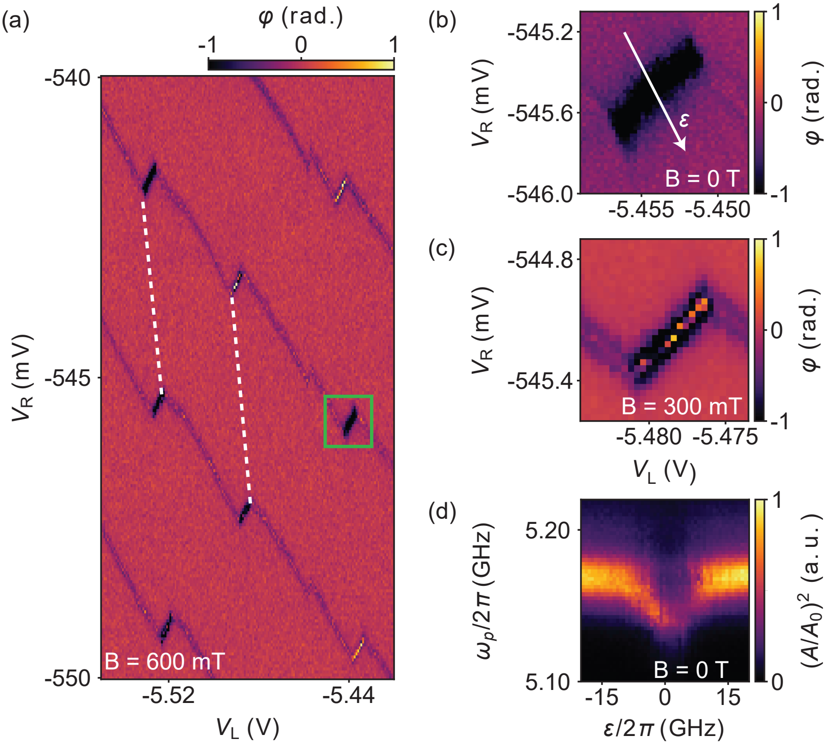

Figure 8.2. Dispersive sensing of the DQD at $B = 0$. (a) Charge stability diagram of the device at $B = 600$ mT applied at $\alpha = 164°$ with respect to the NW, in which the resonator phase φ is measured as a function of the SG voltages V_R and V_L. A zoom on the interdot transition pointed out by the green rectangle is shown in (b) and (c) at $B = 0$ T and $B = 300$ mT with $\alpha = 57°$, respectively. (d) Resonator transmission $(A/A_0)^2$ versus probe frequency ω_p and detuning ε (illustrated by the white line in (b)). At the charge degeneracy point of the DQD, we find a dispersive shift of 21 ± 2 MHz with respect to the bare resonance frequency. At small positive detuning a triplet state crosses the IDT, leading to a suppressed resonator transmission.

extract the inter-dot tunnel coupling $t|_{B=0}/2\pi = 5.1 \pm 1.0$ GHz, the charge-photon coupling $g_0|_{B=0}/2\pi = 353 \pm 72$ MHz, and the charge qubit linewidth $\gamma|_{B=0}/2\pi = 1.7 \pm 0.7$ GHz.

8.3. Strong spin-photon coupling

When investigating the magnetic-field dependence of IDTs similar to the ones shown in Fig. 8.2(b,c), we observe two qualitatively different behaviors which we identify as even and odd charge parity configurations described in methods section D.5. In the following, we investigate a single IDT, shown in Fig. 8.2(c), with an even charge parity.

As illustrated in Fig. 8.1(c), the DQD can be operated as a singlet-triplet qubit when applying a magnetic field. The qubit frequency ω_q can be brought into resonance with the cavity frequency ω_0 at $B \gtrsim 200\,\mathrm{mT}$, as discussed in more detail below. At the resonance condition ($\omega_q \sim \omega_0$), an anti-symmetric (bonding) and a symmetric (anti-bonding) qubit-photon superposition state are formed. The corresponding resonances can spectroscopically be discriminated only if the splitting $2g$ between them is larger than the dressed states' linewidth $\gamma + \kappa/2$ [65]. In particular, the hybrid system is considered strongly coupled if the qubit-photon coupling strength g exceeds γ and κ [65].

In Fig. 8.3(a), we plot a spectroscopic measurement of the resonator where the singlet-triplet qubit is tuned into resonance by applying an electrostatic detuning $\varepsilon_{\mathrm{rel}}$ relative to the configuration at which $S_{2,0}$ and $T^{+}_{1,1}$ would be fully degenerate in the absence of a a spin-rotating tunneling. Consistent with strong coupling, we observe an avoided crossing between the resonator and the qubit. At the points where the bare qubit frequency ω_q and resonator frequency ω_0 (dashed, white curves) are degenerate, instead of crossing, they anti-cross. And in Fig. 8.3(a), a faint double peak structure is visible at around $\varepsilon_{\mathrm{rel}} \sim 0$ as $2g > \kappa/2 + \gamma$, signature of the strong coupling regime [65].

For a quantitative analysis, we fit Lorentzians to the transmission of each trace of constant $\varepsilon_{\mathrm{rel}}$, we extract the transition frequencies $\omega_\pm$ of the dressed states. These are fitted to the Jaynes-Cummings model (solid, white curves in Fig. 8.3(a)) described in theory section 2.2.1. From this fit, we extract the tunnel rate $t|_{B=300\,\mathrm{mT}}/2\pi = \Delta_{\mathrm{so}}|_{B=300\,\mathrm{mT}}/4\pi = 2.54 \pm 0.03\,\mathrm{GHz}$ and bare spin-photon coupling strength $g_0^{\mathrm{JC}}|_{B=300\,\mathrm{mT}}/2\pi = 123 \pm 16$ MHz. The extracted tunnel rate allows to plot the qubit transition frequency $\omega_q = \sqrt{(\Delta_{\mathrm{so}}/\hbar)^2 + (\varepsilon_{\mathrm{rel}})^2}$ in Fig. 8.3(a) and to identify the resonance condition $\omega_q = \omega_0$ at a small electrostatic detuning $\varepsilon_{\mathrm{rel}}/2\pi = \pm 1.0\,\mathrm{GHz}$. We evaluate the effective coupling strength $g = g_0 \cdot 2t/\omega_q$ at the finite detuning $\varepsilon_{\mathrm{rel}}/2\pi = -1.0\,\mathrm{GHz}$ and obtain $g^{\mathrm{JC}}|_{\epsilon_{\mathrm{rel}}/2\pi=-1\,\mathrm{GHz},}/2\pi = 121 \pm 16$ MHz, as the spin-photon coupling strength on resonance condition.

In Fig. 8.3(b), we plot a line trace at this detuning value as indicated in

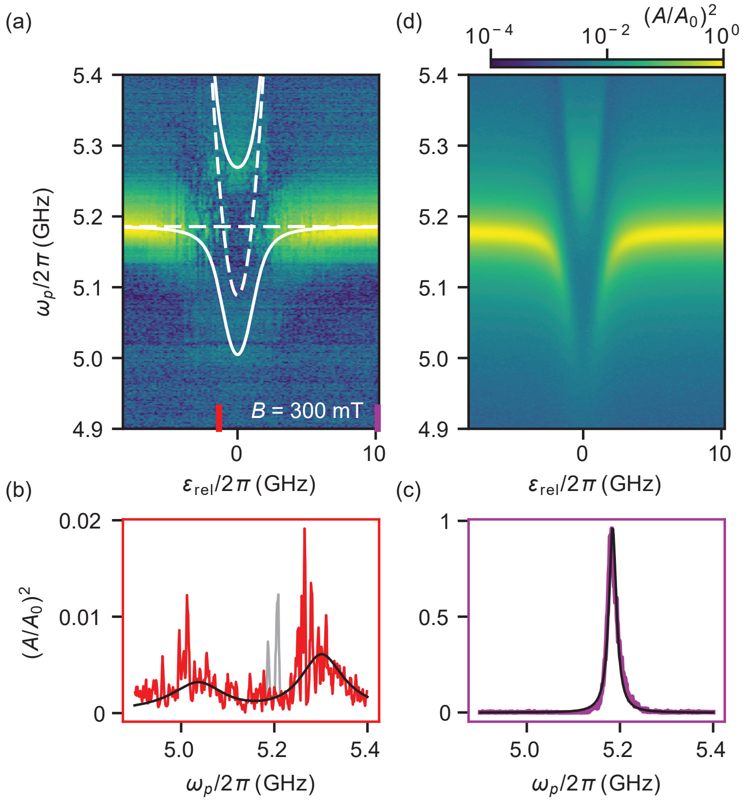

Figure 8.3. Strong spin-photon coupling. (a) Anti-crossing of the resonator and the qubit found when plotting the resonator transmission as a function of detuning $\varepsilon_{\rm rel}$ and probe frequency ω_p at a magnetic field of $B = 300\,\mathrm{mT}$ and $\alpha = 57°$. The solid white curves are the eigenstate energies from fits to a Jaynes-Cummings model (Eq. (2.32) in theory section 2.2.1). The faint double-peak structure at $\varepsilon \approx 0$ is an unambiguous signature of the strong coupling regime, $g > \kappa, \gamma$ [65]. (b,c) Cross sections at the detunings indicated by colored bars in (a). The solid lines stem from fit to input-output theory. (b) Double-peak structure at $\omega_q \sim \omega_0$ (see text). The larger noise floor for $\omega_p \sim \omega_0$ (grey data) is attributed to the bare resonator which is visible in spectroscopy because of a finite coupling between DQD and leads resulting in an odd DQD occupation for a short fraction of time during data acquisition. (c) Transmission for $\omega_q \gg \omega_0$, corresponding to the bare resonator. (d) Simulation using input-output theory with the parameters extracted from the input-output fit to (b). For these measurements, given the input-power $P_{\rm in} = -133\,\mathrm{dBm}$, the average number of photons is $n < 0.25$ (see theory section 2.2.2).

Fig. 8.3(a). Despite the large noise, the double peak structure is also clearly visible and stands in stark contrast to the bare resonator transmission at large detuning (see corresponding linetrace in Fig. 8.3(c)). Using Eq. (2.36) derived from input-output theory described in the supplementary, we fit these data at 300 mT and extract the spin-photon coupling strength $g_{\varepsilon_{\mathrm{rel}}=-1\,\mathrm{GHz}}/2\pi = 139 \pm 4\,\mathrm{MHz}$ and qubit dephasing $\gamma/2\pi = 116 \pm 7\,\mathrm{MHz}$ where we used the bare resonator decay $\kappa|_{B=300\mathrm{mT}}/2\pi = 19.8 \pm 0.6\,\mathrm{MHz}$. This value agrees well with the one obtained from the Jaynes-Cummings model. Using the values from input-output theory we model the whole anti-crossing using input-output theory in Fig. 8.3(d), observing a very good agreement with the measurement.

All together, this measurement therefore clearly demonstrates that the strong coupling regime between a single microwave photon and a singlet-triplet qubit is reached.

8.4. Magnetospectroscopy

To explicitly identify and characterize the spin-orbit eigenstates and to independently verify the character of the singlet-triplet qubit, we now study the magnetic field evolution of the IDT from 0 up to 900 mT applied at the angle $\alpha = 130°$. We measure the amplitude A and phase φ of the signal transmitted through the resonator as function of detuning ε and magnetic field strength B. A non-zero φ occurs at the IDT when tunneling between the dots is allowed resulting in a non-zero DQD dipole moment. As described in methods section 2.1.6, we model the DQD by an effective two electron Hamiltonian which allows us to fit the gate voltage and field dependence of the IDT (white dashed line in Fig. 8.4(a)). We find that the magneto-dispersion of the IDT is well described using the following fit parameters: the spin-conserving singlet and triplet tunnel rates $t_c^S/2\pi \approx 8.5\,\mathrm{GHz}$, and $t_c^T/2\pi \approx 3.2\,\mathrm{GHz}$, the singlet-triplet coupling rate $t_{\mathrm{SO}}/2\pi = \Delta_{\mathrm{SO}}/4\pi \approx 2.9\,\mathrm{GHz}$, the electron g-factors of the right and left dots, $g_R \approx 1$ and $g_L \approx 8$, as well as the single dot singlet-triplet energy splitting $\Delta_{\mathrm{ST}}/2\pi \approx 47\,\mathrm{GHz}$. These fit parameters are consistent with parameters obtained previously in this material system [61, 76, 166, 249, 250]. We note, however, that the fit is under-determined and therefore, it does not provide accurate numbers. Nonetheless, the model gives a qualitative, physical understanding of the system and allows us to establish which DQD levels interact with the resonator.

Independently, we gain quantitative information about the system by considering the functional dependence of the amplitude A and phase φ. This is possible because the resonator provides an absolute energy scale allowing for a quantitative analysis of the interaction between the DQD and the resonator and hence to perform qubit spectroscopy [224, 243, 248]. This spectroscopy complements the preceding DQD Hamiltonian fit. As described in methods

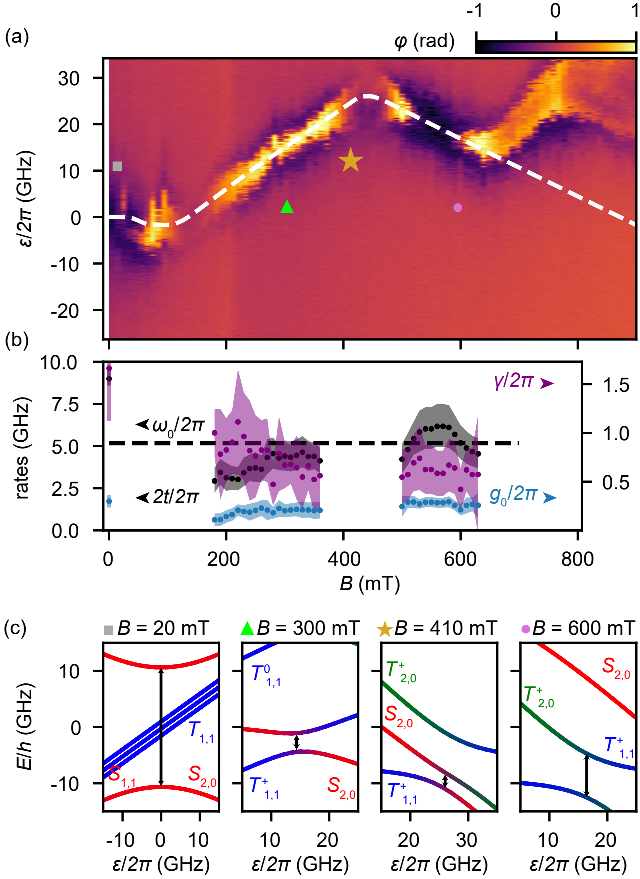

Figure 8.4. Magnetospectroscopy of the singlet-triplet qubit. a) Dispersive shift χ as a function of the magnetic field B at an angle of $\alpha = 130°$ and detuning ε. The white dashed line is a fit of the effective two-electron Hamiltonian (Eq. (2.1.6)) to the data. b) Extracted tunnel rate $2t/2\pi$ (black), qubit-photon coupling $g_0/2\pi$ (blue) and qubit linewidth $\gamma/2\pi$ (purple). The bare resonator frequency is indicated by the dashed black line. Shaded areas indicate the errorbars which originate from the uncertainty of the gate lever arm, which was independently measured. (c) Two-electron energy level diagrams at various magnetic fields with the corresponding field strength indicated in (a) and (b) by the given symbols. For clarity a constant offset of 10 GHz, 20 GHz, and 30 GHz was added to the energy levels at 300 mT, 410 mT and 600 mT. Given the input power $P_{\text{in}} = -128\,\text{dBm}$, the average photon number is $n < 0.8$ in these experiments (see methods section 2.2.2).

section 2.2.2, by fitting input-output theory to φ and A simultaneously, we extract the qubit tunnel amplitude t, the qubit linewidth γ, and the qubit-photon coupling strength g as a function of B, which we plot in Fig. 8.4(b). Here, we assume γ as constant in detuning ε.

Using the fits to both, the 2-electron Hamiltonian model and input-output theory in the 2-level approximation, allows us to directly identify several regimes, in each of which the qubit has a different spin-character. Fig. 8.4(c) shows the corresponding DQD level structure based on the fit parameters as a function of ε for different magnetic field.

At a low magnetic fields around $B = 20\,\mathrm{mT}$, the triplet states (blue curves) are Zeeman split and the ground-state curvature is dominated by the anti-crossing between $S_{1,1}$ and $S_{2,0}$ (red curves). We find a singlet charge qubit in the weak coupling limit, i.e. the linewidth exceeds the charge-photon coupling by a factor of five. The formation of an asymmetric double-dip structure in $\varphi(\varepsilon)$ between $B \sim 0.01\,\mathrm{T}$ and $B \sim 0.18\,\mathrm{T}$ is explained by an interaction between the three states $S_{2,0}$, $S_{1,1}$ and $T^+_{1,1}$ as described in the supplementary material. Traces of $\varphi(\varepsilon)$ with anasymmetric double-dip structure cannot be described by a two-level input-output model and are therefore not analysed quantitatively here. At $B \approx 50\,\mathrm{mT}$, φ becomes positive. Which we interpreted as a drop of the tunnel rate below the resonator frequency, $2t < \omega_0$

As B is increased, the triplet state $T^+_{1,1}$ becomes the ground state for $\varepsilon < 0$, as shown in the second panel of Fig. 8.4(c) for $B = 300\,\mathrm{mT}$. The spin-orbit interaction couples the singlet and triplet states, leading to an anti-crossing between $S_{2,0}$ and $T^+_{1,1}$, which constitutes a singlet-triplet qubit with $\omega_q = \Delta_{\mathrm{SO}} = 2t_{\mathrm{SO}}$ [82, 98]. In this regime, at larger B, the resonance condition between $S_{2,0}$ and $T^+_{1,1}$ occurs at larger ε, because the energy of the bare $T^+_{1,1}$ state decreases with larger B and the energy of $S_{2,0}$ decreases with larger ε. Therefore, the IDT is observed at larger ε for increasing B.

Consistent with the interpretation of the formation of a singlet-triplet qubit, we measure an approximately constant tunneling rate t between $B \sim 0.18\,\mathrm{T}$ and $B \sim 0.36\,\mathrm{T}$. In this regime, we extract the average spin-orbit tunneling rate to be $\bar{t}_{\mathrm{so}} = 1.94 \pm 0.02\,\mathrm{GHz}$.

At a magnetic field of $B \approx 370\,\mathrm{mT}$, the resonator phase φ starts to vanish due to the the triplet state $T^+_{2,0}$ becoming relevant. The triplet state results in a level repulsion between $T^+_{2,0}$ and $T^+_{1,1}$ and hence leads to a reduced energy gap between the $S_{2,0}$ level and the $T^+_{1,1}$ level. In Fig. 8.4(c), this is illustrated by the smaller energy gap (black arrow) at $B = 410\,\mathrm{mT}$ compared to the one at $B = 300\,\mathrm{mT}$. Due to the reduced energy gap, the resonator-qubit coupling on resonance ($\omega_q < \omega_0$) is reduced and hence is the signal in φ.

The level structure at large magnetic fields is plotted exemplary for $B = 600\,\mathrm{mT}$ in the right panel of Fig. 8.4(c). In this regime, the ground-state of the DQD at the IDT is formed by a superposition of the $T^+_{2,0}$ and $T^+_{1,1}$ states.

We find that the curve of Fig. 8.4(a) turns back towards lower ε for increasing B, which can be understood by noting that the spin-polarized triplets $T^+_{2,0}$ and $T^+_{1,1}$ form a charge qubit similar to the singlets at low field. While the transition is increasingly dominated by the triplet-charge qubit for increasing B, φ becomes negative at the IDT, because the anti-crossing between the triplet states $T^+_{2,0}$ and $T^+_{1,1}$ occurs at much larger frequencies, $2t_c^T > 2t_{\mathrm{SO}}, \omega_0$. Hence, the triplet charge qubit frequency does not cross the resonator frequency, leading to a negative phase shift.

At fields $B > 700$ mT the dispersion turns to higher ε again. Which is not accounted for in our model. A possible explanations to this discrepancy is that the magnetic field not only affects the detuning ε of the DQD but also the total energy. This results in the lead to dot transitions starting to influece the IDT at high magnetic fields. Nevertheless, the data is well described at the magnetic field strengths we investigate in detail.

This large number of detailed findings justify the parameters of the two-electron Hamiltonian introduced above, which, in turn, directly allows us to identify the singlet-triplet spin qubit, for which we find the strong coupling limit to the electromagnetic cavity.

Note, that the extracted qubit linewidth is larger in Fig. 8.4(b) compared to the strong-coupling in Fig. 8.3. This is caused by applying the magnetic field at different angles in the two measurements.

8.5. Conclusion and Outlook

In summary, we demonstrate a semiconductor nanowire DQD device with crystal-phase defined tunnel barriers that can be operated as different types of qubits, coupled to a high-impedance, high magnetic field resilient electromagnetic resonator. As the main result, we find a singlet-triplet qubit for which we extract the relevant qubit parameters, especially a large electron spin-photon coupling of $g/2\pi = 139\,\mathrm{MHz}$ in the single photon limit, reaching the strong coupling regime $g > \gamma, \kappa$.

Our experiments demonstrate that deterministically grown tunnel barriers allow for a reduced number of gate lines, and that, mediated by intrinsic spin-orbit interaction, singlet-triplet qubits can reach the strong coupling limit for low photon numbers, similar to flopping mode spin qubits [108, 251]. This finding is potentially applicable to other promising platforms with strong spin-orbit interactions, like holes in Ge [98]. Our nanowire platform without depletion gates results in a significantly reduced gate-induced photon-leakage in the absence of on-chip filtering [124, 233, 252]. And, since DQD parameters (such as charging energy and individual tunnel rates) can be set deterministically in the NW growth, multiple NWs with optimal and essentially identical characteristics properties can be obtained simultaneously [253] and possibly integrated on the same substrate [254]. This drastically simplifies the search for an optimal gate regime and renders further gates, such as the top gates in our device, unnecessary. An optimized gate design with resonators with larger impedance [222] therefore presents an ideal platform to investigate new phenomena in the ultrastrong coupling regime [222, 255]. Additionally, the large electron spin-photon coupling found in our experiments will be crucial for the implementation of two-qubit gates between distant spin qubits, a milestone on the way towards scalable quantum computers.

We acknowledge fruitful discussions with Simon Zihlmann, Roy Haller, Andrea Hofmann, Stefano Bosco, Romain Maurand and Antti Ranni, and support in setting-up the experiments by Fabian Oppliger, Roy Haller, Luk Yi Cheung, and Deepankar Sarmah. This research was supported by the Swiss Nanoscience Institute (SNI), the Swiss National Science Foundation through grant 192027, the NCCR Quantum Science and Technology (NCCR-QSIT), the NCCR Spin Qubit in Silicon (NCCR-Spin) and the Eccellenza Professorial Fellowship PCEFP2_194268. We further acknowledge funding from the European Union's Horizon 2020 research and innovation programme, specifically the FET-open project AndQC, agreement No 828948 and the FET-open project TOPSQUAD, agreement No 847471. Furthermore, we acknowledge funding by NanoLund and the Knut & Alice Wallenberg Foundation (KAW). PS acknowledges support from the SNSF through grant 200418 and the SERI through grant 589025. All data in this chapter is available in numerical form at: `https://doi.org/10.5281/zenodo.7777840`.

9 Summary and Outlook

In this thesis we studied InAs nanowires (NWs) with integrated crystal-phase defined quantum dots (QDs) as a platform for qubits. We looked at their potential for topological qubits, charge qubits, and spin qubits. We have found that with the available for us facilities they are not a good candidate for majorana bound states (MBS) despite the advantage of well-defined tunnel barriers. In contrast, we have found them a promising tool to study spin qubits coupled to high-impedance superconducting (SC) resonators. Their ease of use and high yield make them an ideal platform to study the physics of the combined resonator double QD (DQD) hybrid system. We have reached the strong spin-photon coupling regime and are confident that further improvements are possible.

We started our journey of the study of InAs NWs with some general characterization of the tunnel barriers and QDs in these NW in **chapter** 4. We observed clean tunnel barriers without any indication of confined states over a large gate range. We identified these NWs as promising candidates for studies of MBS, as the clean barriers without any QD features would reduce the danger of misinterpreting ABS. Furthermore, we have shown well-defined single QDs with tunable barriers, as well as textbook bias triangles of double QDs.

In **chapter** 5 we followed up with studies of the induced superconductivity in these NWs. Employing the built-in tunnel barrier as a spectrometer, we observed a soft SC gap. Using a three-terminal device we argue that we perform spectroscopy on a proximitized region in the NW. Furthermore, we studied the gate dependence of the induced SC gap. Interestingly, we observed a linear dependence of the SC in-gap conductance on the normal above-gap conductance. From this we concluded that the gate mainly tunes the number of modes contributing to transport, but only weakly their transmission coefficient. We extracted an average transmission of all modes contributing to transport and used the BTK-theory to model our SC gap. We compare the induced SC gap without and with built-in tunnel barriers. The much softer gap without built-in tunnel barrier could not be explained solely by a weaker tunnel barrier. Substantial quasiparticle poisoning had to be added to model the SC gap. We speculate that this is either due to some of the many transport modes not properly coupling to the SC proximity region or quasiparticle poisoning from the normal leads.

In chapter 6 we further study quasiparticle poisoning by measuring a Cooper pair island. We develop a technique to evaporate a thin homogeneous layer of aluminium (Al) using a thermal ultra-high vacuum evaporator. We take advantage of the thin Al to fabricate strongly coupled, with the SC self-aligned side gates (SGs). In the first device generation insufficient etching of the native oxide of the Al pads lead to very bad contact to the SGs, in turn creating superconducting charge boxes (SCB) at low temperatures in the SGs. This expressed itself as a purely capacitively coupled triple QD (TQD) in our transport measurements. We used the QD in the NW as a charge detector of the SCBs and observed 2e-periodicity in the charging of the SCBs, as characteristic for an unpoisoned Cooper pair islands. We further used the charge detector to measure the time-resolved tunneling events of single Cooper-pairs in the SCBs. We note, that by changing the fabrication process slightly it should also be possible to use the side-coupled QD as spectrometer of the in the NW defined QD.

Unfortunately, no signs of an unpoisoned Cooper pair island in the proximitized NW QD were observed. We made a second device generation with adjusted fabrication parameters, removing the SCBs and adding a sticking layer. However, still no unpoisoned Cooper pair island was observed. We have to conclude that there is just too much quasiparticle poisoning in the device. Combining this experiment with our results form chapter 5, we propose that the quasiparticle poisoning stems from some of the many-modes not coupling properly to the SC region. This is further supported by literature [33, 43, 204] which achieves hard gaps and unpoisoned Cooper pair islands with epitaxial SC-NW interfaces. As this technology is not currently available to us, we turn to another application that makes us of the great QDs in our NWs without the need of induced superconductivity.

We make use of integrated DQDs in our NWs to couple them to SC high-impedance resonators. This approach pioneered by SC qubits allows high-fidelity non-demolition read out and coupling of qubits over large distances. In **chapter** 7 we study coupling between the resonator and the two-level system defined by the DQD at the inter-dot transition between two charge states. We observe, that the inter-dot tunnel rate is much higher than the resonator frequency. Hence, we measure in the dispersive regime. We extract the tunnel rates, qubit linewidth and charge-photon coupling. While we extract large charge-photon couplings above 100 MHz, our qubit shows a very large linewidth in the GHz range, making it impossible to reach the strong-coupling regime. We speculate that this is due to charge noise.

As a next step, we add an external magnetic field to our NW-resonator hybrid system to address the spin degree of freedom. The intrinsic spin-orbit coupling of the InAs NW allows us to couple charge to spin without the use of micromagnets. In **chapter** 8 we show the magnetic field evolution of an inter-dot transition with an even number of electrons. Using a simplified two-electron Hamiltonian we identify a singlet-triplet qubit. At specific magnetic fields we observe an anti-crossing between the qubit and the resonator. As for the charge qubit we extract tunnel rate, qubit linewidth, and spin-photon coupling. We show that we fulfill the condition of the strong-coupling regime, that the qubit-photon coupling is larger than the combined linewidth of qubit and resonator. This is the first important step towards spin qubits in InAs NWs coupled to a high-impedance resonator.

Outlook

With the technology currently available to us, we do not seem to be able to contact our NWs without inducing significant poisoning into the proximity region. Hydrogen cleaning has shown itself to preserve the InAs surface [256, 257] and an epitaxial SC-NW interface has shown a hard gap and unpoisoned Cooper pair islands in InAs [33, 43, 47, 204]. Furthermore hydrogen radical cleaning has shown hard SC gaps and 2e-periodic Cooper pair islands in InSb [32, 194, 215, 258]. It stands to reason, that this technique should also work for our NWs. However, as this is not an option right now, further studies in this direction are not a priority.

While it is unfortunate, that our NWs are not suited to superconductivity and topololgy studies, they have proven to be a reliable, high-yield platform for QDs coupled to resonators. While we suffered from a bad qubit linewidth for the charge qubit, we managed to achieve strong spin-photon coupling for the spin qubit. Further experiments will build up on this important first step. An immediate next step is to improve the coupling even more by optimizing the device design and resolve the vacuum Rabi splitting. It might also be advantageous to study magnetic field orientation dependence. In silicon hole qubits, this has shown to drastically affect both spin-photon coupling and qubit linewidth [108].

Devices with dedicated high frequency SGs for two-tone measurements and pulsing have already been fabricated and are waiting for measurements. We are optimistic that with these improvements, we will be able to measure Rabi-oscillations and Ramsey-fringes and extract the T_1 and T_2 times. Once we can measure and control a single qubit, it would naturally follow to add a second qubit to the other anti-node at the other end of the resonator and couple them.

Furthermore, other applications with QDs and resonators, could be achieved. Recently, parametric amplifiers based on QDs have been demonstrated [259]. With the combination of our high-quality QDs and resonator, we hope to improve the quality of the QD parametric amplifiers already demonstrated.

Furthermore, we have recently observed that we can evaporate top gates directly on the native oxide of the NW without gate leakage up to 0.5 V. These top gates are as close as possible to the QDs and should increase the charge-photon coupling even more. While charge noise at the interface might be an issue, we might be able to achieve ultrastrong coupling [222], opening a new regime of interesting physics.

A further possibility would be the study of charge and spin qubits defined in triple QDs [123, 260–262] or even more serial QDs, as a larger number of tunnel barriers can easily be added during growth.

In conclusion, there are a lot of interesting possibilities for these built-in NW QDs coupled to resonators, such as the coupling of spin qubits over distances, exploring the strong coupling regime, and QD parametric amplifier. This thesis lied the cornerstone upon which this future applications will be build.

Bibliography

[1] G. Moore, Electronics Magazine **38** (1965).

[2] G. E. Moore, IEEE Solid-State Circuits Society Newsletter **11**, 36 (2006).

[3] M. M. Waldrop, Nature News **530**, 144 (2016).

[4] B. Schumacher, Physical Review A **51**, 2738 (1995).

[5] J. M. Chow, J. M. Gambetta, A. D. Córcoles, S. T. Merkel, J. A. Smolin, C. Rigetti, S. Poletto, G. A. Keefe, M. B. Rothwell, J. R. Rozen, M. B. Ketchen, and M. Steffen, Physical Review Letters **109**, 060501 (2012).

[6] R. Barends, J. Kelly, A. Megrant, A. Veitia, D. Sank, E. Jeffrey, T. C. White, J. Mutus, A. G. Fowler, B. Campbell, Y. Chen, Z. Chen, B. Chiaro, A. Dunsworth, C. Neill, P. O'Malley, P. Roushan, A. Vainsencher, J. Wenner, A. N. Korotkov, A. N. Cleland, and J. M. Martinis, Nature **508**, 500 (2014).

[7] F. Arute, K. Arya, R. Babbush, D. Bacon, J. C. Bardin, R. Barends, R. Biswas, S. Boixo, F. G. S. L. Brandao, D. A. Buell, B. Burkett, Y. Chen, Z. Chen, B. Chiaro, R. Collins, W. Courtney, A. Dunsworth, E. Farhi, B. Foxen, A. Fowler, C. Gidney, M. Giustina, R. Graff, K. Guerin, S. Habegger, M. P. Harrigan, M. J. Hartmann, A. Ho, M. Hoffmann, T. Huang, T. S. Humble, S. V. Isakov, E. Jeffrey, Z. Jiang, D. Kafri, K. Kechedzhi, J. Kelly, P. V. Klimov, S. Knysh, A. Korotkov, F. Kostritsa, D. Landhuis, M. Lindmark, E. Lucero, D. Lyakh, S. Mandrà, J. R. McClean, M. McEwen, A. Megrant, X. Mi, K. Michielsen, M. Mohseni, J. Mutus, O. Naaman, M. Neeley, C. Neill, M. Y. Niu, E. Ostby, A. Petukhov, J. C. Platt, C. Quintana, E. G. Rieffel, P. Roushan, N. C. Rubin, D. Sank, K. J. Satzinger, V. Smelyanskiy, K. J. Sung, M. D. Trevithick, A. Vainsencher, B. Villalonga, T. White, Z. J. Yao, P. Yeh, A. Zalcman, H. Neven, and J. M. Martinis, Nature **574**, 505 (2019).

[8] D. Nigg, M. Müller, E. A. Martinez, P. Schindler, M. Hennrich, T. Monz, M. A. Martin-Delgado, and R. Blatt, Science (New York, N.Y.) **345**, 302 (2014).

[9] T. P. Harty, D. T. C. Allcock, C. J. Ballance, L. Guidoni, H. A. Janacek, N. M. Linke, D. N. Stacey, and D. M. Lucas, Physical Review Letters **113**, 220501 (2014).

[10] A. D. Córcoles, E. Magesan, S. J. Srinivasan, A. W. Cross, M. Steffen, J. M. Gambetta, and J. M. Chow, Nature Communications **6**, 6979 (2015).

[11] J. Preskill, Quantum **2**, 79 (2018).

[12] A. Yu. Kitaev, Annals of Physics **303**, 2 (2003).

[13] A. Stern and N. H. Lindner, Science (New York, N.Y.) **339**, 1179 (2013).

[14] J. Alicea, Physical Review B **81**, 125318 (2010).

[15] J. Alicea, Y. Oreg, G. Refael, F. von Oppen, and M. P. A. Fisher, Nature Physics **7**, 412 (2011).

[16] Y. Oreg, G. Refael, and F. von Oppen, Physical Review Letters **105**, 177002 (2010).

[17] S. D. Sarma, M. Freedman, and C. Nayak, npj Quantum Information **1**, 1 (2015).

[18] L.-A. Wu and D. A. Lidar, Journal of Mathematical Physics **43**, 4506 (2002).

[19] J. Klinovaja and D. Loss, Physical Review B **90**, 045118 (2014).

[20] E. Gaidamauskas, J. Paaske, and K. Flensberg, Physical Review Letters **112**, 126402 (2014).

[21] L. Fu and C. L. Kane, Physical Review Letters **100**, 096407 (2008).

[22] F. Krizek, T. Kanne, D. Razmadze, E. Johnson, J. Nygård, C. M. Marcus, and P. Krogstrup, Nano Letters **17**, 6090 (2017).

[23] J. Gooth, M. Borg, H. Schmid, V. Schaller, S. Wirths, K. Moselund, M. Luisier, S. Karg, and H. Riel, Nano Letters **17**, 2596 (2017).

[24] S. R. Plissard, I. van Weperen, D. Car, M. A. Verheijen, G. W. G. Immink, J. Kammhuber, L. J. Cornelissen, D. B. Szombati, A. Geresdi, S. M. Frolov, L. P. Kouwenhoven, and E. P. A. M. Bakkers, Nature Nanotechnology **8**, 859 (2013).

[25] P. Aseev, G. Wang, L. Binci, A. Singh, S. Martí-Sánchez, M. Botifoll, L. J. Stek, A. Bordin, J. D. Watson, F. Boekhout, D. Abel, J. Gamble, K. Van Hoogdalem, J. Arbiol, L. P. Kouwenhoven, G. de Lange, and P. Caroff, Nano Letters **19**, 9102 (2019).

[26] S. P. Ramanandan, P. Tomić, N. P. Morgan, A. Giunto, A. Rudra, K. Ensslin, T. Ihn, and A. Fontcuberta i Morral, Nano Letters **22**, 4269 (2022).

[27] M. Friedl, K. Cerveny, P. Weigele, G. Tütüncüoglu, S. Martí-Sánchez, C. Huang, T. Patlatiuk, H. Potts, Z. Sun, M. O. Hill, L. Güniat, W. Kim, M. Zamani, V. G. Dubrovskii, J. Arbiol, L. J. Lauhon, D. M. Zumbühl, and A. Fontcuberta i Morral, Nano Letters **18**, 2666 (2018).

[28] J. Jung, S. G. Schellingerhout, M. F. Ritter, S. C. ten Kate, O. A. van der Molen, S. de Loijer, M. A. Verheijen, H. Riel, F. Nichele, and E. P. Bakkers, Advanced Functional Materials **n/a**, 2208974 (2022).

[29] P. Krogstrup, N. L. B. Ziino, W. Chang, S. M. Albrecht, M. H. Madsen, E. Johnson, J. Nygård, C. M. Marcus, and T. S. Jespersen, Nature Materials **14**, 400 (2015).

[30] M. Bjergfelt, D. J. Carrad, T. Kanne, M. Aagesen, E. M. Fiordaliso, E. Johnson, B. Shojaei, C. J. Palmstrøm, P. Krogstrup, T. S. Jespersen, and J. Nygård, Nanotechnology **30**, 294005 (2019).

[31] D. J. Carrad, M. Bjergfelt, T. Kanne, M. Aagesen, F. Krizek, E. M. Fiordaliso, E. Johnson, J. Nygård, and T. S. Jespersen, Advanced Materials **32**, 1908411 (2020).

[32] S. Heedt, M. Quintero-Pérez, F. Borsoi, A. Fursina, N. van Loo, G. P. Mazur, M. P. Nowak, M. Ammerlaan, K. Li, S. Korneychuk, J. Shen, M. A. Y. van de Poll, G. Badawy, S. Gazibegovic, N. de Jong, P. Aseev, K. van Hoogdalem, E. P. A. M. Bakkers, and L. P. Kouwenhoven, Nature Communications **12**, 4914 (2021).

[33] T. Kanne, M. Marnauza, D. Olsteins, D. J. Carrad, J. E. Sestoft, J. de Bruijckere, L. Zeng, E. Johnson, E. Olsson, K. Grove-Rasmussen, and J. Nygård, Nature Nanotechnology **16**, 776 (2021).

[34] X. Jiang, Q. Xiong, S. Nam, F. Qian, Y. Li, and C. M. Lieber, Nano Letters **7**, 3214 (2007).

[35] M. Nilsson, L. Namazi, S. Lehmann, M. Leijnse, K. A. Dick, and C. Thelander, Physical Review B **94** (2016), 10.1103/physrevb.94.115313.

[36] K. A. Dick, C. Thelander, L. Samuelson, and P. Caroff, Nano Letters **10**, 3494 (2010).

[37] M. T. Björk, B. J. Ohlsson, T. Sass, A. I. Persson, C. Thelander, M. H. Magnusson, K. Deppert, L. R. Wallenberg, and L. Samuelson, Nano Letters **2**, 87 (2002).

[38] V. Zannier, F. Rossi, D. Ercolani, and L. Sorba, Nanotechnology **30**, 094003 (2019).

[39] M. Nilsson, L. Namazi, S. Lehmann, M. Leijnse, K. A. Dick, and C. Thelander, Physical Review B **93** (2016), 10.1103/physrevb.93.195422.

[40] S. Lehmann, J. Wallentin, D. Jacobsson, K. Deppert, and K. A. Dick, Nano Letters **13**, 4099 (2013).

[41] M. F. Ritter, H. Schmid, M. Sousa, P. Staudinger, D. Z. Haxell, M. A. Mueed, B. Madon, A. Pushp, H. Riel, and F. Nichele, Nano Letters **21**, 9922 (2021).

[42] M. Knoedler, N. Bologna, H. Schmid, M. Borg, K. E. Moselund, S. Wirths, M. D. Rossell, and H. Riel, Crystal Growth & Design **17**, 6297 (2017).

[43] S. M. Albrecht, A. P. Higginbotham, M. Madsen, F. Kuemmeth, T. S. Jespersen, J. Nygård, P. Krogstrup, and C. M. Marcus, Nature **531**, 206 (2016).

[44] M. T. Deng, S. Vaitiekėnas, E. B. Hansen, J. Danon, M. Leijnse, K. Flensberg, J. Nygård, P. Krogstrup, and C. M. Marcus, Science **354**, 1557 (2016).

[45] M.-T. Deng, S. Vaitiekėnas, E. Prada, P. San-Jose, J. Nygård, P. Krogstrup, R. Aguado, and C. M. Marcus, Physical Review B **98**, 085125 (2018).

[46] S. Vaitiekėnas, G. W. Winkler, B. van Heck, T. Karzig, M.-T. Deng, K. Flensberg, L. I. Glazman, C. Nayak, P. Krogstrup, R. M. Lutchyn, and C. M. Marcus, Science (New York, N.Y.) **367** (2020), 10.1126/science.aav3392.

[47] S. Vaitiekėnas, Y. Liu, P. Krogstrup, and C. M. Marcus, Nature Physics **17**, 43 (2021).

[48] H. Pan and S. Das Sarma, Physical Review Research **2**, 013377 (2020).

[49] E. J. H. Lee, X. Jiang, R. Aguado, G. Katsaros, C. M. Lieber, and S. De Franceschi, Physical Review Letters **109**, 186802 (2012).

[50] M. Valentini, M. Borovkov, E. Prada, S. Martí-Sánchez, M. Botifoll, A. Hofmann, J. Arbiol, R. Aguado, P. San-Jose, and G. Katsaros, Nature **612**, 442 (2022).

[51] M. Valentini, F. Peñaranda, A. Hofmann, M. Brauns, R. Hauschild, P. Krogstrup, P. San-Jose, E. Prada, R. Aguado, and G. Katsaros, Science (New York, N.Y.) **373**, 82 (2021).

[52] C.-X. Liu, J. D. Sau, T. D. Stanescu, and S. Das Sarma, Physical Review B **96**, 075161 (2017).

[53] C. Reeg, O. Dmytruk, D. Chevallier, D. Loss, and J. Klinovaja, Physical Review B **98**, 245407 (2018).

[54] J. Chen, B. D. Woods, P. Yu, M. Hocevar, D. Car, S. R. Plissard, E. P. A. M. Bakkers, T. D. Stanescu, and S. M. Frolov, Physical Review Letters **123**, 107703 (2019).

[55] M. Leijnse and K. Flensberg, Physical Review B **84**, 140501 (2011).

[56] K. Gharavi, D. Hoving, and J. Baugh, Physical Review B **94**, 155417 (2016).

[57] D. Chevallier, P. Szumniak, S. Hoffman, D. Loss, and J. Klinovaja, Physical Review B **97**, 045404 (2018).

[58] A. P. Higginbotham, S. M. Albrecht, G. Kiršanskas, W. Chang, F. Kuemmeth, P. Krogstrup, T. S. Jespersen, J. Nygård, K. Flensberg, and C. M. Marcus, Nature Physics **11**, 1017 (2015).

[59] Y.-J. Doh, S. D. Franceschi, E. P. A. M. Bakkers, and L. P. Kouwenhoven, Nano Letters **8**, 4098 (2008).

[60] C. Jünger, A. Baumgartner, R. Delagrange, D. Chevallier, S. Lehmann, M. Nilsson, K. A. Dick, C. Thelander, and C. Schönenberger, Communications Physics **2** (2019), 10.1038/s42005-019-0162-4.

[61] C. Jünger, R. Delagrange, D. Chevallier, S. Lehmann, K. A. Dick, C. Thelander, J. Klinovaja, D. Loss, A. Baumgartner, and C. Schönenberger, Physical Review Letters **125** (2020), 10.1103/physrevlett.125.017701.

[62] D. Barker, S. Lehmann, L. Namazi, M. Nilsson, C. Thelander, K. A. Dick, and V. F. Maisi, Applied Physics Letters **114**, 183502 (2019).

[63] A. Wallraff, D. I. Schuster, A. Blais, L. Frunzio, R.-S. Huang, J. Majer, S. Kumar, S. M. Girvin, and R. J. Schoelkopf, Nature **431**, 162 (2004).

[64] A. Blais, R.-S. Huang, A. Wallraff, S. M. Girvin, and R. J. Schoelkopf, Physical Review A **69**, 062320 (2004).

[65] A. Blais, A. L. Grimsmo, S. M. Girvin, and A. Wallraff, Reviews of Modern Physics **93**, 025005 (2021).

[66] J. Heinsoo, C. K. Andersen, A. Remm, S. Krinner, T. Walter, Y. Salathé, S. Gasparinetti, J.-C. Besse, A. Potočnik, A. Wallraff, *et al.*, Physical Review Applied **10**, 034040 (2018).

[67] J. Majer, JM. Chow, JM. Gambetta, J. Koch, BR. Johnson, JA. Schreier, L. Frunzio, DI. Schuster, A. A. Houck, A. Wallraff, *et al.*, Nature **449**, 443 (2007).

[68] A. Stockklauser, P. Scarlino, J. V. Koski, S. Gasparinetti, C. K. Andersen, C. Reichl, W. Wegscheider, T. Ihn, K. Ensslin, and A. Wallraff, Physical Review X **7**, 011030 (2017).

[69] X. Mi, J. V. Cady, D. M. Zajac, P. W. Deelman, and J. R. Petta, Science (New York, N.Y.) **355**, 156 (2017).

[70] X. Mi, M. Benito, S. Putz, D. M. Zajac, J. M. Taylor, G. Burkard, and J. R. Petta, Nature **555**, 599 (2018).

[71] N. Samkharadze, G. Zheng, N. Kalhor, D. Brousse, A. Sammak, U. C. Mendes, A. Blais, G. Scappucci, and L. M. K. Vandersypen, Science **359**, 1123 (2018).

[72] A. J. Landig, J. V. Koski, P. Scarlino, UC. Mendes, A. Blais, C. Reichl, W. Wegscheider, A. Wallraff, K. Ensslin, and T. Ihn, Nature **560**, 179 (2018).

[73] D. J. van Woerkom, P. Scarlino, J. H. Ungerer, C. Müller, J. V. Koski, A. J. Landig, C. Reichl, W. Wegscheider, T. Ihn, K. Ensslin, and A. Wallraff, Physical Review X **8**, 041018 (2018).

[74] F. Borjans, XG. Croot, X. Mi, MJ. Gullans, and JR. Petta, Nature **577**, 195 (2020).

[75] P. Harvey-Collard, J. Dijkema, G. Zheng, A. Sammak, G. Scappucci, and L. M. Vandersypen, Physical Review X **12**, 021026 (2022).

[76] M. Nilsson, F. V. Boström, S. Lehmann, K. A. Dick, M. Leijnse, and C. Thelander, Physical Review Letters **121**, 156802 (2018).

[77] T. Ihn, *Semiconductor Nanostructures* (Oxford University Press, 2009).

[78] J. Gramich, *Andreev and Spin Transport in Carbon Nanotube Quantum Dot Hybrid Devices*, Ph.D. thesis, University of Basel (2016).

[79] G. Abulizi, *Quantum Transport in Hexagonal Boron Nitride Carbon Nanotube Heterostructures*, Ph.D. thesis, University of Basel (2017).

[80] J. Schindele, *Observation of Cooper Pair Splitting and Andreev Bound States in Carbon Nanotubes*, Ph.D. thesis, University of Basel (2014).

[81] W. G. van der Wiel, S. De Franceschi, J. M. Elzerman, T. Fujisawa, S. Tarucha, and L. P. Kouwenhoven, Reviews of Modern Physics **75**, 1 (2002).

[82] P. M. Mutter and G. Burkard, Physical Review B **104**, 195421 (2021).

[83] M. Benito, X. Mi, J. M. Taylor, J. R. Petta, and G. Burkard, Physical Review B **96**, 235434 (2017).

[84] L. P. Kouwenhoven, D. G. Austing, and S. Tarucha, Reports on Progress in Physics **64**, 701 (2001).

[85] F. Thomas, A. Baumgartner, L. Gubser, C. Jünger, G. Fülöp, M. Nilsson, F. Rossi, V. Zannier, L. Sorba, and C. Schoenenberger, Nanotechnology (2019), 10.1088/1361-6528/ab5ce6.

[86] G. Abulizi, A. Baumgartner, and C. Schönenberger, physica status solidi (b) **253**, 2428 (2016).

[87] M. Jung, J. Schindele, S. Nau, M. Weiss, A. Baumgartner, and C. Schönenberger, Nano Letters **13**, 4522 (2013).

[88] S. J. Tans, M. H. Devoret, H. Dai, A. Thess, R. E. Smalley, L. J. Geerligs, and C. Dekker, Nature **386**, 474 (1997).

[89] S. Wang, N. Kharche, E. C. Girão, X. Feng, K. Müllen, V. Meunier, R. Fasel, and P. Ruffieux, Nano Letters **17**, 4277 (2017).

[90] J. Weis, R. J. Haug, K. v Klitzing, and K. Ploog, Physical Review Letters **71**, 4019 (1993).

[91] L. P. Kouwenhoven, N. C. van der Vaart, A. T. Johnson, W. Kool, C. J. P. M. Harmans, J. G. Williamson, A. A. M. Staring, and C. T. Foxon, Zeitschrift für Physik B Condensed Matter **85**, 367 (1991).

[92] L. J. Klein, K. A. Slinker, J. L. Truitt, S. Goswami, K. L. M. Lewis, S. N. Coppersmith, D. W. van der Weide, M. Friesen, R. H. Blick, D. E. Savage, M. G. Lagally, C. Tahan, R. Joynt, M. A. Eriksson, J. O. Chu, J. A. Ott, and P. M. Mooney, Applied Physics Letters **84**, 4047 (2004).

[93] M. Eich, R. Pisoni, A. Pally, H. Overweg, A. Kurzmann, Y. Lee, P. Rickhaus, K. Watanabe, T. Taniguchi, K. Ensslin, and T. Ihn, Nano Letters **18**, 5042 (2018).

[94] L. P. Kouwenhoven, C. M. Marcus, P. L. McEuen, S. Tarucha, R. M. Westervelt, and N. S. Wingreen, in *Mesoscopic Electron Transport* (Springer Netherlands, 1997) pp. 105–214.

[95] R. T. Tung, Applied Physics Reviews **1**, 011304 (2014).

[96] M. D. Schroer, K. D. Petersson, M. Jung, and J. R. Petta, Physical Review Letters **107**, 176811 (2011).

[97] J. R. Petta, A. C. Johnson, C. M. Marcus, M. P. Hanson, and A. C. Gossard, Physical Review Letters **93**, 186802 (2004).

[98] D. Jirovec, A. Hofmann, A. Ballabio, P. M. Mutter, G. Tavani, M. Botifoll, A. Crippa, J. Kukucka, O. Sagi, F. Martins, J. Saez-Mollejo, I. Prieto, M. Borovkov, J. Arbiol, D. Chrastina, G. Isella, and G. Katsaros, Nature Materials **20**, 1106 (2021).

[99] D. Jirovec, P. M. Mutter, A. Hofmann, A. Crippa, M. Rychetsky, D. L. Craig, J. Kukucka, F. Martins, A. Ballabio, N. Ares, D. Chrastina, G. Isella, G. Burkard, and G. Katsaros, Physical Review Letters **128**, 126803 (2022).

[100] F. Thomas, *Deterministic Tunnel Barriers in 1D Quantum Electronic Systems*, Thesis, University of Basel (2020).

[101] A. Bordoloi, *Spin Projection and Correlation Experiments in Nanoelectronic Devices*, Thesis, University of Basel (2021).

[102] R. Hanson, L. P. Kouwenhoven, J. R. Petta, S. Tarucha, and L. M. K. Vandersypen, Reviews of Modern Physics **79**, 1217 (2007).

[103] C. W. J. Beenakker, Physical Review B **44**, 1646 (1991).

[104] M. R. Wegewijs and Y. V. Nazarov, "Inelastic Co-Tunneling through an Excited State of a Quantum Dot," (2001), arxiv:cond-mat/0103579 .

[105] D. V. Averin and Yu. V. Nazarov, Physical Review Letters **65**, 2446 (1990).

[106] S. De Franceschi, S. Sasaki, J. M. Elzerman, W. G. van der Wiel, S. Tarucha, and L. P. Kouwenhoven, Physical Review Letters **86**, 878 (2001).

[107] P. Zeeman, Nature **55**, 347 (1897).

[108] C. X. Yu, S. Zihlmann, J. C. Abadillo-Uriel, V. P. Michal, N. Rambal, H. Niebojewski, T. Bedecarrats, M. Vinet, É. Dumur, M. Filippone, B. Bertrand, S. De Franceschi, Y.-M. Niquet, and R. Maurand, Nature Nanotechnology **18**, 741 (2023).

[109] A. Stockklauser, *Strong Coupling Circuit QED with Semiconductor Quantum Dots*, Doctoral Thesis, ETH Zurich (2017).

[110] G. Burkard, M. J. Gullans, X. Mi, and J. R. Petta, Nature Reviews Physics **2**, 129 (2020).

[111] S. Haroche and J. M. Raimond, *Exploring the Quantum: Atoms, Cavities, and Photons* (Oxford Univ. Press, Oxford, 2006).

[112] D. Braak, Physical Review Letters **107**, 100401 (2011).

[113] E. Jaynes and F. Cummings, Proceedings of the IEEE **51**, 89 (1963).

[114] J. H. Ungerer, A. Pally, A. Kononov, S. Lehmann, J. Ridderbos, P. P. Potts, C. Thelander, K. A. Dick, V. F. Maisi, P. Scarlino, A. Baumgartner, and C. Schönenberger, "Strong coupling between a microwave photon and a singlet-triplet qubit," (2023), arxiv:2303.16825 [cond-mat, physics:quant-ph] .

[115] C. W. Gardiner and P. Zoller, *Quantum Noise: A Handbook of Markovian and Non-Markovian Quantum Stochastic Methods with Applications to Quantum Optics*, 3rd ed., Springer Series in Synergetics (Springer, Berlin ; New York, 2004).

[116] C. H. Wong and M. G. Vavilov, Physical Review A **95**, 012325 (2017).

[117] M. Schöndorf, L. C. G. Govia, M. G. Vavilov, R. McDermott, and F. K. Wilhelm, Quantum Science and Technology **3**, 024009 (2018).

[118] E. Kawakami, P. Scarlino, D. R. Ward, F. R. Braakman, D. E. Savage, M. G. Lagally, M. Friesen, S. N. Coppersmith, M. A. Eriksson, and L. M. K. Vandersypen, Nature Nanotechnology **9**, 666 (2014).

[119] M. Veldhorst, J. C. C. Hwang, C. H. Yang, A. W. Leenstra, B. de Ronde, J. P. Dehollain, J. T. Muhonen, F. E. Hudson, K. M. Itoh, A. Morello, and A. S. Dzurak, Nature Nanotechnology **9**, 981 (2014).

[120] J. T. Muhonen, J. P. Dehollain, A. Laucht, F. E. Hudson, R. Kalra, T. Sekiguchi, K. M. Itoh, D. N. Jamieson, J. C. McCallum, A. S. Dzurak, and A. Morello, Nature Nanotechnology **9**, 986 (2014).

[121] K. D. Petersson, J. R. Petta, H. Lu, and A. C. Gossard, Physical Review Letters **105**, 246804 (2010).

[122] Z. Shi, C. B. Simmons, D. R. Ward, J. R. Prance, R. T. Mohr, T. S. Koh, J. K. Gamble, X. Wu, D. E. Savage, M. G. Lagally, M. Friesen, S. N. Coppersmith, and M. A. Eriksson, Physical Review B **88**, 075416 (2013).

[123] A. J. Landig, J. V. Koski, P. Scarlino, U. C. Mendes, A. Blais, C. Reichl, W. Wegscheider, A. Wallraff, K. Ensslin, and T. Ihn, Nature **560**, 179 (2018).

[124] K. D. Petersson, L. W. McFaul, M. D. Schroer, M. Jung, J. M. Taylor, A. A. Houck, and J. R. Petta, Nature **490**, 380 (2012).

[125] K. Takeda, J. Kamioka, T. Otsuka, J. Yoneda, T. Nakajima, M. R. Delbecq, S. Amaha, G. Allison, T. Kodera, S. Oda, and S. Tarucha, Science Advances **2**, e1600694 (2016).

[126] H. Ibach and H. Lüth, *Festkörperphysik*, Springer-Lehrbuch (Springer, Berlin, Heidelberg, 2009).

[127] M. Tinkham, *Introduction to Superconductivity: Second Edition* (Dover Publications, 2004).

[128] R. S. Deacon, Y. Tanaka, A. Oiwa, R. Sakano, K. Yoshida, K. Shibata, K. Hirakawa, and S. Tarucha, Physical Review Letters **104**, 076805 (2010).

[129] J.-D. Pillet, C. H. L. Quay, P. Morfin, C. Bena, A. L. Yeyati, and P. Joyez, Nature Physics **6**, 965 (2010).

[130] C. Bena, The European Physical Journal B **85**, 196 (2012).

[131] C. Jünger, S. Lehmann, K. A. Dick, C. Thelander, C. Schönenberger, and A. Baumgartner, "Intermediate states in Andreev bound state fusion," (2021), arxiv:2111.00651 [cond-mat] .

[132] C. W. J. Beenakker, in *Transport Phenomena in Mesoscopic Systems*, Springer Series in Solid-State Sciences, edited by H. Fukuyama and T. Ando (Springer, Berlin, Heidelberg, 1992) pp. 235–253.

[133] A. Martín-Rodero and A. Levy Yeyati, Advances in Physics **60**, 899 (2011).

[134] O. H. Kamerlingh, Comm. Phys. Lab. Univ., Leiden , 122 (1911).

[135] V. L. Ginzburg, Il Nuovo Cimento (1955-1965) **2**, 1234 (1955).

[136] J. Bardeen, L. N. Cooper, and J. R. Schrieffer, Physical Review **108**, 1175 (1957).

[137] L. N. Cooper, Physical Review **104**, 1189 (1956).

[138] C. Enss and H. Siegfried, *Low-Temperature Physics* (Springer, 2005).

[139] D. J. Thouless, Physical Review **117**, 1256 (1960).

[140] C. W. J. Beenakker, in *Quantum Mesoscopic Phenomena and Mesoscopic Devices in Microelectronics*, NATO Science Series, edited by I. O. Kulik and R. Ellialtioğlu (Springer Netherlands, Dordrecht, 2000) pp. 51–60.

[141] A. F. Andreev, Soviet Physics-JETP **Vol. 19** (1964).

[142] G. E. Blonder, M. Tinkham, and T. M. Klapwijk, Physical Review B **25**, 4515 (1982).

[143] T. M. Klapwijk, Journal of Superconductivity **17**, 593 (2004).

[144] C. H. Jünger, *Transport Spectroscopy of Semiconductor Superconductor Nanowire Hybrid Devices*, Ph.D. thesis, University of Basel (2019).

[145] P. Joyez, Lecture notes Capri Spring School, available: http://www.capri-school.eu/capri12/ (2012).

[146] P. Lafarge, P. Joyez, D. Esteve, C. Urbina, and M. H. Devoret, Physical Review Letters **70**, 994 (1993).

[147] P. Lafarge, P. Joyez, D. Esteve, C. Urbina, and M. H. Devoret, Nature **365**, 422 (1993).

[148] J. Gramich, A. Baumgartner, and C. Schönenberger, Physical Review Letters **115**, 216801 (2015).

[149] S. d. Hollosy, *Locally Tunable inAs Nanowire Quantum Dots for Cooper Pair Splitting*, Thesis, University of Basel (2014).

[150] G. Fábián, *Engineered Magnetoconductance in InAs Nanowire Quantum Dots*, Thesis, University of Basel (2015).

[151] J. H. Ungerer, *High-Impedance Circuit Quantum Electrodynamics with Semiconductor Quantum Dots*, Thesis, University of Basel (2022).

[152] R. Haller, *Probing the Microwave Response of Novel Josephson Elements*, Ph.D. thesis, University of Basel (2021).

[153] J. F. Cochran and D. E. Mapother, Physical Review **111**, 132 (1958).

[154] C. Reale, Acta Physica Academiae Scientiarum Hungaricae **37**, 53 (1974).

[155] F. Pobell, *Matter and Methods at Low Temperatures* (Springer, Berlin, Heidelberg, 2007).

[156] S. Zihlmann, *Spin and Charge Relaxation in Graphene*, Thesis, University of Basel (2018).

[157] “"QCoDeS",” https://qcodes.github.io/Qcodes/.

[158] S. Krinner, S. Storz, P. Kurpiers, P. Magnard, J. Heinsoo, R. Keller, J. Lütolf, C. Eichler, and A. Wallraff, EPJ Quantum Technology **6**, 1 (2019).

[159] X. Duan and C. M. Lieber, Advanced Materials **12**, 298 (2000).

[160] Y.-S. Kim, K. Hummer, and G. Kresse, Physical Review B **80**, 035203 (2009).

[161] M. Hjort, S. Lehmann, J. Knutsson, A. A. Zakharov, Y. A. Du, S. Sakong, R. Timm, G. Nylund, E. Lundgren, P. Kratzer, K. A. Dick, and A. Mikkelsen, ACS Nano **8**, 12346 (2014).

[162] A. G. Milnes and A. Y. Polyakov, Materials Science and Engineering: B **18**, 237 (1993).

[163] H. Potts, I.-J. Chen, A. Tsintzis, M. Nilsson, S. Lehmann, K. A. Dick, M. Leijnse, and C. Thelander, Nature Communications **10**, 5740 (2019).

[164] M. T. Björk, A. Fuhrer, A. E. Hansen, M. W. Larsson, L. E. Fröberg, and L. Samuelson, Physical Review B **72**, 201307 (2005).

[165] S. Csonka, L. Hofstetter, F. Freitag, S. Oberholzer, C. Schönenberger, T. S. Jespersen, M. Aagesen, and J. Nygård, Nano Letters **8**, 3932 (2008).

[166] C. Fasth, A. Fuhrer, L. Samuelson, V. N. Golovach, and D. Loss, Physical Review Letters **98**, 266801 (2007).

[167] S. Nadj-Perge, S. M. Frolov, E. P. a. M. Bakkers, and L. P. Kouwenhoven, Nature **468**, 1084 (2010).

[168] L. Romeo, S. Roddaro, A. Pitanti, D. Ercolani, L. Sorba, and F. Beltram, Nano Letters **12**, 4490 (2012).

[169] C. Flindt, A. S. Sørensen, and K. Flensberg, Physical Review Letters **97**, 240501 (2006).

[170] D. D. Awschalom, L. C. Bassett, A. S. Dzurak, E. L. Hu, and J. R. Petta, Science (New York, N.Y.) **339**, 1174 (2013).

[171] I. Žutić, J. Fabian, and S. Das Sarma, Reviews of Modern Physics **76**, 323 (2004).

[172] A. Hirohata, K. Yamada, Y. Nakatani, I.-L. Prejbeanu, B. Diény, P. Pirro, and B. Hillebrands, Journal of Magnetism and Magnetic Materials **509**, 166711 (2020).

[173] D. Rainis, L. Trifunovic, J. Klinovaja, and D. Loss, Physical Review B **87**, 024515 (2013).

[174] L. Fu, Physical Review Letters **104**, 056402 (2010).

[175] D. Aasen, M. Hell, R. V. Mishmash, A. Higginbotham, J. Danon, M. Leijnse, T. S. Jespersen, J. A. Folk, C. M. Marcus, K. Flensberg, and J. Alicea, Physical Review X **6**, 031016 (2016).

[176] A. Bordoloi, V. Zannier, L. Sorba, C. Schönenberger, and A. Baumgartner, Communications Physics **3** (2020), 10.1038/s42005-020-00405-2.

[177] F. Vigneau, V. Prudkovkiy, I. Duchemin, W. Escoffier, P. Caroff, Y.-M. Niquet, R. Leturcq, M. Goiran, and B. Raquet, Physical Review Letters **112**, 076801 (2014).

[178] S. Dhara, H. S. Solanki, V. Singh, A. Narayanan, P. Chaudhari, M. Gokhale, A. Bhattacharya, and M. M. Deshmukh, Physical Review B **79**, 121311 (2009).

[179] S. F. Karg, V. Troncale, U. Drechsler, P. Mensch, P. D. Kanungo, H. Schmid, V. Schmidt, L. Gignac, H. Riel, and B. Gotsmann, Nanotechnology **25**, 305702 (2014).

[180] K. A. Dick, Progress in Crystal Growth and Characterization of Materials **54**, 138 (2008).

[181] R. S. Wagner and W. C. Ellis, Applied Physics Letters **4**, 89 (1964).

[182] J. M. Redwing, X. Miao, and X. Li, in *Handbook of Crystal Growth (Second Edition)*, Handbook of Crystal Growth, edited by T. F. Kuech (North-Holland, Boston, 2015) pp. 399–439.

[183] G. B. Stringfellow, in *Organometallic Vapor-Phase Epitaxy (Second Edition)*, edited by G. B. Stringfellow (Academic Press, San Diego, 1999) pp. 1–16.

[184] M. Tchernycheva, L. Travers, G. Patriarche, F. Glas, J.-C. Harmand, G. E. Cirlin, and V. G. Dubrovskii, Journal of Applied Physics **102**, 094313 (2007).

[185] X. Yan, X. Zhang, X. Ren, H. Huang, J. Guo, X. Guo, M. Liu, Q. Wang, S. Cai, and Y. Huang, Nano Letters **11**, 3941 (2011).

[186] L. E. Jensen, M. T. Björk, S. Jeppesen, A. I. Persson, B. J. Ohlsson, and L. Samuelson, Nano Letters **4**, 1961 (2004).

[187] M. T. Björk, H. Schmid, C. M. Breslin, L. Gignac, and H. Riel, Journal of Crystal Growth **344**, 31 (2012).

[188] A. I. Hochbaum, R. Fan, R. He, and P. Yang, Nano Letters **5**, 457 (2005).

[189] M. E. Messing, K. Hillerich, J. Bolinsson, K. Storm, J. Johansson, K. A. Dick, and K. Deppert, Nano Research **3**, 506 (2010).

[190] P. H. M. Böttger, Z. Bi, D. Adolph, K. A. Dick, L. S. Karlsson, M. N. A. Karlsson, B. A. Wacaser, and K. Deppert, Nanotechnology **18**, 105304 (2007).

[191] T. Mårtensson, P. Carlberg, M. Borgström, L. Montelius, W. Seifert, and L. Samuelson, Nano Letters **4**, 699 (2004).

[192] U. P. Gomes, D. Ercolani, V. Zannier, F. Beltram, and L. Sorba, Semiconductor Science and Technology **30**, 115012 (2015).

[193] S. Vaitiekėnas, A. M. Whiticar, M.-T. Deng, F. Krizek, J. E. Sestoft, C. J. Palmstrøm, S. Marti-Sanchez, J. Arbiol, P. Krogstrup, L. Casparis, and C. M. Marcus, Physical Review Letters **121**, 147701 (2018).

[194] R. L. M. Op het Veld, D. Xu, V. Schaller, M. A. Verheijen, S. M. E. Peters, J. Jung, C. Tong, Q. Wang, M. W. A. de Moor, B. Hesselmann, K. Vermeulen, J. D. S. Bommer, J. Sue Lee, A. Sarikov, M. Pendharkar, A. Marzegalli, S. Koelling, L. P. Kouwenhoven, L. Miglio, C. J. Palmstrøm, H. Zhang, and E. P. A. M. Bakkers, Communications Physics **3**, 1 (2020).

[195] A. E. Hansen, M. T. Björk, C. Fasth, C. Thelander, and L. Samuelson, Physical Review B **71**, 205328 (2005).

[196] Z. Liu, Z. Zhang, R. Jiang, X. Li, M. Zhang, and D. Qiu, Scripta Materialia **121**, 79 (2016).

[197] Z. Zanolli, F. Fuchs, J. Furthmüller, U. von Barth, and F. Bechstedt, Physical Review B **75**, 245121 (2007).

[198] A. Belabbes, C. Panse, J. Furthmüller, and F. Bechstedt, Physical Review B **86**, 075208 (2012).

[199] L. Ö. Olsson, C. B. M. Andersson, M. C. Håkansson, J. Kanski, L. Ilver, and U. O. Karlsson, Physical Review Letters **76**, 3626 (1996).

[200] S. Chuang, Q. Gao, R. Kapadia, A. C. Ford, J. Guo, and A. Javey, Nano Letters **13**, 555 (2013).

[201] N. Bouarissa and H. Aourag, Infrared Physics & Technology **40**, 343 (1999).

[202] A. C. Ford, S. B. Kumar, R. Kapadia, J. Guo, and A. Javey, Nano Letters **12**, 1340 (2012).

[203] O. Arif, V. Zannier, F. Rossi, D. D. Matteis, K. Kress, M. D. Luca, I. Zardo, and L. Sorba, Nanoscale (2022), 10.1039/D2NR02350D.

[204] W. Chang, S. M. Albrecht, T. S. Jespersen, F. Kuemmeth, P. Krogstrup, J. Nygård, and C. M. Marcus, Nature Nanotechnology **10**, 232 (2015).

[205] H. Zhang, Ö. Gül, S. Conesa-Boj, M. P. Nowak, M. Wimmer, K. Zuo, V. Mourik, F. K. de Vries, J. van Veen, M. W. A. de Moor, J. D. S. Bommer, D. J. van Woerkom, D. Car, S. R. Plissard, E. P. A. M. Bakkers, M. Quintero-Pérez, M. C. Cassidy, S. Koelling, S. Goswami, K. Watanabe, T. Taniguchi, and L. P. Kouwenhoven, Nature Communications **8**, 16025 (2017).

[206] N. A. Court, A. J. Ferguson, and R. G. Clark, Superconductor Science and Technology **21**, 015013 (2007).

[207] A. Melo, C.-X. Liu, P. Rożek, T. Ö. Rosdahl, and M. Wimmer, SciPost Physics **10**, 037 (2021).

[208] J. Danon, A. B. Hellenes, E. B. Hansen, L. Casparis, A. P. Higginbotham, and K. Flensberg, Physical Review Letters **124**, 036801 (2020).

[209] G. C. Ménard, G. L. R. Anselmetti, E. A. Martinez, D. Puglia, F. K. Malinowski, J. S. Lee, S. Choi, M. Pendharkar, C. J. Palmstrøm, K. Flensberg, C. M. Marcus, L. Casparis, and A. P. Higginbotham, Physical Review Letters **124**, 036802 (2020).

[210] C. W. J. Beenakker, Physical Review B **46**, 12841 (1992).

[211] R. Landauer, Zeitschrift für Physik B Condensed Matter **68**, 217 (1987).

[212] R. C. Dynes, V. Narayanamurti, and J. P. Garno, Physical Review Letters **41**, 1509 (1978).

[213] M. H. Devoret, D. Esteve, and C. Urbina, Nature **360**, 547 (1992).

[214] T. M. Eiles, J. M. Martinis, and M. H. Devoret, Physical Review Letters **70**, 1862 (1993).

[215] J. Shen, S. Heedt, F. Borsoi, B. van Heck, S. Gazibegovic, R. L. M. Op het Veld, D. Car, J. A. Logan, M. Pendharkar, S. J. J. Ramakers, G. Wang, D. Xu, D. Bouman, A. Geresdi, C. J. Palmstrøm, E. P. A. M. Bakkers, and L. P. Kouwenhoven, Nature Communications **9**, 4801 (2018).

[216] J. Gramich, A. Baumgartner, and C. Schönenberger, Applied Physics Letters **108**, 172604 (2016).

[217] T. Dirks, Y.-F. Chen, N. O. Birge, and N. Mason, Applied Physics Letters **95**, 192103 (2009).

[218] C. Kittel, *Introduction to Solid State Physics*, 8th ed. (John Wiley & Sons, New York, NY, 2004).

[219] J. Eisenstein, Reviews of Modern Physics **26**, 277 (1954).

[220] J. Aumentado, M. W. Keller, and J. M. Martinis, NIST **72**, 175 (2003).

[221] P. Scarlino, D. J. van Woerkom, U. C. Mendes, J. V. Koski, A. J. Landig, C. K. Andersen, S. Gasparinetti, C. Reichl, W. Wegscheider, K. Ensslin, T. Ihn, A. Blais, and A. Wallraff, Nature Communications **10**, 3011 (2019).

[222] P. Scarlino, J. H. Ungerer, D. J. van Woerkom, M. Mancini, P. Stano, C. Müller, A. J. Landig, J. V. Koski, C. Reichl, W. Wegscheider, T. Ihn, K. Ensslin, and A. Wallraff, Physical Review X **12**, 031004 (2022).

[223] H. Watzinger, J. Kukučka, L. Vukušić, F. Gao, T. Wang, F. Schäffler, J.-J. Zhang, and G. Katsaros, Nature Communications **9**, 3902 (2018).

[224] F. Borjans, X. Zhang, X. Mi, G. Cheng, N. Yao, CAC. Jackson, LF. Edge, and JR. Petta, PRX Quantum **2**, 020309 (2021).

[225] S. Probst, F. B. Song, P. A. Bushev, A. V. Ustinov, and M. Weides, Review of Scientific Instruments **86**, 024706 (2015).

[226] T. Frey, PJ. Leek, M. Beck, A. Blais, T. Ihn, K. Ensslin, and A. Wallraff, Physical Review Letters **108**, 046807 (2012).

[227] C. Livermore, C. H. Crouch, R. M. Westervelt, K. L. Campman, and A. C. Gossard, Science (New York, N.Y.) **274**, 1332 (1996).

[228] B. W. Shore and P. L. Knight, Journal of Modern Optics **40**, 1195 (1993).

[229] R. Wang, R. S. Deacon, D. Car, E. P. a. M. Bakkers, and K. Ishibashi, Applied Physics Letters **108**, 203502 (2016).

[230] R. Wang, R. S. Deacon, J. Sun, J. Yao, C. M. Lieber, and K. Ishibashi, Nano Letters **19**, 1052 (2019).

[231] F. Bloch and A. Siegert, Physical Review **57**, 522 (1940).

[232] B. A. Mazin, *Microwave Kinetic Inductance Detectors*, Ph.D. thesis, California Institute of Technology (2005).

[233] P. Harvey-Collard, G. Zheng, J. Dijkema, N. Samkharadze, A. Sammak, G. Scappucci, and L. M. K. Vandersypen, Physical Review Applied **14**, 034025 (2020).

[234] J. H. Ungerer, D. Sarmah, A. Kononov, J. Ridderbos, R. Haller, L. Y. Cheung, and C. Schönenberger, EPJ Quantum Technology **10**, 1 (2023).

[235] M. D. Reed, B. M. Maune, R. W. Andrews, M. G. Borselli, K. Eng, M. P. Jura, A. A. Kiselev, T. D. Ladd, S. T. Merkel, I. Milosavljevic, E. J. Pritchett, M. T. Rakher, R. S. Ross, A. E. Schmitz, A. Smith, J. A. Wright, M. F. Gyure, and A. T. Hunter, Physical Review Letters **116**, 110402 (2016).

[236] X.-C. Yang and X. Wang, Physical Review A **96**, 012318 (2017).

[237] A. V. Kuhlmann, J. Houel, A. Ludwig, L. Greuter, D. Reuter, A. D. Wieck, M. Poggio, and R. J. Warburton, Nature Physics **9**, 570 (2013).

[238] J. H. Ungerer, A. Pally, A. Kononov, S. Lehmann, J. Ridderbos, P. P. Potts, C. Thelander, K. A. Dick, V. F. Maisi, P. Scarlino, A. Baumgartner, and C. Schönenberger, Nature Communications **15**, 1068 (2024).

[239] F. A. Zwanenburg, A. S. Dzurak, A. Morello, M. Y. Simmons, L. C. L. Hollenberg, G. Klimeck, S. Rogge, S. N. Coppersmith, and M. A. Eriksson, Reviews of Modern Physics **85**, 961 (2013).

[240] L. M. K. Vandersypen, H. Bluhm, J. S. Clarke, A. S. Dzurak, R. Ishihara, A. Morello, D. J. Reilly, L. R. Schreiber, and M. Veldhorst, npj Quantum Information **3**, 1 (2017).

[241] A. Chatterjee, P. Stevenson, S. De Franceschi, A. Morello, N. P. de Leon, and F. Kuemmeth, Nature Reviews Physics **3**, 157 (2021).

[242] L. Childress, A. S. Sørensen, and M. D. Lukin, Physical Review A **69**, 042302 (2004).

[243] X. Mi, C. G. Péterfalvi, G. Burkard, and J. R. Petta, Physical Review Letters **119**, 176803 (2017).

[244] J. R. Petta, A. C. Johnson, J. M. Taylor, E. A. Laird, A. Yacoby, M. D. Lukin, C. M. Marcus, M. P. Hanson, and A. C. Gossard, Science **309**, 2180 (2005).

[245] A. J. Landig, J. V. Koski, P. Scarlino, C. Reichl, W. Wegscheider, A. Wallraff, K. Ensslin, and T. Ihn, Physical Review Letters **122**, 213601 (2019).

[246] C. G. L. Bøttcher, S. P. Harvey, S. Fallahi, G. C. Gardner, M. J. Manfra, U. Vool, S. D. Bartlett, and A. Yacoby, Nature Communications **13**, 4773 (2022).

[247] N. Samkharadze, A. Bruno, P. Scarlino, G. Zheng, DP. DiVincenzo, L. DiCarlo, and LMK. Vandersypen, Physical Review Applied **5**, 044004 (2016).

[248] D. J. Ibberson, T. Lundberg, J. A. Haigh, L. Hutin, B. Bertrand, S. Barraud, C.-M. Lee, N. A. Stelmashenko, G. A. Oakes, L. Cochrane, J. W. Robinson, M. Vinet, M. F. Gonzalez-Zalba, and L. A. Ibberson, PRX Quantum **2**, 020315 (2021).

[249] S. Nadj-Perge, S. M. Frolov, J. W. W. van Tilburg, J. Danon, Yu. V. Nazarov, R. Algra, E. P. A. M. Bakkers, and L. P. Kouwenhoven, Physical Review B **81**, 201305 (2010).

[250] M. Trif, V. N. Golovach, and D. Loss, Physical Review B **77**, 045434 (2008).

[251] G. Burkard, T. D. Ladd, A. Pan, J. M. Nichol, and J. R. Petta, Reviews of Modern Physics **95**, 025003 (2023).

[252] X. Mi, JV. Cady, DM. Zajac, J. Stehlik, LF. Edge, and J. R. Petta, Applied Physics Letters **110**, 043502 (2017).

[253] M. Nilsson, I.-J. Chen, S. Lehmann, V. Maulerova, K. A. Dick, and C. Thelander, Nano Letters **17**, 7847 (2017).

[254] M. S. Ram, K.-M. Persson, A. Irish, A. Jönsson, R. Timm, and L.-E. Wernersson, Nature Electronics **4**, 914 (2021).

[255] P. Forn-Díaz, L. Lamata, E. Rico, J. Kono, and E. Solano, Reviews of Modern Physics **91**, 025005 (2019).

[256] E. Hilner, U. Håkanson, L. E. Fröberg, M. Karlsson, P. Kratzer, E. Lundgren, L. Samuelson, and A. Mikkelsen, Nano Letters **8**, 3978 (2008).

[257] J. L. Webb, J. Knutsson, M. Hjort, S. Gorji Ghalamestani, K. A. Dick, R. Timm, and A. Mikkelsen, Nano Letters **15**, 4865 (2015).

[258] J. Shen, G. W. Winkler, F. Borsoi, S. Heedt, V. Levajac, J.-Y. Wang, D. van Driel, D. Bouman, S. Gazibegovic, R. L. M. Op Het Veld, D. Car, J. A. Logan, M. Pendharkar, C. J. Palmstrøm, E. P. A. M. Bakkers, L. P. Kouwenhoven, and B. van Heck, Physical Review B **104**, 045422 (2021).

[259] L. Cochrane, T. Lundberg, D. J. Ibberson, L. A. Ibberson, L. Hutin, B. Bertrand, N. Stelmashenko, J. W. A. Robinson, M. Vinet, A. A. Seshia, and M. F. Gonzalez-Zalba, Physical Review Letters **128**, 197701 (2022).

[260] K. Eng, T. D. Ladd, A. Smith, M. G. Borselli, A. A. Kiselev, B. H. Fong, K. S. Holabird, T. M. Hazard, B. Huang, P. W. Deelman, I. Milosavljevic, A. E. Schmitz, R. S. Ross, M. F. Gyure, and A. T. Hunter, Science Advances **1**, e1500214 (2015).

[261] J. Z. Blumoff, A. S. Pan, T. E. Keating, R. W. Andrews, D. W. Barnes, T. L. Brecht, E. T. Croke, L. E. Euliss, J. A. Fast, C. A. Jackson, A. M. Jones, J. Kerckhoff, R. K. Lanza, K. Raach, B. J. Thomas, R. Velunta, A. J. Weinstein, T. D. Ladd, K. Eng, M. G. Borselli, A. T. Hunter, and M. T. Rakher, PRX Quantum **3**, 010352 (2022).

[262] B. Kratochwil, J. V. Koski, A. J. Landig, P. Scarlino, J. C. Abadillo-Uriel, C. Reichl, S. N. Coppersmith, W. Wegscheider, M. Friesen, A. Wallraff, T. Ihn, and K. Ensslin, Physical Review Research **3**, 013171 (2021).

[263] C. Gatzke, S. J. Webb, K. Fobelets, and R. A. Stradling, Semiconductor Science and Technology **13**, 399 (1998).

[264] C. Thelander, P. Caroff, S. Plissard, A. W. Dey, and K. A. Dick, Nano Letters **11**, 2424 (2011).

[265] A. Crippa, R. Ezzouch, A. Aprá, A. Amisse, R. Laviéville, L. Hutin, B. Bertrand, M. Vinet, M. Urdampilleta, T. Meunier, *et al.*, Nature communications **10**, 1 (2019).

[266] R. Ezzouch, S. Zihlmann, V. P. Michal, J. Li, A. Aprá, B. Bertrand, L. Hutin, M. Vinet, M. Urdampilleta, T. Meunier, X. Jehl, Y.-M. Niquet, M. Sanquer, S. De Franceschi, and R. Maurand, Physical Review Applied **16**, 034031 (2021).

[267] S. Park, C. Metzger, L. Tosi, M. F. Goffman, C. Urbina, H. Pothier, and A. L. Yeyati, Physical Review Letters **125**, 077701 (2020).

[268] M. D. Schroer, M. Jung, K. D. Petersson, and J. R. Petta, Physical Review Letters **109**, 166804 (2012).

[269] F. K. Malinowski, F. Martins, T. B. Smith, S. D. Bartlett, A. C. Doherty, P. D. Nissen, S. Fallahi, G. C. Gardner, M. J. Manfra, C. M. Marcus, and F. Kuemmeth, Physical Review X **8**, 011045 (2018).

A Fabrication Recipes

The fabrication techniques used in this work can be found in 3. This appendix shows the detailed fabrication recipes.

A.1. Fabrication of InAs NW Devices

A.1.1. Wafer Characteristics

- **Substrate Material:** Highly doped Silicon
- **Dopant:** Boron (p-doped)
- **Resistivity:** $0.003 - 0.005\,\Omega\mathrm{m}$
- **Capping Layer:** 400 nm thick thermally grown SiO_2

A.1.2. Wafer Cleaning

1. Dice the wafer into 2 cm x 2 cm pieces.
2. Sonicate in acetone for $\sim$ 20 min.
3. Sonicate in IPA for $\sim$ 20 min.
4. Blow dry with pressurized air or N_2

A.2. E-beam Lithography, Development and Lift-off

- **Resist:** PMMA 950K dissolved in Anisole.
- **Spin Coating:** 2400 RPM for 60s resulting in a thickness of $\sim 300\,\mathrm{nm}$.
- **Baking:** 180°C on a hotplate for 5 minutes.
- **Area Dose:** $270\,\mu\mathrm{C/cm^2}$ at $17\,\mathrm{kV}$
- **Development:** 3:1 Isopropyl alcohol (IPA) / Methylisobutyl ketone (MIBK) for 60 seconds followed by a dip in IPA and blow dry with pressurized air or N_2.

- **Liftoff:** 30 minutes or longer in 50°C warm acetone.

A.3. Reactive ion etching - O_2 Plasma Etching

To remove residue with PMMA resist only.

- **Parameters:**
  - **O_2 Flow:** 16 %
  - **RF Power:** 30 W
  - **Process Pressure:** 250 mTorr
  - **Time:** 60 s
- **Etch Rates:**
  - **SiO_2:** negligible
  - **PMMA:** ~20 nm/min

A.4. Etching of the GaSb-shell before metallization

To remove the GaSb-shell before contacting and further processing.

1. Clamp NW with metal at the bottom below the contact area using standard E-beam lithography and evaporation.
2. Perform 1 min O_2 cleaning.
3. Etch for 3 minutes and 30 seconds in MF319 developer under strong movement
4. Rinse thoroughly with deionized water
5. Rinse with IPA
6. Blow dry with pressurized air or N_2

A.5. Contacts

A.5.1. Ti/Au contacts

Used for base structures and normal metal contacts and gates.

1. **Type:** E-beam evaporation in Balzers.
2. Pump to a base pressure of $\sim 2e^{-6}$ mbar.

3. For contacts: Align sample stage with ion gun and perform a 26s in-situ Ar-mill.

4. Align sample stage with metal sources

5. Evaporate 5 nm of Ti (0.5 Å per second).

6. Evaporate 90 nm of Au (1.5 Å per second).

A.5.2. Ti/Al contacts

Used for thick Al superconducting contacts.

1. **Type:** E-beam evaporation in Balzers.

2. Pump to a base pressure of $\sim 2e^{-6}$ mbar.

3. Align sample stage with ion gun and perform a 26 second in-situ Ar-mill.

4. Evaporate 5 nm of Ti (0.5 Å per second).

5. Evaporate 95 nm of Al (1.5 Å per second).

A.5.3. Thin Al contacts

Used for thin Al superconducting contacts.

1. **Type:** Thermal evaporation in Bestec.

2. Mount sample on holder with a bit of Ga on the back of the sample for good thermal contact

3. Load in loadlock and pump below $\sim 2e^{-6}$ mbar.

4. Perform 2 minutes 30 seconds in-situ Ar-mill.

5. Transfer sample to main chamber with pressure $\sim 3e^{-9}$ mbar.

6. Cool sample stage to -75 °C with liquid nitrogen.

7. Heat up source and evaporate 12 nm of Al (0.015 Å per second).

B Additional data on the material platform

This appendix provides further information to chapter 4.

B.1. Gate dependence with and without built-in tunnel barrier

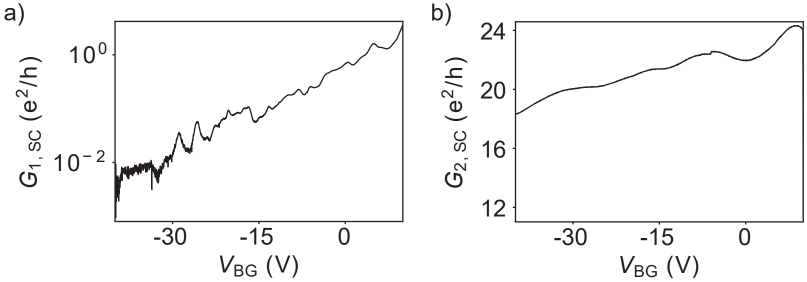

Figure B.1. Gate dependence with and without built-in tunnel barrier. Differntial conductance G as a function of back gate voltage V_{BG} where the bias voltage $V_{SD} = 0$ is applied on the superconducting contact SC and the current is measured on N1 (a) and N2 (b). The conductance in a) is plotted on log-scale.

The back gate dependence disucssed in chapter 4 for the three-terminal device with and without built-in tunnel barrier between the contacts is shown in Fig. B.1. Here, the conductance $G_{i,SC}$ is plotted as a function of V_{BG} with $V_{SD} = 0$ applied on SC and the current measured on normal contact N$_i$. There is a built-in tunnel barrier between N1 and SC, while the barrier between SC and N2 is shorted by SC. The back gate dependence is clearly stronger in $G_{1,SC}$. Note, that $G_{1,SC}$ is plotted in log-scale.

B.2. Addition energy of a single quantum dot

Figure B.2 shows the extracted addition energy E_{add} for the single QD discussed in chapter 4. We observe a even-odd pattern due to spin-degeneracy.

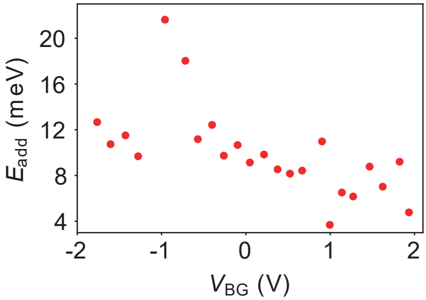

Figure B.2. Addition energy E_{add} of a single QD. Extracted E_{add} as a function of V_{BG}.

We extract $E_C \approx 11.2$ meV and $\delta E \approx 1.2$ meV. We also observe a general decrease of E_{add} with increasing V_{BG} due to increased screening effects as the QD get filled with more electrons [77, 100]. Note, that the data point with much higher E_{add} corresponds to the thermally broadened Coulomb blockade resonance.

C Additional data on Cooper pair charge sensing of a superconducting charge box

This appendix provides further information to chapter 6.

C.1. Full dataset on magnetic field maps

The complete set of magnetic field maps used to extract the data in Fig. 6.4 and Fig. 6.6 are shown in Figs. C.1-C.4.

C.2. Wrongly detected tunnel events

In Fig. C.5 the two current measurements at finite magnetic field, were tunnel events were wrongly detected by the algorithm, are shown.

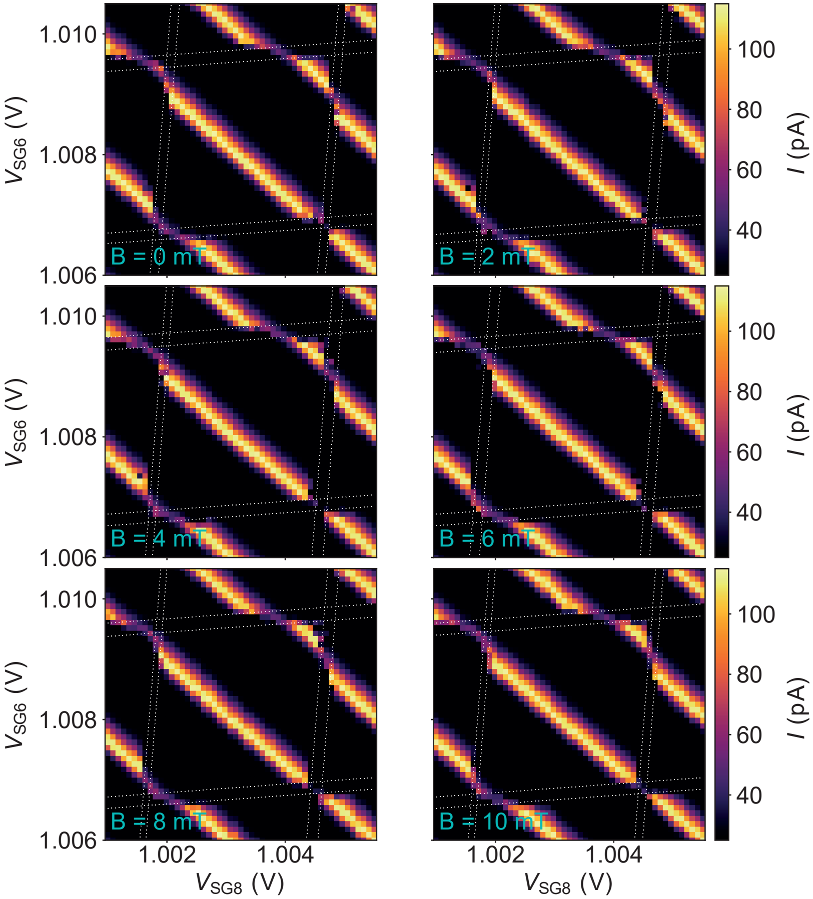

Figure C.1. Current maps from zero to 10 mT. Measured current as a function of V_{SG6} and V_{SG8} for magnetic fields from 0 to 10 mT.

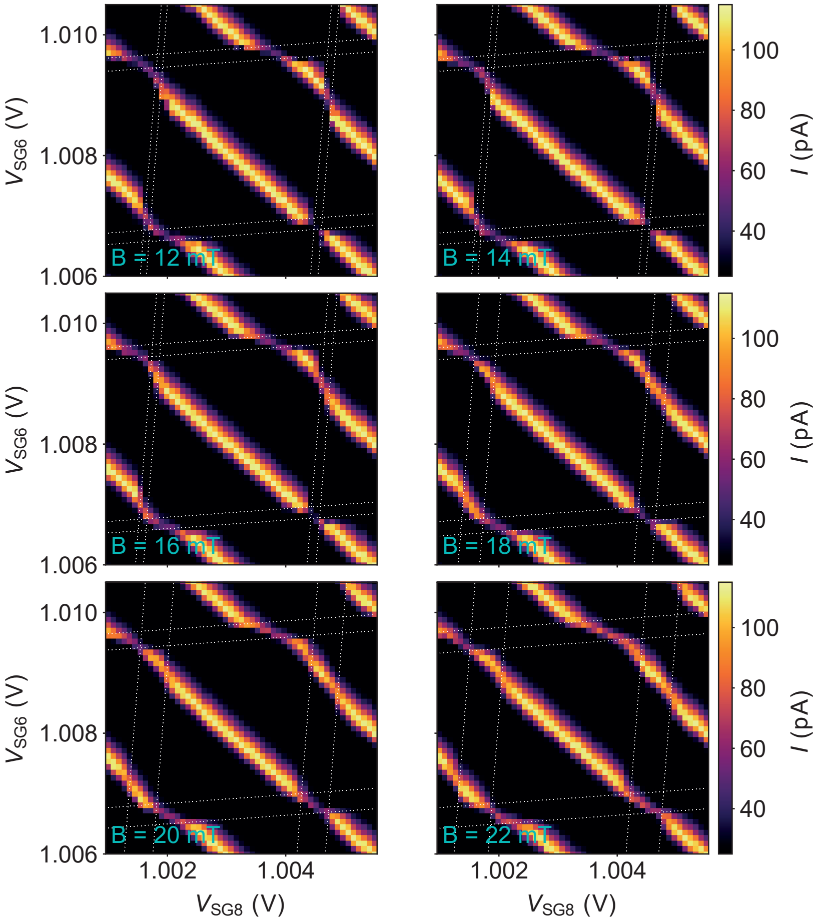

Figure C.2. Current maps from 12 mT to 22 mT. Measured current as a function of V_{SG6} and V_{SG8} for magnetic fields from 12 mT to 22 mT.

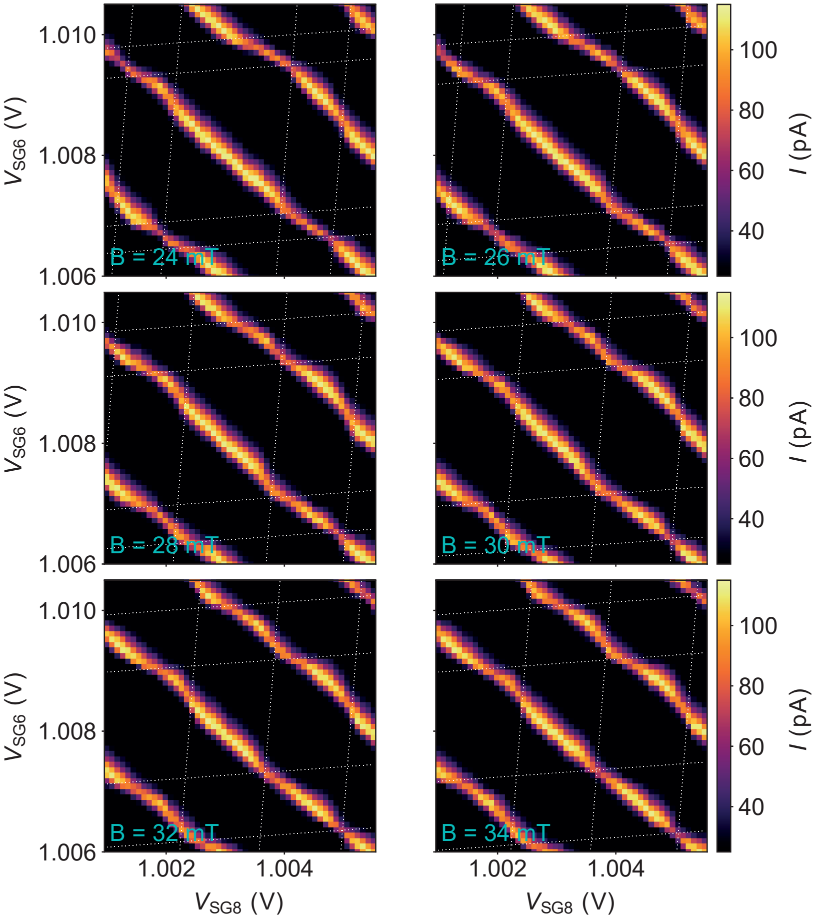

Figure C.3. Current maps from 24 mT to 34 mT. Measured current as a function of V_{SG6} and V_{SG8} for magnetic fields from 24 mT to 34 mT.

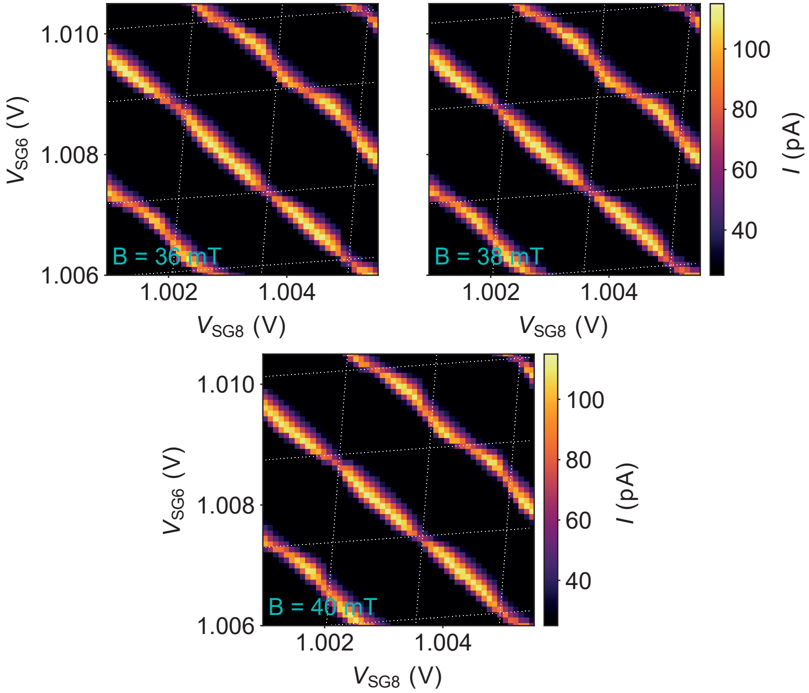

Figure C.4. Current maps from 36 mT to 40 mT. Measured current as a function of V_{SG6} and V_{SG8} for magnetic fields from 36 mT to 40 mT.

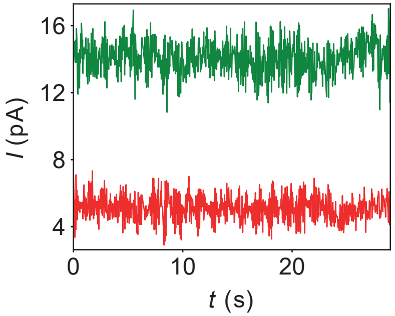

Figure C.5. Wrongly detected tunnel events. Current measurements as a function of time. For this two measurements tunnel events were wrongly detected by the algorithm.

D Additional data strong coupling between a microwave photon and a singlet-triplet qubit

This appendix provides further information to chapter 8. It is also available in the supplementary of the publication [238].

D.1. Resonator characterization and analysis

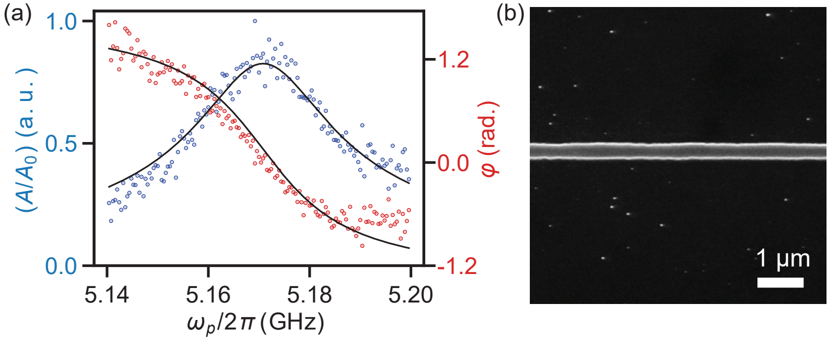

Figure D.1. Resonator of a device A. (a) Resonance curve of the resonator in Coulomb blockade in amplitude A/A_0 (blue) and phase φ (red). The black lines are simultaneous fits to the data using input-ouput theory. (b) Scanning electron micrograph of the resonator center conductor.

The resonator is fabricated from a thin-film NbTiN (thickness ∼10 nm), sputtered onto a Si/SiO$_2$ (500 µm/100 nm) substrate [234]. These resonators can be operated for in-plane fields exceeding 5 T [234, 247]. The large sheet kinetic inductance of the used NbTiN film of $L_{\mathrm{sq}} \approx 90\,\mathrm{pH}$ combined with the narrow center conductor width of ∼ 380 nm, and the large distance to the ground plane of ∼ 35 µm results in an impedance of 2.1 kΩ. The resonator can be dc biased using a bias line which contains a meandered inductor ensuring sufficient frequency detuning between the half-wave resonance used in the experiment and a second, low quality resonance mode at a lower frequency that forms due to the finite inductance of the bias line [233]. A scanning electron micrograph of the resonator center-conductor is shown in Fig.D.1(b) in the extended data. One of the two resonator voltage anti-nodes is galvanically connected to gate SG_R shown in Fig. 8.1(c) of the main text.

D.2. InAs crystal-phase nanowires

InAs nanowires with controlled crystal structure were grown by metal-organic vapor phase epitaxy (MOVPE) from Au aerosol nanoparticles with a nominal diameter of 30 nm deposited on InAs 111B substrates. After annealing, nanowires were grown at 460 °C by introducing trimethylindium (TMIn) at a molar fraction of $\chi_{\mathrm{TMIn}} = 1.8 \cdot 10^{-6}$ and Arsine ($\mathrm{AsH_3}$) at a molar fraction of $\chi_{\mathrm{AsH_3}} = 1.2 \cdot 10^{-4}$. Crystal-phase switching is realized by modifying the $\mathrm{AsH_3}$ molar fractions from $\chi_{\mathrm{AsH_3}} = 2.5 \cdot 10^{-2}$ for zinc blende to $\chi_{\mathrm{AsH_3}} = 2.2 \cdot 10^{-5}$ for wurtzite, with 15 s waiting steps under $\mathrm{AsH_3}$. The wurtzite barrier growth time is 54 s and the zinc blende segment growth time is 360 s. Deposited at the same growth temperature, the GaSb shell was grown for 40 minutes with respective molar fractions of trimethylgallium (TMGa) $\chi_{\mathrm{TMGa}} = 2.7 \cdot 10^{-6}$ and trimethylantimony (TMSb) $\chi_{\mathrm{TMSb}} = 3.1 \cdot 10^{-5}$. As the nanowires in this work were grown from randomly deposited Au seed particles, a variability in the local growth conditions was present that affect nanowire growth rate and segment lengths. However, by adding the GaSb shell that selectively deposits on zinc blende surfaces, it is possible to identify nanowires with desired segment lengths, and to accurately position contacts and local gates to these [62]. The GaSb-shell is then removed before contacting by a wet-etching process using MF-319 developer [263].

By growing nanowires in arrays, such as from lithographically defined Au particles, the variability in segment lengths can be greatly reduced [253]. The electron mobility in these nanowires is primarily limited by the wurtzite tunnel barriers and surface scattering. InAs nanowires with a pure zinc-blende crystal phase grown by a corresponding method show a room-temperature field-effect mobility of approximately 2000 $\mathrm{cm^2/Vs}$ [264].

In total, we have fabricated 4 nanowire devices coupled to a high-impedance resonator. All nanowires demonstrated well-defined double-quantum dots as expected from their barrier design. Out of these 4 devices, two were investigated at elevated magnetic-field strengths and both of them showed similar behavior as discussed in the manuscript.

D.3. Hamiltonian in the odd charge parity

In the main text, we elaborate on the Hamiltonian describing the double quantum dot (DQD) for an even charge occupation. This section provides the description for an *odd* number of electrons which is used in order to obtain Fig. 6(d) in the extended data. In this case, the total electron spin is 1/2 which can be modelled by one electron with a half spin. This electron can reside either on the left dot or on the right dot [81]. Therefore, a suitable basis is $\{|\mathrm{L}\uparrow\rangle, |\mathrm{L}\downarrow\rangle, |\mathrm{R}\uparrow\rangle, |\mathrm{R}\downarrow\rangle\}$, where L/R denotes whether the charge resides in the left dot or on the right dot, and ↑/↓ denotes whether the spin is aligned parallel or anti-parallel with the magnetic field B.

The Hamiltonian describing the electron can be decomposed into three parts as

$$\mathcal{H}_{\mathrm{odd}} = \mathcal{H}^{0}_{\mathrm{odd}} + \mathcal{H}^{Z}_{\mathrm{odd}} + \mathcal{H}^{\mathrm{SO}}_{\mathrm{odd}} \tag{D.1}$$

The first part of the Hamiltonian describes the spin-independent charge which can be written using the the charge Pauli matrices $\hat{\tau}_{x,y,z}$ as

$$\mathcal{H}^{0}_{\mathrm{odd}} = \frac{\hbar\epsilon}{2}\hat{\tau}_z + \hbar t_c \hat{\tau}_x. \tag{D.2}$$

Here, the diagonal terms are proportional to the detuning $\hbar\epsilon = E_R - E_L$ which is the difference between the electro-static potential of the electron residing in the right and left dot. The off-diagonal terms are given by $\hbar t_c$, which is the spin-conserving tunnel rate.

In the presence of a magnetic-field, $\mathcal{H}^{Z}_{\mathrm{odd}}$ comes into effect. This term describes the Zeeman energy of the electron and is given by

$$\mathcal{H}^{Z}_{\mathrm{odd}} = \frac{1}{2} g_{L,R} \mu_B B \hat{\sigma}_z, \tag{D.3}$$

where g_L and g_R are the site-dependent Landé g-factors, μ_B is the Bohr magneton and $\hat{\sigma}_{x,y,z}$ are the spin Pauli matrices. The Zeeman energy lifts the spin degeneracy and hence four spin-polarized levels are observed as shown in Fig. 6(d) in the extended data. As explained in the methods section, unequal g factors $g_L \neq g_R$ result in a shift of the avoided level crossings originating from spin-conserving tunneling. This results in a slope of the observed interdot transition as a function of gate voltage (detuning) and field from zero field onward.

D.4. Extraction of parameters using input-output theory

Parameters are extracted as described in chapter 2.2.2. Figure D.2 illustrates the fit of input-output theory to the data.

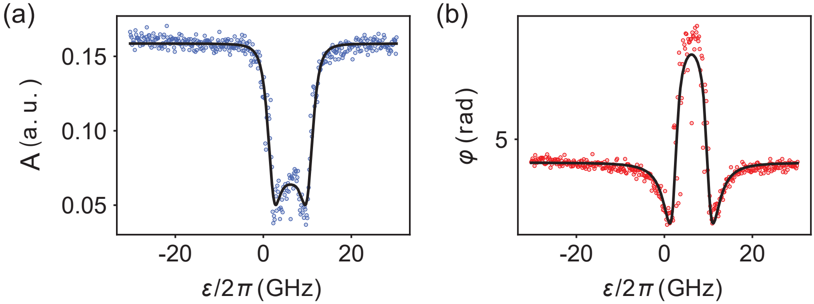

Figure D.2. Fit of input-output theory to the data. Input-output theory (solid lines) simoultaneously fitted to the resonator amplitude A (a) and the resonator phase φ (b) as a function of detuning ε of the even configuration at 0.25 T.

D.5. Charge parity determination

We measure the phase φ and amplitude A of the resonator as a function of detuning ε and magnetic field B at a probe-frequency $\omega_\mathrm{p}/2\pi = 5.253\,\mathrm{GHz}$, close to the bare resonator frequency. A change in φ reflects the dispersive interaction between the resonator and two anticrossing levels of the DQD [226, 265]. Therefore, the non-zero phase response of the resonator tracks the position of the IDT along the detuning axis. The comparison of the magnetic field dependence of the IDT position to a Hamiltonian model of the DQD allows one to determine the charge parity [265, 266]. Figures D.3 (a) and (b) in the extended data show two typical low field IDT characteristics of device B.

For an odd number of electrons (Fig. D.3(b)), the DQD resonance gate voltage V_R, at which the IDT is observed, disperses linearly with magnetic field starting from zero. This can be understood considering the Zeeman-splitting of the unpaired electron energy levels and two non-equal Landé g-factors of the two dots. Fig. D.3(c) shows the energy level diagram of a one-electron Hamiltonian including Zeeman-splitting with a g-factor difference of 1.0 and spin-orbit interaction $t_{SO}/2\pi = 5$ GHz at a magnetic field of $B = 500\,\mathrm{mT}$ (green, dashed line in Fig. D.3(b)). The arrow points out the center of the IDT (largest curvature of the groundstate [267]) which corresponds to the largest dipole moment of the DQD and thus to the largest change in φ. This point shifts with B towards increasingly negative values.

For an even number of electrons in the DQD at zero magnetic field (Fig. D.3(a)), a single dip in phase is observed, but at a low magnetic fields, $B \approx 60\,\mathrm{mT}$, a double dip structure emerges as a function of ε (see supplementary material

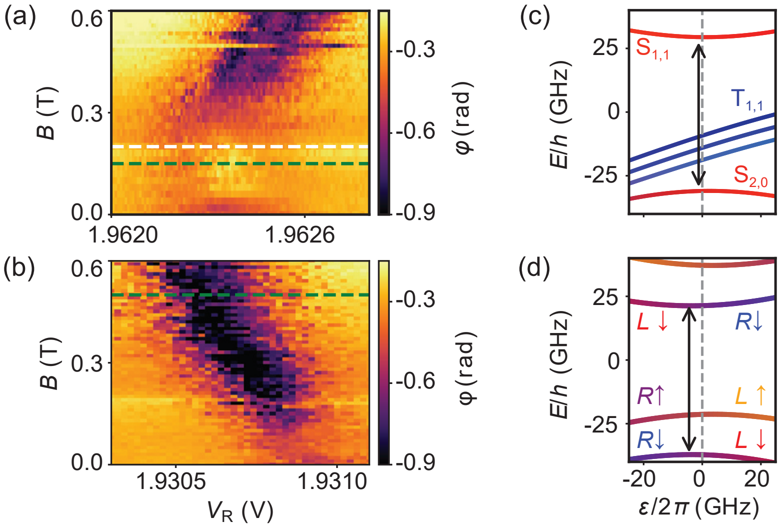

Figure D.3. Dispersive read-out at low magnetic field. Resonator phase in dependence of the right gate voltage V_R and magnetic field B for even (a) and odd (b) occupation of the DQD of device B. For the odd occupation the IDT shifts to lower V_R from $B = 0$. The IDT of the even occupation stays nearly independent of magnetic field until around 0.2 T (white dashed line), from where it starts moving to more positive V_R. Energy level diagram for the even (c) and odd (d) configuration at 0.15 T and 0.5 T (green dashed line). The arrow marks the transition the resonator is sensitive to, where the ground state energy level has maximum curvature.

for details). This double-dip originates from an interaction between $S_{2,0}$, $S_{1,1}$ and $T^{+}_{1,1}$ as explained in detail in the supplementary material. The dependence of the IDT on magnetic field for an even number of electrons can be understood using an effective two electron Hamiltonian including spin-orbit interaction described in more detail in section 2.1.6. In Fig. D.3(c), we plot the energy levels at a magnetic field $B = 0.15$ T. In contrast to the odd filling, starting at zero magnetic field, the arrow marking the center of the IDT barely changes, consistent with our measurement. The double dip vanishes when further increasing the magnetic field, because of an increasing occupation of the polarized triplet states. Once the Zeeman energy of the triplet state $|T^{+}_{1,1}\rangle$ becomes comparable to the singlet charge tunneling t_c^{S}, the position of the IDT as a function of B disperses towards larger ε [266, 268, 269]. This transition is marked by the white dashed line at 0.2 T in D.3(a).

Based on the good qualitative agreement between our data and the one electron and two electron Hamiltonian, respectively, we can clearly identify the even and odd charge parities.

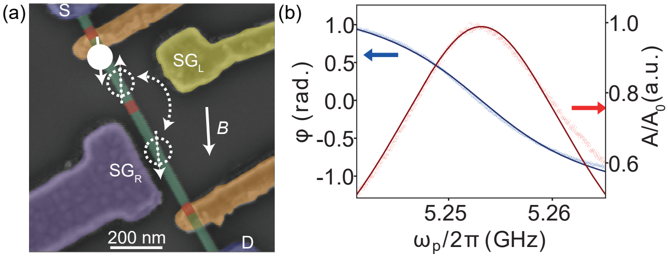

Figure D.4. Device B (a) False colored SEM-image of the device. The NW (green) is divided into two segments by an in-situ grown tunnel barrier (red), thus forming the DQD system. The NW ends are contacted by two Ti/Au contacts (S,D) and the NW segements can be electrically tuned by two Ti/Au sidegates SG$_R$ (purple) and SG$_L$ (yellow). A high-impedance, half-wave resonator is connected to SG$_R$. Top gates (orange) are kept at a constant voltage of -0.05 V. The magnetic field is applied in-plane at an angle of $\sim 60°$ to the NW. The arrows illustrate an even charge configuration with the two degenerate DQD states $T^+_{1,1}$ and $S_{2,0}$. (b) Resonance curve of the resonator in Coulomb blockade in amplitude A/A_0 (red) and phase φ (blue).

D.6. Analysis of device B

In this section we will discuss device B, which showed qualitatively similar behavior as device A which is discussed in the main text. Device B is shown in Fig. D.4(a), including a false-colored SEM-image of the crystal-phase defined NW DQD. The DQD is hosted in the 280 nm and 380 nm long zincblende segments (green), separated by 30 nm long wurtzite (red) tunnel barriers. A high-impedance, half-wave coplanar-waveguide resonator is capacitively coupled to the DQD at its voltage anti-node via sidegate SG_R. One more side gate SG_L (yellow) allows to tune the electrostatic potential and there are two top gates (orange) kept at constant voltage of -0.05. We show the bare resonance curve in Fig. D.4(b) and extract the bare resonance frequency $\omega_0/2\pi = 5.25308 \pm 0.00003$ GHz and the bare decay rate $\kappa/2\pi = 23.2 \pm 0.8$ MHz. The main difference to device A is the weaker coupling of the resonator gate SG_R to the DQD and the smaller voltages applied to the top gates, which resulted in a stronger coupling of the DQD to the leads. Consequently, we observe a weaker spin-photon coupling and a larger qubit linewidth compared to device A. However, the behaviour of the singlet-triplet qubit in magnetic field is qualitatively the same, demonstrating that this kind of singlet-triplet is reproducible.

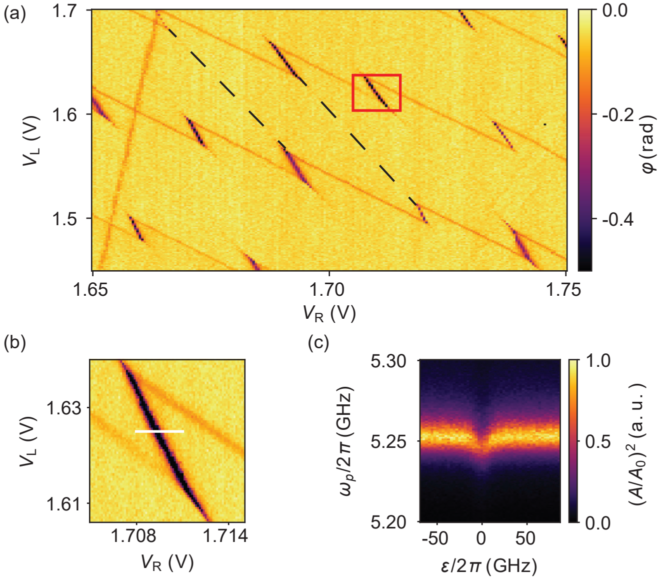

Figure D.5. Dispersive sensing of the DQD at B = 0. (a) Charge stability diagram of the device, in which the resonator phase φ is measured as a function of the SG voltages V_R and V_L. The negative slopes of the interdot transitions are due to the strong cross-capacitance of the larger gate SG_R. A zoom on the interdot transition pointed out by the red rectangle is shown in (b). (c) Resonator transmission $(A/A_0)^2$ versus probe frequency ω_p and detuning ϵ along the white line in (b). At the charge degeneracy point of the DQD, we observe a dispersive shift with respect to the bare resonance frequency.

D.6.1. Charge-stability diagram

Fig. D.5(a) shows the charge stability diagram of the DQD detected as a shift in the transmission phase φ of the resonator, plotted as a function of the two gate voltages V_L and V_R at a fixed probe frequency of 5.253 GHz, close to resonance. We observe a slanted honeycomb pattern, in which the inter-dot transition lines exhibit a negative slope due to the specific gate geometry (see Fig. D.4(a)), which results in the right gate (V_R) coupling stronger to both dots than the left (V_L). Using a capacitance model [81, 222], we extract the gate-to-dot capacitances $C_{R2} = 2.5 \pm 0.4\,\mathrm{aF}$, $C_{L2} = 1.65 \pm 0.08\,\mathrm{aF}$, $C_{R1} = 10.1 \pm 0.6\,\mathrm{aF}$ and $C_{L1} = 2.0 \pm 0.2\,\mathrm{aF}$.

In Fig. D.5(c) we show the resonator response while varying the probe frequency ω_p and changing the detuning ϵ along the white line in Fig. D.5(b). By fitting input-output theory to this particular IDT, we extract the inter-dot tunnel coupling $t = 4.40 \pm 0.06$ GHz, charge-photon coupling $g_0 = 150 \pm 3$ MHz, and charge qubit linewidth $\gamma = 1.5 \pm 0.5$ GHz.

D.6.2. Avoided crossing

As illustrated in Fig. D.6(c), the DQD can be operated as a singlet-triplet qubit when placed into a magnetic field. The qubit frequency $\omega_q = \Delta_{SO}/\hbar$ can be brought into resonance with the cavity frequency ω_0 at $B \approx 1.7$ T, as discussed in more detail below. At the resonance condition ($\omega_q \sim \omega_0$), an anti-symmetric (bonding) and a symmetric (anti-bonding) qubit-photon superposition are formed. Consistently, at a field of $B \approx 1.7\,\mathrm{T}$, we observe an anti-crossing between the resonator and the singlet-triplet qubit. Figure D.6(a) shows the anti-crossing as a function of the detuning voltage V_ϵ at constant magnetic field $B = 1.67\,\mathrm{T}$. By fitting a lorentzian to each trace of fixed detuning, we extract the resonance frequencies $\omega_{\Psi_\pm}$ and linewidths δ_ω (transmission and phase). Simultaneously, we fit the transition frequencies (dashed, white curves in Fig. D.6(a)) and linewidths (solid, black curve in Fig. D.6(b)) to the Jaynes-Cummings model. The transition frequencies are fitted as described in the methods section in the main text and linewidth of the transitions from the ground state to the predominantly photon-like dressed state $|\psi_-\rangle$ is given by

$$\begin{aligned}\delta_\omega &= \left|\langle\psi_-|g,1\rangle\right|^2 \kappa + \left|\langle\psi_-|e,0\rangle\right|^2 2\gamma \\ &= \cos^2(\theta)\,\kappa + \sin^2(\theta)\,2\gamma,\end{aligned} \tag{D.4}$$

where $\theta = \frac{1}{2}\tan^{-1}\left(\frac{2g}{\omega_q - \omega_0}\right)$ [64]. The fit parameters are given in the caption of Fig. D.6.

In Fig. D.6(c), we show the same anti-crossing as a function of B at a fixed detuning $\epsilon/2\pi \sim 1.65\,\mathrm{GHz}$. To extract the spin-photon coupling strength and qubit linewidth from this second measurement, we characterize the effective qubit transition frequency around the minimum $t_0 = t(B_0)$ by $\omega_q(B) = \sqrt{(2t_0)^2 + (\alpha_B(B - B_0))^2}$, where we introduce the heuristic scaling factor α_B . With this additional free parameter, we fit the Jaynes-Cummings model (dashed, white curves in Fig. D.6(c) and solid, black curve in Fig. D.6(d)) and extract the parameters described in the caption of Fig. D.6.

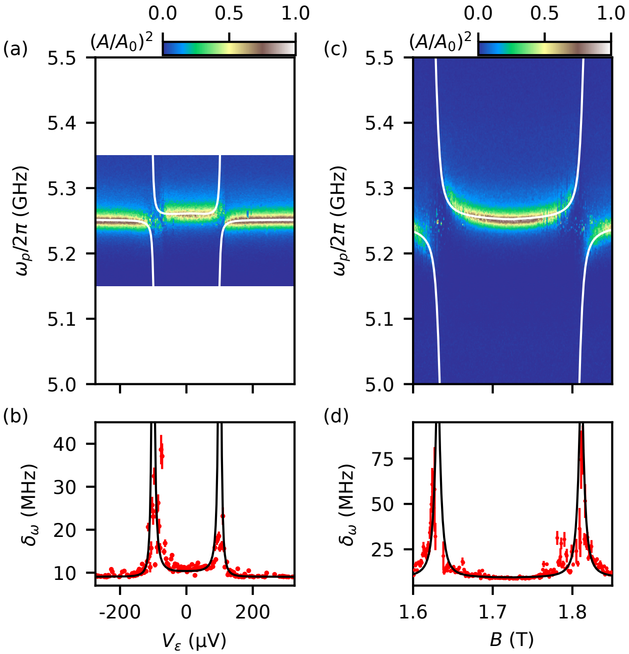

Figure D.6. Avoided crossing as function of gate voltage and field. (a) Resonator transmission at a fixed magnetic field $B = 1.67\,\mathrm{T}$ as function of detuning gate voltage V_ϵ. (b) Linewidths δ_ω extracted from (a). (c) Resonator transmission at a fixed detuning voltage corresponding to $\epsilon' = 1.65\,\mathrm{GHz}$ as function of magnetic field. (d) Linewidths δ_ω extracted from (c). Using a Jaynes-Cummings model fit, we extract the following parameters for (a) and (b): $g_0/2\pi = 164 \pm 6\,\mathrm{MHz}$, $t/2\pi = 1.34 \pm 0.05\,\mathrm{GHz}$, $\gamma = 317 \pm 28\,\mathrm{MHz}$, $\kappa = 18.2 \pm 0.2\,\mathrm{MHz}$. This results in a resonant coupling strength of $g(\omega_q = \omega_0) = 83 \pm 4\,\mathrm{MHz}$ when correcting for the mixing angle. From (c) and (d), we extract $g(\omega_q = \omega_0)/2\pi = 158 \pm 3\,\mathrm{MHz}$, $t(B = B_0)/2\pi \sim 0$, $\gamma/2\pi = 269 \pm 16\,\mathrm{MHz}$, $\kappa/2\pi = 18.6 \pm 0.2\,\mathrm{MHz}$. The larger value of the coupling strength in the magnetic-field (c,d) sweep compared to the detuning sweep (a,b) is attributed to the smaller mixing angle and reflected by the larger splitting at the anti-crossing in (c) compared to (a). Given the input power $P_{\mathrm{in}} = -133\,\mathrm{dBm}$, the average number of photons in these measurements is $n < 0.25$ (see methods of main part).

D.7. Magnetospectroscopy

In this section we analyse the magnetospectroscopy of device B analogously to device A. We measure the resonator phase φ as a function of the detuning ϵ and the magnetic field, as plotted in Fig. D.7(a). Resonator transmission and phase are simultaneously fitted to input-output theory and the qubit-photon coupling, qubit tunnel coupling and qubit linewidth are extracted. Descriptions to the method and formulas can be found in the main text and methods section.

We observe a qualitatively similar curve shape to device A in the main text. Again, we model the DQD by an effective two electron Hamiltonian which allows us to fit the gate voltage and field dependence of the IDT (white dashed line in Fig. D.7(a)). We find that the magneto-dispersion of the IDT is well fitted using the following fit parameters namely the spin-conserving singlet and triplet tunnel rates $t_c^S/2\pi \approx 29\,\mathrm{GHz}$, and $t_c^T/2\pi \approx 37\,\mathrm{GHz}$, the singlet-triplet coupling rate $t_{\mathrm{SO}}/2\pi \approx 5\,\mathrm{GHz}$, the electron g-factors of the right and left dots, $g_R \approx 1.8$ and $g_L \approx 2.8$, as well as the singlet-triplet energy splitting $\Delta_{\mathrm{ST}}/2\pi \approx 79\,\mathrm{GHz}$. As for device A, these fit parameters are consistent with parameters obtained previously in this material system [61, 76, 166, 249, 250].

As described in the main text, we extract the the qubit tunnel amplitude t, the qubit linewidth γ, and the qubit-photon coupling strength g as a function of B, which we plot in Figure D.7(b). A notable difference to device A, is the higher tunnel rate of device B. Unlike device A, device B has a qubit frequency predominantly above the resonator frequency and therefore anti-crosses only in small regions of the dispersion.

We will now shortly discuss the different regimes of the qubit, analogue to device A. Fig. D.7(c) shows the corresponding DQD level structure based on the fit parameters as a function of ϵ for different magnetic field.

At a low magnetic fields around $B = 0.1\,\mathrm{T}$, we observe again a singlet charge qubit with Zeeman-split triplets in the weak coupling limit. Again, we observe the characteristic double-dip structure between $B \sim 0.03\,\mathrm{T}$ and $B \sim 0.3\,\mathrm{T}$ of an even IDT.

As shown in the second panel of Fig. D.7(c) at high enough field $T^+_{1,1}$ becomes the ground state for $\epsilon < 0$. The spin-orbit interaction couples the singlet and triplet states, leading to an anti-crossing between $S_{2,0}$ and $T^+_{1,1}$.

Consistent with the interpretation of the formation of a singlet-triplet qubit, we measure an approximately constant tunneling rate t between $B \sim 0.5\,\mathrm{T}$ and $B \sim 1.1\,\mathrm{T}$. We extract the average spin-orbit tunneling to be $\bar{t}_{\mathrm{so}} = 4.0 \pm 0.3\,\mathrm{GHz}$. At $B \approx 1.3\,\mathrm{T}$, χ becomes positive. This is interpreted as a drop of the tunnel rate below the resonator frequency, $2t < \omega_0$. This decline in t is not captured by our simplified Hamiltonian model and we speculate that changes in the orbital structure of a many-electron DQD could be the reason.

At a magnetic field of $B \approx 1.7\,\mathrm{T}$, we observe a resonant interaction be-

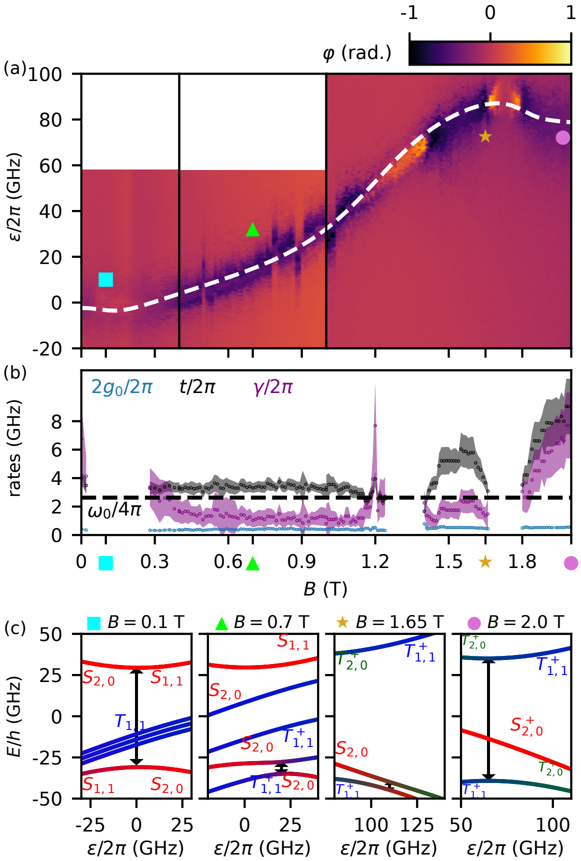

Figure D.7. Magnetospectroscopy of the singlet-triplet qubit. a) Resonator phase φ as a function of the magnetic field B and detuning ϵ. The white dashed line is a fit of the effective two-electron Hamiltonian to the data. b) Extracted tunnel rate $2t/2\pi$ (black), twice the qubit-photon coupling $2g_0/2\pi$ (cyan) and qubit linewidth $\gamma/2\pi$ (purple). Half the bare resonator frequency is indicated by the black dashed line. (c) Two-electron energy level diagrams at various magnetic fields with the corresponding field strength indicated in (a) and (b) by the given symbols. A constant offset of 20 GHz and 30 GHz was added to the energy levels at 1.65 T and 2.0 T, respectively.

tween the resonator and the singlet-triplet qubit leading to the anti-crossing as discussed in section D.6.2. As seen in the level structure in Fig. D.7(c) at $B = 1.65\,\mathrm{T}$, the triplet state $T^{+}_{2,0}$ becomes relevant. This results in a level repulsion between $T^{+}_{2,0}$ and $T^{+}_{1,1}$ and hence leads to a reduced splitting between the $S_{2,0}$ level and the $T^{+}_{1,1}$ states. In Fig. D.7(c), this is illustrated by the smaller level gap (black arrow) compared to the one at $B = 0.7\,\mathrm{T}$.

The level structure at very large magnetic fields is plotted at $B \approx 2\,\mathrm{T}$ in the right panel of Fig. D.7(c). Here, we observe the triplet charge qubit.

As discussed in the main text, the triplet charge qubit has a larger frequency detuning from the resonator frequency than the singlet-triplet qubit, leading to a smaller resonator shift.

Curriculum Vitae

Alessia Pally
Born on 3th Mai, 1994 in Uster (ZH), Switzerland

Education

11/2018–01/2023 **PhD in Experimental Physics at the University of Basel, Switzerland**

- Dissertation in the group of Prof. Dr. Christian Schönenberger
  "Crystal-phase defined nanowire quantum dots as a platform for qubits"

09/2016–10/2018 **Master of Science in Physics at ETH Zürich, Switzerland**

- Master thesis in the group of Prof. Klaus Ensslin
  "Electrostatically Defined Quantum Dots in Bilayer Graphene"
- Project work in the group of Prof. Christian Degen
  "Interferometric Study of Effects of Multireflection and Losses on Fringe Spectra"

09/2013–09/2016 **Bachelor of Science in Physics at ETH Zürich**

- Project work in the group of Prof. Klaus Ensslin
  "Edge Conduction in InAs"

2013 **Matura** Kantonsschule Uster, Zürich

Positions

11/2018-now Teaching assistant for physics at the University of Basel

Publications

- *"A singlet-triplet qubit sweet spot with enhanced dipolar coupling"*
  A. Pally*, J. H. Ungerer*, S, Bosco, A. Kononov , S. Lehmann, C. Thelander, K.A. Dick, C. Schönenberger
  in preparation

- *"Strong coupling between a microwave photon and a singlet-triplet qubit"*
  J. H. Ungerer*, **A. Pally***, A. Kononov , S. Lehmann, J. Ridderbos, P.P. Potts, C. Thelander, K.A. Dick, V.F. Maisi, P. Scarlino, A. Baumgartner, C. Schönenberger
  Nature Communications **15**, 1068 (2024)

- *"Charge Detection in Gate-Defined Bilayer Graphene Quantum Dots"*
  A. Kurzmann, H. Overweg, M. Eich, **A. Pally**, P. Rickhaus, R. Pisoni, Y. Lee, K. Watanabe, T. Taniguchi, T. Ihn, K. Ensslin
  Nano Letters **19**, 5216–5221 (2019)

- *"Coupled Quantum Dots in Bilayer Graphene"*
  M. Eich, R. Pisoni, **A. Pally**, H. Overweg, A. Kurzmann, Y. Lee, P. Rickhaus, K. Watanabe, T. Taniguchi, K. Ensslin, and T. Ihn.
  Nano Letters **18**, 5042–5048 (2018)

* Equal contribution

Talks

- *RF coupling of a crystal-phase defined nanowire quantum dot*
  QCQT Research Seminar, University of Basel, Basel (Switzerland), May 2022

- *Coupling of a crystal-phase defined InAs nanowire double quantum dot to a high-impedance resonator*
  QSIT General Meeting, Arosa (Switzerland), February 2022

- *Electrostatically Defined Quantum Dots in Bilayer Graphene*
  QSIT junior Meeting, Passugg (Switzerland), June 2018

Poster Contributions

- *“Coherent coupling between a microwave photon and spinful states of a crystal-phase defined double-quantum dot in a spin-orbit nanowire”*
  5th International Conference on Spin-Based Quantum Information Processing, Pontresina (Switzerland), September 2022
- *“Optimising the dielectrics for nanowire integration in circuit QED system”*
  Annual meeting of the NNCR spin, Pontresina (Switzerland), November 2022
- *“Transport Spectroscopy in Semiconducting Nanowire Electronic Devices”*
  QSIT General Meeting, Arosa (Switzerland), February 2020
- *“Tunnel spectroscopy of superconducting proximity effect in InAs nanowires using aligned crystal-phase quantum dots”*
  One-Dimensional Systems for Quantum Technology, Bad Honnef (Germany), June 2019

Acknowledgments

This thesis and the past four years I spent in Basel would not have been possible without the support of many amazing people. Friends, family, colleagues, and collaborators all had a great influence on me in these years and I would not be where I am now without them. Therefore, I would like to thank everyone for their continuous support in the following paragraphs.

First, I would like to thank my PhD supervisor Prof. Dr. Christian Schönenberger for giving me this chance to study and perform this research. He encouraged me and helped me throughout this four years. His never-ending passion for science and attention to even tiny details in measurements inspired me. He was always helpful and supportive even when the project seemed stuck. I am especially thankful that he helped me find new topics to work on when it became clear that our original project was not going to work as intended. The atmosphere in the group was always warm, welcoming, and very social, which Christian always fostered and supported. Thank you very much for these four years!

Secondly, I would like to thank Prof. Dr. Georgios Katsaros and Dr. Heike Riel for taking the time to read my thesis and attending my defense. I am honored to have two such distinguished scientists in my PhD committee.

I would like to thank the people that supervised my work over the years. Especially, Dr. Malin Nilsson who supervised me during the first two years of my PhD. She taught me a lot about fabrication, measurements, and especially the great nanowires and quantum dots I got to work with. I had a great start into my PhD with you!

Further, I would like to thank Dr. Artem Kononov who supervised me during my last year and the writing of this thesis. You were always a great support to me. You helped my a lot in the lab with your great understanding of physics and in handling and fixing the Triton. I hope it eventually goes to 20 mK again! Your support has been invaluable to me, especially when I was struggling with my thesis.

Then, I would like to thank Dr. Andreas Baumgartner for his support over this four years. Especially, for helping me write my chapter about superconducting contacts and reading my thesis. I am still not sure what I would have written in that chapter without you!

During my time here I had the joy to work with several other former PhD

students. I want to especially thank Dr. Jann Ungerer with whom I did the main work written in my thesis. This combination of cQED and quantum dots would not have been possible without his expertise. Thank you for always pushing for more and better results, without you this would not have been possible!

On this note I would like to thank Dr. Luk Yi Cheung for working with me on making Pb contacts during the pandemic. Unfortunately, the physics did not work out in our favor, but I am still proud of what we achieved. And even after this, your wisdom and knowledge of RF and qubits have been invaluable to me!

I am also very thankful to our collaborators at Lund University who are growing these wonderful nanowires and exchanging their knowledge with us. Thank you very much, Dr. Sebastian Lehmann, Prof. Dr. Claes Thelander, and Prof. Dr. Kimberly Dick for always growing the nanowires tailored to our specific needs. I would also like to thank our other collaborators form Lund, Prof. Dr. Ville Maisi and Dr. Antti Ranni, who helped us with their knowledge of these nanowires in many interesting discussions.

On this note, I would also like to thank our collaborators in EPFL in the group of Prof. Dr. Pasquale Scarlino. I had a lot of interesting discussions with them and I am glad that they will continue some of our work in EPFL. Thank you Fabian Oppliger, Franco de Palma, Dr. Won Jin Jang, and Dr. Radha Krishnan. I am looking forward to seeing your results!

I also want to express my thanks to my team nanowire and office buddies Dr. Arunav Bordoloi and Dr. Frederick Thomas. I learned a lot from you about fabrication and how to handle a PhD. I also had a lot of fun in the office. It is never boring with such a dynamic duo!

Further, I would like to thank all the great people I got to work with in the Nanoelectronics group. From the beginning the group atmosphere was very warm and social. We did lots of barbecues, group trips, and events together. I enjoyed our time a lot! I want to especially thank my office mates over the years, Dr. David Indolese, Dr. Mehdi Ramezani, Dr. Lukas Gubser, Dr. Blesson Varghese, Rounak Jha, Dr. Ian Correa Sampaio, Carlo Ciaccia, Dr. Christian Jünger, Dr. Olivier Faist, Jibin Sunil, Dr. Lujun Wang, Dr. Arunav Bordoloi, Dr. Frederick Thomas, and Deepankar Sarmah. It was never boring in the office with you! And sometimes we even managed to work a bit.

I would also like to thank the people with whom I did not have the pleasure to share an office with, Dr. Jann Ungerer, Dr. Paritosh Karnatak, Dr. Martin Endres, Dr. Zarina Mingazheva, Matthijs Hermans, Dr. Malin Nilsson, Dr. Joost Ridderbos, Dr. Prasanta Kumbhakar, Dr. Libin Wang, Dr. Simon Zhilmann, Han Zheng, Dr. Gulibusitan Abuliz, Dr. Gergö Fülöp, and Dr. Roy Haller.

During my time here, I also got the chance to supervise two great students, Adilia Iafarova and Ivan Krastilevskiy. Thank you for your help and interest, it was a joy to work with the two of you!

Besides the people working in research there are also invaluable work done behind the scene. A big thanks goes to Barbara Kammermann and Astrid Kalt, who kept the departement running and were always there if I had an administrative problem. I would also like to thank Dominik Sifrig and Patrick Stöckli for always supplying us with helium and helping with technical problems. On that note, I would also like to thank Sascha Martin and the mechanical workshop for their continuous support. I would also like to thank Michael Steinacher, Sascha Linder and the electronic workshop for their help with electronics and soldering.

Last, but not least, I want to thank my friends and family for accompanying me on this journey for four years. Especially, my parents Roland and Beatrice and my sister Andrea, as well as my friends form my studies Pascale and Alex. Thank you for always being there for me!

Thank you all so much!